



저작자표시-비영리-변경금지 2.0 대한민국

이용자는 아래의 조건을 따르는 경우에 한하여 자유롭게

- 이 저작물을 복제, 배포, 전송, 전시, 공연 및 방송할 수 있습니다.

다음과 같은 조건을 따라야 합니다:



저작자표시. 귀하는 원저작자를 표시하여야 합니다.



비영리. 귀하는 이 저작물을 영리 목적으로 이용할 수 없습니다.



변경금지. 귀하는 이 저작물을 개작, 변형 또는 가공할 수 없습니다.

- 귀하는, 이 저작물의 재이용이나 배포의 경우, 이 저작물에 적용된 이용허락조건을 명확하게 나타내어야 합니다.
- 저작권자로부터 별도의 허가를 받으면 이러한 조건들은 적용되지 않습니다.

저작권법에 따른 이용자의 권리는 위의 내용에 의하여 영향을 받지 않습니다.

이것은 [이용허락규약\(Legal Code\)](#)을 이해하기 쉽게 요약한 것입니다.

[Disclaimer](#)

Doctoral Thesis

High Temperature VO₂ based Microbolometer
with Enhanced Light Absorption

Hye Jin Lee

Department of Materials Science and Engineering

Graduate School of UNIST

2019

High Temperature VO₂ based Microbolometer with Enhanced Light Absorption

Hye Jin Lee

Department of Materials Science and Engineering

Graduate School of UNIST

High Temperature VO₂ based Microbolometer with Enhanced Light Absorption

A thesis/dissertation
submitted to the Graduate School of UNIST
in partial fulfillment of the
requirements for the degree of
Doctor of Philosophy

Hye Jin Lee

06. 04. 2019

Approved by

Advisor

Jeong Min Baik

High Temperature VO₂ based Microbolometer with Enhanced Light Absorption

Hye Jin Lee

This certifies that the thesis/dissertation of Hye Jin Lee is approved.

06. 04. 2019

signature

Advisor: Jeong Min Baik

signature

Ju-Young Kim: Thesis Committee Member #1

signature

Suk Bin Lee: Thesis Committee Member #2

signature

Won Jun Choi: Thesis Committee Member #3

signature

Seung-Hyub Baek: Thesis Committee Member #4;

Abstract

Microbolometer depends on the change in electrical resistance of material as the temperature of the material changes. As element technology of microbolometer, VO_x thin films are widely used due to high temperature resistance coefficients (TCR) and low noise. However, due to the metal-insulator-transition (MIT) property of the VO₂ thin film, it is difficult to fabricate a microbolometer at 68°C which can operate at high temperatures. Also, high light absorption is required. Here, we developed VO₂ thin films and nanowires. And we developed a light absorber to increase the responsivity of microbolometer through high light absorption and applied it to various application. In order to obtain high quality of thermal sensitive material, we fabricated the resistor included in micro-bolometer which has a low resistance and a high temperature resistance coefficient (TCR) by growing the tetragonal VO₂ crystal phase on the oxide thin film of the perovskite structure. In addition, infrared absorber has multilayer structure in which Ti metal layer and an MgF₂ dielectric layer are alternately deposited with a several repetition cycle. The absorber layer shows about 70 % infrared absorption in the range of 8–14 μm. In this paper, we used VO₂ for the TCR material and the infrared absorber, showing the enhanced performance compared to that of the conventional micro-bolometer. The micro bolometer operates even at high temperature of 100°C. The micro-bolometer has a responsivity and detectivity of 4.90×10^3 V/W and 1.45×10^8 cmHz^{1/2}/W at 100°C.

In VO₂ materials study, we demonstrated the mechanism of VO₂ nanowires growth and MIT based strain sensor. The remarkable electronic and mechanical properties of nanowires promise fascinating applications; however, the difficulties of assembling ordered arrays of aligned nanowires over large areas prevent their integration into many practical devices. In this paper, we show that aligned VO₂ nanowires form spontaneously after heating a thin V₂O₅ film on a grooved SiO₂ surface. Nanowires grow after complete de-wetting of the film, formation of super-cooled nanodroplets and subsequent Ostwald ripening and coalescence. We investigate the growth mechanism with molecular dynamics simulations of spherical Lennard-Jones particles – the simulations help explain how the grooved surface produces aligned nanowires. With this simple approach, we produce self-aligned, millimeter long nanowire arrays with uniform metal-insulator transition properties which, after transfer to a polymer substrate, act as a highly sensitive array of strain sensors with very fast response time of several tens of milliseconds.

As photo-thermal conversion study, we developed light absorber in broad wavelength. A facile method to fabricate mechanically robust stretchable solar absorber for stretchable heat generation and enhanced thermoelectric generator is demonstrated. This strategy is very simple, it is a multilayer film made of titanium and magnesium fluoride optimized by two-dimensional finite element frequency domain simulation, followed by the application of mechanical stress such as bending and stretching to the film. This process produces many microsized sheets with submicron thickness (~ 500 nm), showing great

adhesion to any substrates such as fabrics and PDMS. It shows quite high light absorption of approximately 85 % over a wavelength range from 0.2 to 4.0 μm . Under 1-sun illumination, the solar absorber on various stretchable substrates increased the substrate temperature to approximately 60°C, irrespective of various mechanical stresses such as bending, stretching, rubbing, and even washing. The thermoelectric generator with the absorber on the top surface also showed an enhanced output power of 60 %, compared to that without the absorber. With incident solar radiation flux of 38.3 kW/m^2 , the output power significantly increased to 24 mW/cm^2 due to the increase of the surface temperature to 141°C.

Reflectivity is an important part of photo-thermal conversion. We have studied research on antireflective films applicable to solar cells. A series of hierarchical ZnO-based antireflection coatings with different nanostructures (nanowires and nanosheets) is prepared hydrothermally, followed by means of RF sputtering of MgF_2 layers for coaxial nanostructures. Structural analysis showed that both ZnO had a highly preferred orientation along the $\langle 0001 \rangle$ direction with a highly crystalline MgF_2 shell coated uniformly. However, a small amount of Al was present in nanosheets, originating from Al diffusion from the Al seed layer, resulting in an increase of the optical bandgap. Compared with the nanosheet-based antireflection coatings, the nanowire based ones exhibited a significantly lower reflectance ($\sim 2\%$) in ultraviolet and visible light wavelength regions. In particular, they showed perfect light absorption at wavelength less than approximately 400 nm. However, a GaAs single junction solar cell with nanosheet-based antireflection coatings showed the largest enhancement (43.9%) in power conversion efficiency. These results show that the increase of the optical bandgap of the nanosheets by the incorporation of Al atoms allows more photons enter the active region of the solar cell, improving the performance.

Contents

CHAPTER 1. Introduction	1
CHAPTER 2. Theoretical Background	3
2.1 Uncooled bolometers for thermal imaging	3
2.1.1 Thermal detectors.....	3
2.1.2 Bolometer theory.....	3
2.2 Characteristic of vanadium oxide	4
2.2.1 Metal insulation transition (MIT) of vanadium oxide nanowire.....	4
2.2.2 Metal insulation transition (MIT) based strain sensor.....	6
2.3 Application for enhancing light absorption.....	6
2.3.1 Solar thermal absorber for enhancing thermoelectric generator (TEG) efficiency.....	6
2.3.2 Antireflective layer for enhancing performance of solar cell.....	7
2.4 Reference.....	8
CHAPTER 3. Experimental Procedure	10
3.1 VO ₂ based Micro-bolometer with infrared absorbing layer.....	10
3.2 Directional Ostwald ripening for producing aligned arrays of nanowires.....	10
3.3 Solar absorbers with submicron-thick multilayer sheets.....	11
3.4 Optical design of ZnO-based antireflective layers for enhanced GaAs solar cell performance...	11
CHAPTER 4. High Temperature VO₂ based Microbolometer with Enhanced Light Absorption .13	
4.1 High temperature operation of VO ₂ based micro-bolometer with infrared absorbing layer.....	13
4.1.1 Introduction.....	13
4.1.2 Experimental detail.....	14
4.1.3 Result and discussion.....	15
4.1.4 Conclusion.....	21
4.1.5 Reference.....	23
4.2 Directional Ostwald ripening for producing aligned arrays of nanowires.....	24
4.2.1 Introduction.....	24
4.2.2 Experimental detail.....	25
4.2.3 Result and discussion.....	26
4.2.4 Conclusion.....	39
4.2.5 Reference.....	41
4.3 Mechanically robust, stretchable solar absorbers with submicron-thick multilayer sheets for wearable and energy applications.....	45
4.3.1 Introduction.....	45
4.3.2 Experimental detail.....	46

4.3.3 Result and discussion.....	47
4.3.4 Conclusion.....	60
4.3.5 Reference.....	61
4.4 Optical design of ZnO-based antireflective layers for enhanced GaAs solar cell Performance...64	
4.4.1 Introduction.....	64
4.4.2 Experimental detail.....	64
4.4.3 Result and discussion.....	66
4.4.4 Conclusion.....	75
4.4.5 Reference.....	77
Curriculum Vitae.....	80

LIST OF FIGURES

Figure 1. Schematic of microbolometer structure

Figure 2. (a) Schematic diagram of nanowire growth reactor. (b) SEM image of VO₂ nanowires grown at 900°C on Si₃N₄/Si substrate

Figure 3. Fabrication process of micro-bolometer.

Figure 4. TCR value of VO₂(B) as a functional of temperature.

Figure 5. (a) SEM image of multi-layers infrared absorber and (b) Fourier transformed infrared spectroscopy (FT-IR) over a wavelength range from 8 to 14 μm.

Figure 6. SEM image of micro-bolometer with VO₂(B) thin film and multi-layer infrared absorber.

Figure 7. Schematic of micro-bolometer measurement system.

Figure 8. Inverse of resistance of micro-bolometer (a) without absorber and (b) with absorber as a functional of the square of bias current under various temperature.

Figure 9. Responsivity of micro-bolometer (a) without absorber and (b) with absorber as a functional of frequency under various temperature.

Figure 10. Responsivity and noise voltage of micro-bolometer (a) without absorber (b) with absorber as a functional of bias current under various temperature.

Figure 11. Detectivity of micro-bolometer (a) without absorber (b) with absorber as a functional of bias current under various temperature.

Figure 12. SEM image of VO₂ nanowires. (a, b) SEM images of randomly oriented VO₂ nanowires on a flat SiO₂/Si substrate and aligned along the direction of the V-groove, respectively. Scale bars in a are 20 μm (top) and 5 μm (bottom). Scale bar in b, 5 μm. (c) Millimeter-long horizontally aligned nanowire. (d) Schematic diagram of the VO₂ nanowire growth with the angle of V-groove. (e) SEM images with the angle of V-groove (70°, 100°, and 120°). Scale bars, 5 μm (left) and 1 μm (right).

Figure 13. The histogram of length and width of randomly oriented VO₂ nanowires on a SiO₂/Si substrate.

Figure 14. The VO₂ nanowire growth as a function of the V₂O₅ thin film thickness. Scale bars, 500 nm.

Figure 15. The cross-sectional images of the grown VO₂ with the shape of the V-grooved surface.

Figure 16. The millimeter-long VO₂ nanowires SEM image and I-V measurement graph.

Figure 17. (a) Schematic fabrication process of V-groove templates and schematic diagrams of the V-groove templates with different pitch size (b) and KOH etching time (c).

Figure 18. Morphological and structural evolution. (a) Ex-situ SEM images of morphological evolution of the vanadium oxide as a function of temperature and growth time. Scale bar: 1 μm. (b, c) Raman spectra obtained with the laser incident on the V-grooved surface and the flat surface between the V-grooves, respectively.

Figure 19. MD simulation results for directional Ostwald ripening. (a) MD simulation of a simple spherical particles interacting with Lennard-Jones (LJ) potential on a surface with a half flat and the other half V-shaped. (b) time-evolution of droplets size.

Figure 20. (a) The SEM image of VO₂ nanowire tail located on V groove substrate and (b) the schematic image of Ostwald ripening process on flat substrate and V groove substrate.

Figure 21. Cross-sectional TEM images of VO₂ nanowire grown in V-grooved surface. (a) Cross-sectional low-resolution transmission electron microscope (TEM) image of single VO₂ nanowire grown in V-grooved surface. Scale bar, 0.2 μm. (b) high-resolution TEM image of the VO₂ nanowire. Scale bar, 5 nm. (c, d) high-resolution TEM images of the VO₂ nanowire at the interface region near the SiO₂/Si substrate. Scale bar, 5 nm. The corresponding fast Fourier transform (FFT) in b and d are shown.

Figure 22. Electron energy loss spectroscopy (EELS) in V₂O₅ and VO₂ regions.

Figure 23. (a) SEM image and (b) EDXS result of the transferred VO₂ nanowire onto PDMS substrate.

Figure 24. Highly sensitive strain sensor made with VO₂ nanowire arrays. (a) Schematic diagrams of the fabrication process for the strain sensor array with VO₂ nanowire transferred onto the PDMS substrate. (b) Photos of the strain sensor and the SEM images of the VO₂ nanowires transferred onto PDMS substrate. To measure the resistance of the device, Cr/Au electrode was deposited onto the nanowires. (c) Change in resistance ($\Delta R/R_0 = (R - R_0)/R_0$) with the bending motion and the magnitude of the strain. The inset shows the expanded view of the change in resistance at the strain of 0.3 %. (d) Change in the resistance of VO₂ nanowire array with the strain of 0.3 % during 1 hour as bending and release cycles.

Figure 25. (a) (left) Cross-sectional SEM image and (right) photo of the multilayer film deposited on glass substrate. The scale bar is 0.2 μm and 1 cm, respectively. (b) Photo showing bending of the multilayer deposited on polyurethane and SEM image after the bending (scale bar 50 μm). (c) Schematic illustration showing that the micro-sized sheets are produced after simple mechanical stresses such as bending and stretching. (d) Photos of fabric with the absorber before and after the rubbing (e) SEM image of each fabric (The scale bar 10 μm , respectively).

Figure 26. 2D and 3D AFM images of the absorber deposited on glass.

Figure 27. Refractive indices of each materials (Al, Pt, Ti) with wavelength.

Figure 28. (a) Calculated absorptance and solar irradiance as a function of wavelength for given multilayer films. (b) The solar absorption spectrum with different thickness of multilayers. (c) Total solar absorption versus thickness of each layer, Ti and MgF₂. (d) Absorption measured by UV-Vis-NIR spectroscopy and Fourier transformed infrared spectroscopy over a wavelength range from 0.2 to 4 μm .

Figure 29. (a) Schematic of the case of a normal incident light for multilayers. (b) An example of absorption-spectrum calculation for Ti (27.3 nm)/MgF₂ (300 nm) multilayer structure. (c) The electric field profile through the thickness from the propagation matrix.

Figure 30. The total solar absorption of the optimum metal thickness for Al, Pt and Ti.

Figure 31. The simulated solar absorption of the multilayer as a function of the number of the layer.

Figure 32. The optical absorption of the multilayered films with the incident angle.

Figure 33. The optical absorption of the multilayered films as a function of annealing temperature.

Figure 34. (a) Surface temperature (b) Top view thermal image of the multilayer ($\text{Ti/MgF}_2 = 7.3 \text{ nm}/96.5 \text{ nm}$) deposited on polyurethane as a function of the number of layers under 1-sun illumination. (c) Surface temperature measured under illumination of 680 nm-filtered light ($> 680 \text{ nm}$). (d) Surface temperature obtained by turning on and off repeatedly every 10 mins.

Figure 35. The photograph and thermal image comparison of absorber deposited on fabrics such as linen, spandex, cotton napping and cotton under AM 1.5G illumination.

Figure 36. Real photos of cottons with and without absorber. The surface temperatures of the substrates were measured as a function of measuring time outside.

Figure 37. (a) Photos and thermal images of the fabrics with the absorber attached on the surface of a wrist under concave bending (top), neutral (center) and convex bending (bottom) condition. (b) Photos and thermal images of PDMS with the absorber under highly stretched condition. (c) Surface temperature measured under 1-sun illumination after rubbing and washing several times the fabrics. The inset shows the photos and thermal images.

Figure 38. SEM images of the absorber on cotton fabrics after rubbing and washing several times and thermal images of the samples measured under AM 1.5G illumination.

Figure 39. The optical absorption of the cotton fabrics with the absorber before and after rubbing.

Figure 40. The temperature of the absorber as a function of bending times.

Figure 41. (a) (left) Schematic images of the solar absorber formed on the top surface of the thermoelectric generator and (right) the measurement tools. (b) Temperature difference of the thermoelectric generator as a function of cooling temperature. The open and closed diamonds are the output powers of thermoelectric generators with and without the solar absorber, respectively. (c) Output power of the thermoelectric generator as a function of load resistance. (d) Output power and surface temperature of the thermoelectric generator as incident solar radiation flux.

Figure 42. (a) Schematic images of a GaAs based solar cell with MgF_2/ZnO nanosheet/ Al/ZnS as the AR coatings. Schematic and SEM images of (b) MgF_2/ZnO nanowires/ ZnO/TiO_2 , (c) MgF_2/ZnO

nanowires/ZnO/ZnS, and (d) MgF₂/ZnO nanosheet/Al/ZnS. The scale bars in the SEM images are 1 μm except of the right image of (d), which is 250 nm. The insets also show the enlarged images (scale bar 50 nm).

Figure 43. Top view of SEM image for ZnO nanosheet/Al/ZnS with thickness of Al (a) 0.5 nm, (b) 1 nm, (c) 3 nm and (d-f) histogram of the ZnO nanosheets thickness distributions along Al thickness, respectively.

Figure 44. Scanning electron micrographs of ZnO nanosheet grown on Si substrates; (a) Top view and (b) cross-sectional SEM image, Energy-dispersive X-ray spectroscopy (EDXS) of (c) ZnO nanosheet/Al/ZnS, (d) ZnO nanowires/ZnO/ZnS.

Figure 45. The peak in the Al 2p spectra corresponds to Al-O and Al-Zn-O bonds. The Al-O binding energy was observed at 73.48 eV, lower than that (~ 75.6 eV) of the pure Al₂O₃.

Figure 46. Transmission electron microscopy (TEM) images of MgF₂ thickness on MgF₂/ZnO nanowires (scale bar is 5 nm).

Figure 47. Transmission electron microscopy (TEM) images of MgF₂/ZnO nanowires and MgF₂/ZnO nanosheet. (a) Low-magnification MgF₂/ZnO nanowires (scale bar is 50 nm) and (b) High-resolution TEM (HR-TEM) image of MgF₂/ZnO nanowires (scale bar is 5 nm). (c) Low-magnification MgF₂/ZnO nanosheet (scale bar is 0.2 μm) and (d) HR-TEM image of MgF₂/ZnO nanosheet (scale bar is 5 nm). The inset shows a Fast Fourier Transform (FFT) of the image.

Figure 48. (a) UV-Vis-NIR reflectance spectra over a wavelength range from 300 to 800 nm: MgF₂/ZnO nanowires/ZnO/TiO₂, MgF₂/ZnO nanowires/ZnO/ZnS and MgF₂/ZnO nanosheet/Al/ZnS. (b) UV-Vis-NIR absorption spectra in the range from 300 to 800 nm. The absorption calculated by measuring the reflection (at a 7 ° angle of incidence) using $A \% = 100 \% - R \% - T \%$ while it is assumed that the scattering effect is negligible. (c) Corresponding plot of transformed Kubelka-Munk function versus the energy of the light. (d) Simulated spectra of the effect of the straight MgF₂ shell on the reflectance. Wavelength-dependent simulated reflectance distribution at 90 °.

Figure 49. Simulated reflectance spectra for the ZnO/TiO₂ and ZnO/ZnS double layered films with different thickness. The thickness is ZnO 100nm, TiO₂ (or ZnS) (a) 50 nm, (b) 60 nm, (c) 70 nm and (d) 100 nm.

Figure 50. (a) The current density-voltage (J-V) curves of GaAs based solar cells with MgF₂/ZnO nanowires/ZnO/TiO₂, MgF₂/ZnO nanowires/ZnO/ ZnS, MgF₂/ZnO nanosheet/Al/ZnS and without ARC layer under AM 1.5 G illumination (100 mW/cm²). (b) The external quantum efficiency (EQE) spectra of GaAs based solar cells with none, the MgF₂/ZnO nanowires/ZnO/TiO₂, MgF₂ /ZnO nanowires/ZnO/ZnS, MgF₂/ZnO nanosheet/Al/ZnS ARC layers.

Table 1. Micro-bolometer parameters at room temperature.

Table 2. Micro-bolometer parameters at 100°C.

Table 3. Short-circuit current density (J_{SC}), open-circuit voltage (V_{OC}), fill factor (FF) and power conversion efficiency of solar cells before and after integrated with the MgF₂/ZnO nanowires/ZnO/TiO₂, MgF₂/ZnO nanowires/ZnO/ZnS and MgF₂/ZnO nanosheet/Al/ZnS layer under AM1.5G normal illumination at room temperature

CHAPTER 1. Introduction

Many uncooled infrared (IR) detectors have been developed for many military and commercial applications, such as thermal sensors, night vision cameras, infrared cameras and surveillance devices. In particular, vanadium oxide-based microbolometer are the most widely used. Thermal sensor elements commonly used in commercial, uncooled thermal cameras. The merits of vanadium oxide (VO_x) uncooled microbolometer are suitable for low power consumption, room temperature operation, light weight and portable applications. Also, VO_x thin films are widely used due to high temperature resistance coefficients (TCR) and low noise. However, due to the metal-insulator-transition (MIT) property of the VO₂ thin film, it is difficult to fabricate a microbolometer at 68°C which can operate at high temperatures. Therefore, the commercial VO_x microbolometer operates mainly at room temperature and the TCR value of VO_x is 2 ~ 3%/K. Recently, TCR materials have been developed for obtain large TCR values such as VO_x/ZnO/VO_x multilayer, VWO layer, and V₂O₅/V/V₂O₅ multilayer sandwich structure. In the case of infrared sensors, infrared absorber material is required inside the detector stack to perform absorption and then transfer heat to micro-bolometer because of thermal conduction. Infrared absorber materials have been used in the VO_x based microbolometer such as Titanium (Ti), silicon nitride (Si₃N₄), Titanium Nitride (TiN), Nichrome (NiCr) and gold black. Most widely used gold black has very high absorption over a broad wavelength range. On the other hand, this low-density material is extremely fragile, which makes it difficult to integrate onto a micro-bolometer array, since usual fabrication processes destroy the film.

Today's engineers envision miniaturized circuits interconnected by nanowires with specialized electronic, photonic, energy conversion, gas sensing, and bio-sensing properties. Unlike conventional wires, nanowires must be grown from physical and chemical processes like liquid-phase self-assembly, templated growth in nanometer sized pores, or chemical vapor depositions. To create circuits with nanometer scale control requires growth processes that can precisely position and align nanowires and produce them with highly uniform dimensions. This remains a largely unsolved problem. A clue to a solution comes from studies of vanadium dioxide (VO₂) nanowire growth. In the paper, a film of V₂O₅ was heated on a SiO₂ substrate and substantially below the melting point of V₂O₅, where the film dewets and forms super-cooled liquid nano-droplets that spontaneously form randomly distributed single crystal VO₂ nanowires with uniform dimensions. Nanowires composed of oxides of molybdenum, ruthenium, and iron could also be produced by a mechanism that involves super-cooled nano-droplet mobility, coalescence and Ostwald ripening.

Solar thermal technologies, which convert solar energy into heat, have received increasing interest during the past few decades and are considered a promising candidate due to high energy storage density and high energy conversion efficiency in many emerging applications such as solar collectors for heating and cooling systems, solar cookers, solar heated clothes, and steam generators. The solar

thermal efficiency is strongly dependent on the optical properties of the solar absorber. In general, for high-temperature applications, optimal solar-thermal energy conversion can be achieved by selectively absorbing solar energy with high infrared (IR) transmittance. With the high efficiency, it should be easy to manufacture and cost-effective, chemically and thermally stable at elevated temperatures. Recently, metamaterial absorbers, typically made of metals (e.g., Au, Ag, Ni) and dielectrics (e.g., HfO₂, SiO₂, Al₂O₃) are able to significantly increase the optical cross section of the structure, leading to greatly enhanced absorption in certain wavelength ranges caused by surface plasmon excitations. A plasmonic resonant visible light absorber, composed of a square array of vertically coupled nanowires coated with metal film, was developed, achieving ca. 75 % average absorption over a wavelength range from 0.4 to 0.8 μm. Hedayati and coworkers proposed perfect plasmonic metamaterial absorbers with an absorption of around 100 % over the entire visible region. However, the metamaterials require accurate lithography techniques for sub-wavelength feature sizes such as metallic concentric ring patterns and the absorption is critically dependent on the absorption angle. Flexible and stretchable substrates, such as polymer and fabrics, also limit the size of metadata that can be achieved with mechanical deformations that are not available in flexible applications.

Antireflective (AR) coatings based the ZnO nanostructures have received increasing interest during the past few decades and may be considered as one of the promising candidates due to the excellent optical properties and the controllable anisotropic growth of ZnO. In particular, the ZnO can easily be synthesized as a various form of nanostructures such as nanowires, nanobelts, nanoplatelets, and nanorods by well-developed methods, demonstrated by many research groups. However, as a promising candidate, most work has focused on the nanowires-based AR coatings. The graded refractive index to the active region of the solar cell, which is essential in obtaining low reflectance, can be achieved by the gradual decrease in the diameter of the nanowires to the bottom from the top. Various experimental parameters such as substrate, growth time, temperature, amount of precursor and additives should be considered for the fine control of the nanowires diameter. However, the morphology was found to be quite sensitivity to these parameters. Recently, it was reported that the coaxial-type surface by coating low refractive index materials on the nanowires could decrease the reflectance, significantly at low angle of incident light, thereby, enhancing the solar cell performance over broadband and wide angle ranges. However, the enhancement of the performance of solar cell with the ZnO nanowires-based AR coatings may not be huge, although the AR coatings show quite low reflectance comparable to those of conventional multi-layered antireflective films.

CHAPTER 2. Theoretical Background

2.1 Uncooled bolometers for thermal imaging

2.1.1 Thermal detectors

Infrared detectors are classified as thermal detectors and photon detectors. These two things work in a very different way. Thermal detectors have an absorber with an absorber, which converts the light into heat and provides an electrical signal output that indicates the change in the absorber temperature. Since the heat detector is not wavelength dependent, it can be used as an infrared detector when used with window materials such as Si that transmit infrared light. Thermal sensors are mainly classified into a thermopile detector whose electromotive force changes, bolometer whose resistance changes, pyroelectric sensors whose dielectric surface charge changes, and diodes whose voltage-current characteristics change. Because photosensitive material of bolometer is composed of thermoelectric conversion materials and uses bolometer resistance, the temperature coefficient of resistance is the main cause of determining bolometer sensitivity. Since bolometer sensitivity does not depend on the size of the photosensitive area, it is possible to make a detector with no sensitivity reduction even if the photosensitive area is small.

2.1.2 Bolometer theory

IR detection by microbolometer depends on the change in electrical resistance of material as the temperature of the material changes. The blackbody is a Lambert source with the spectral emission given by Planck's blackbody radiation equation.

$$M_{\lambda}(T, \lambda) = \frac{2\pi hc^2}{\lambda^5 \left(e^{\left(\frac{hc}{\lambda kT} \right)} - 1 \right)} \text{ (W. m}^{-3}\text{)}$$

Vanadium oxide was applied as thermal sensitive material. The suspended $\lambda/4$ cavity structure was designed to enhance the infrared light coupling. The gap of sacrificial layer between silicon nitride membrane and bottom reflector was 2 μm . The performances of bolometers are expressed in terms of device figures of merit such as responsivity (R_v), detectivity (D^*), thermal conductance (G) and temperature coefficient of resistance (TCR).

Thermal conductance G was measured less than 1 mbar with the relation between the thermal conductance G and bias current I_b :

$$\frac{1}{R} = \frac{1}{R_0} - \frac{\alpha}{G} I_b^2 \quad (1)$$

Where R is resistance, R_0 is resistance at room temperature. The total thermal conductance (G) can be expressed as summation of thermal conductance of supporting legs (G_{leg}), gas (G_{gas}) and material radiation (G_{rad}): $G = G_{\text{leg}} + G_{\text{gas}} + G_{\text{rad}}$. The measurement of G is easily influenced on the vacuum condition. Without vacuum condition, G can be more than 10^{-5} W/K under atmosphere pressure owing

to air flow, which is not good for detector performance. Thus, a proper vacuum condition is necessary. The thermal time constant τ is the relation of thermal conductance G and thermal capacitance C of the device, expressed as:

$$\tau = \frac{C}{G} \quad (2)$$

And responsivity of detector is defined as:

$$R_v = \frac{\alpha \eta I_b R_0}{G \sqrt{1 + \omega^2 \tau^2}} \quad (3)$$

where α is temperature coefficient of resistance described as $\alpha = \Delta R/R\Delta T$. η is infrared absorptivity; I_b is bias current applied to device; R_0 is bolometer resistance at room temperature; G is the thermal conductance; τ is thermal time constant; ω is modulation frequency. Δf is test bandwidth; A_d is effective area of absorber, V_n is signal noise. Detectivity D^* is defined as:

$$D^* = \frac{R_v \sqrt{A_d \Delta f}}{V_n} \quad (4)$$

From the above equations, we know that a design of the bolometer with the low thermal conductance and a use of the material with the high TCR and the low resistance are essential for obtaining the high-performance bolometer.

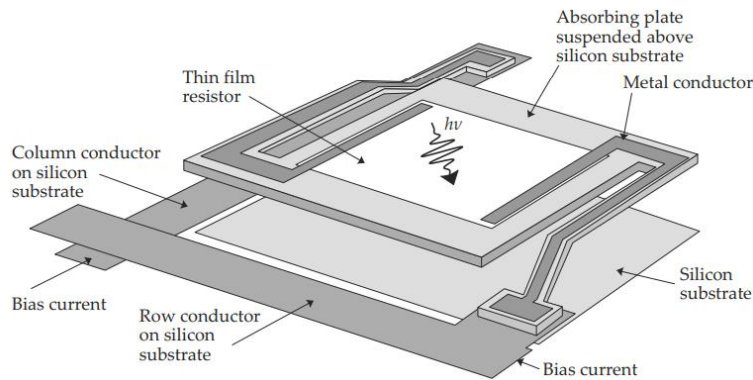


Figure 1. Schematic of microbolometer structure

2.2 Characteristic of vanadium oxide

2.2.1 Metal insulation transition (MIT) of vanadium oxide nanowire

The material containing electrons with strong electron-electron interaction is called strongly correlated material. It has interaction between spin, charge and orbital degrees of freedom. This interaction makes strongly correlated electron systems very sensitive to small changes in various external parameters, such as pressure, doping or temperature. As the transition metal combines with oxygen, various metal oxides are formed. In particular, metals (i.e. V, Cu, Fe, Cr, Co, Ni and Mn) make correlated materials. This correlated materials are characterized by MIT, colossal magnetoresistance, battery materials, thermoelectrics and high temperature superconductors. VO_2 is the one of the correlated material with

metal-insulator transition characteristics. Metal–insulator transitions are transitions from a metal to an insulator. VO_2 is abruptly changes from the monoclinic structure to rutile structure at a temperature of about 68°C , thereby rapidly reducing the resistance¹. The transition characteristic changes in the optical reflectivity, lattice structure and electrical conductivity. The transition could be applied for various device applications (i.e. Mott transistors, optical switches, strain sensor, thermochromic coating and gas sensors). However, there are considerable problems in designing the MIT of VO_2 for these device applications. Especially, strain related with substrate clamping, stoichiometry, grain boundaries and dislocations raise the known problem of phase heterogeneity in which multiple insulator domains and metal coexist over a wide range of temperatures². This makes the extensive phase transition and diffusion. In this regard, monocrystalline VO_2 nanowires provide an attractive alternative because they host a single domain across the entire width to support single or minority domain MIT³. Moreover, property of the MIT physics are discovered from these VO_2 nanowires, and device applications such as actuators⁴, sensors⁵, power meters⁶, and strain gauges⁷ are demonstrated.

Several methods for manufacturing nanowires have been reported⁸, including liquid self-assembly and casting growth in nanometer-sized pores. One of the most typically used methods is physical vapor transport or chemical vapor deposition (CVD). Here, a solid sample can be heated in a tube furnace in vacuum or flowing gas in a tube furnace to form a gas, which cause crystalline nanowire growth in the downstream part. The mechanisms of growth are similar to sublimation and may resemble recrystallization (also known as vapor-solid (VS) growth)^{9, 10}. Alternatively, nanometer sized metal particles can be used as catalysts for nanowire growth. At this time, the metal particles can be melted to form a eutectic solution with the precursor. The solid nanowires are crystallized to saturate the solution by adsorbing and dissolving the precursor on the metal catalyst. This mechanism of growth is called vapor-liquid-solid (VLS)¹¹ or “metal catalytic” growth. Recently, it has been demonstrated that solid catalyst particles can also be used to catalysts for nanowire growth by a vapor-solid-solid (VSS) mechanism¹². Both VLS and VSS need to grow nanowires using catalysts.

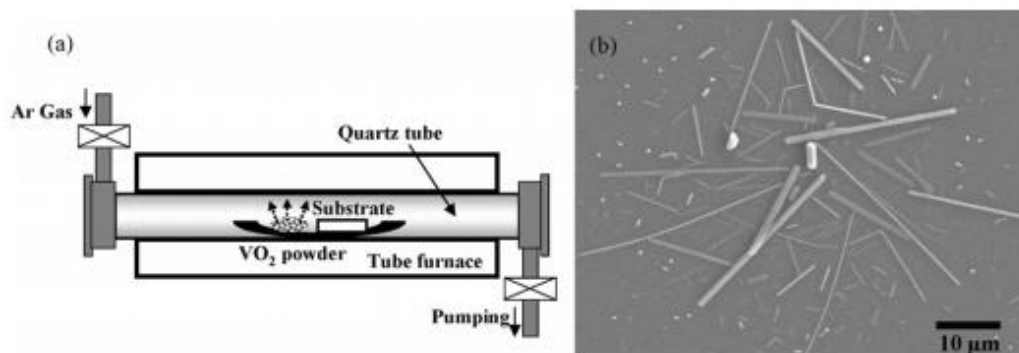


Figure 2. (a) Schematic of nanowire growth. (b) SEM image of VO_2 nanowires grown at 900°C on $\text{Si}_3\text{N}_4/\text{Si}$ substrate³⁸.

2.2.2 Metal insulation transition (MIT) based strain sensor

There are various mechanical/physical sensors for monitoring pressure, strain in human body. Especially, strain sensors give us specifically mechanical deformation in human body to measure and analyze the indices and their variation of electrical properties in active layers *i.e.* capacitance, resistance and even piezo-/triboelectric output performance of various devices. In order to fabricate highly superior strain sensors, many critical requirements should be considered such as cost and simplicity in procedure to fabricate, sensitivity (*i.e.*, gauge factor (GF)), response time, stability and stretchability. The GF is a ratio of variation in electrical resistance ($\Delta R/R_0$) under the mechanical strain and it was commonly used to evaluate the performance of the strain sensors. Generally, strain sensors request low fabrication cost, but have sensitivity and poor stretchability. Recently, various applications of flexible/stretchable strain sensors such as rehabilitation therapy monitoring¹³, health monitoring¹⁴, sports performance monitoring¹⁵ and human motion capturing for entertainment systems¹⁶ have been widely investigated. And a highly stretchable/sensitive strain sensor is quite essential for biomechanical, physiological and even kinetic applications. VO₂ has an unique electrical property which is transition of crystal structure at room temperature under high pressure along the [110] direction of the rutile phase and even doping a high composition of Cr on the initial insulation (M1 insulator) converts it on other stabilized insulators (M2 insulator), which are respectively well-known as a monoclinic M1 and M2 phase transition¹⁷. Unlike the abrupt change from the brightly reflecting M phase to the darkly reflecting R phase with respect to the transition temperature, the M1-M2 transition is difficult to observe with an optical microscope. Recently, the phase transition of a single heated VO₂ nanobeam was observed and used to correlate with the electrical properties of the nanobeam. In the crystalline structure, the M phase and R phase in the VO₂ nanobeam showed the highly sensitive to internal stress. In the peak position of M1 phases and M2 phases, the appearance and shifts have been used to observe and related to the phase transition caused by the applied strain¹⁸. Characteristic of MIT has already been developed to make sensitive transition sensors and quick optical shutters¹⁹. The transition between the M1 and M2 insulator can be used to developing reproducible and fast strain sensors and logic switches.

2.3 Application for enhancing light absorption

2.3.1 Solar thermal absorber for enhancing thermoelectric generator (TEG) efficiency

A thermoelectric (TE) material produces a voltage with a temperature gradient. The efficiency of a thermoelectric material is determined by zT factor, defined as $zT = a^2T/k\rho$. Here, a is the Seebeck coefficient, k is the thermal conductivity, and r is the electrical resistivity. Thermoelectric materials had reported zT values of 0.5–0.8, resulting in low conversion efficiency and limiting these materials to various applications²⁰. The total power conversion efficiency of a thermoelectric generate (TEG) can be represented as the product of thermoelectric efficiency, which expressed the efficiency of converting

light energy into heat to electric energy and photo-thermal efficiency. In order to increase the photo-thermal efficiency, hot parts of TE module receiving light energy should be applied with a light absorbing materials. Mostly dark colored materials can be applied as light absorbing materials, such as metal oxide and sulfides²¹. Graphitic carbon such as graphite and glassy carbon, have been demonstrated to be good light absorbers²². Also, carbon nanotube (CNT) based composites were used to enhance thermoelectric efficiency²³.

2.3.2 Antireflective layer for enhancing performance of solar cell

Antireflection coatings play an important role in improving the efficiency of photovoltaic devices by increasing the optical coupling of the devices to the active area. Antireflection coatings are a type of optical coating that is applied to the surface of optical elements to reduce reflections. By using alternating layers of low refractive index materials and high refractive index materials, low reflection at a single wavelength can be obtained. During the past few decades, research has been studied to enhance the efficiency of solar cell. Especially, there are many studies to make antireflection film with nanostructure. Many groups have demonstrated surface textured by anisotropic etching²⁴, etching via patterned masks^{25, 26}, and through other skill that make porosity and roughness^{27, 28} on lithographically patterned Si PV devices. However, various experimental parameters (i.e. growth time, substrates, amounts of precursors, additives and temperature) should be considered for the precise control of the diameter of nanowire. In nanostructure, light rays are captured in a gaps induces a number of internal reflections. Thus, the incident radiation can be clearly absorbed and the reflection in the visible range is reduced very low. So, antireflection coatings on solar cells could decrease the reflection. And it is possible to improve the absorption of light in the absorption wavelength band for almost all incident directions.

2.4 Reference

- [1] Eyert, V. The metal-insulator transitions of VO₂: A band theoretical approach. *Ann Phys. (Berlin, Ger.)* **2002**, 11, 650a.
- [2] Cao, J.; Wu, J. Strain effects in low-dimensional transition metal oxides. *Mater. Sci. Eng.* **2011**, 71, 35.
- [3] Cao, J.; Ertekin, E.; Srinivasan, V.; Fan, W.; Huang, S.; Zheng, H.; Yim, J. W. L.; Khanal, D. R.; Ogletree, D. F.; Grossman, J. C.; Wu, J. Strain engineering and one-dimensional organization of metal-insulator domains in single-crystal vanadium dioxide beams. *Nat. Nanotechnol.* **2009**, 4, 732.
- [4] Gu, Y.; Cao, J.; Wu, J.; Chen, L.-Q. J. Thermodynamics of strained vanadium dioxide single crystals. *Appl. Phys.* **2010**, 108, 083517.
- [5] Strelcov, E.; Lilach, Y.; Kolmakov, A. Gas Sensor Based on Metal-Insulator Transition in VO₂ Nanowire Thermistor. *Nano Lett.* **2009**, 9, 2322.
- [6] Cheng, C.; Fan, W.; Cao, J.; Ryu, S.-G.; Ji, J.; Grigoropoulos, C. P.; Wu, J. Heat transfer across the interface between nanoscale solids and gas. *ACS Nano.* **2011**, 5, 10102.
- [7] Hu, B.; Ding, Y.; Chen, W.; Kulkarni, D.; Shen, Y.; Tsukruk, V. V.; Wang, Z. L. External-Strain Induced Insulating Phase Transition in VO₂ Nanobeam and Its Application as Flexible Strain Sensor. *Adv. Mater.* **2010**, 22, 5134.
- [8] Whitney, T. M.; Jiang, J. S.; Searson, P. C.; Chien, C. L. Fabrication and magnetic properties of arrays of metallic nanowires. *Science.* **1993**, 261, 1316.
- [9] Pan, Z. W.; Dai, Z. R.; Wang, Z. L. Nanobelts of semiconducting oxides. *Science* **2001**, 291, 1947.
- [10] Persson, A. I.; Larsson, M. W.; Stenstrom, S.; Ohlsson, B. J.; Samuelson, L.; Wallenberg, L. R. Solid-phase diffusion mechanism for GaAs nanowire growth. *Nat. Mater.* **2004**, 3, 677.
- [11] Wagner, R. S.; Ellis, W. C. Vapor-liquid-solid mechanism of single crystal growth. *Appl. Phys. Lett.* **1964**, 4, 89.
- [12] Kodambaka, S.; Tersoff, J.; Reuter, M. C.; Ross, F. M. Germanium nanowire growth below the eutectic temperature. *Science.* **2007**, 316, 729.
- [13] Liu, C. X.; Choi, J. W. An Embedded PDMS Nanocomposite Strain Sensor toward Biomedical Application. *31st Ann. Int. Conf. IEEE EMBS* **2009**, 6391–6394.
- [14] Zhang, J.; Liu, J.; Zhuang, R.; Mäder, E.; Heinrich, G.; Gao, S. Single MWNT-Glass Fiber as Strain Sensor and Switch. *Adv. Mater.* **2011**, 23, 3392–3397.
- [15] Helmer, R. J. N.; Farrow, D.; Ball, K.; Phillips, E.; Farouil, A.; Blanchonette, I. A Pilot Evaluation of an Electronic Textile for Lower Limb Monitoring and Interactive Biofeedback. *Procedia Eng.* **2011**, 513–518.
- [16] Lu, N.; Lu, C.; Yang, S.; Rogers, J. Highly Sensitive SkinMountable Strain Gauges Based Entirely

- on Elastomers. *Adv. Funct. Mater.* **2012**, 22, 4044–4050.
- [17] Pouget, J. P.; Launois, H.; J. Dhaenens.; P. Merenda, P.; Rice, T. M. Electron Localization Induced by Uniaxial Stress in Pure VO₂. *Phys. Rev. Lett.* **1975**, 35, 873.
- [18] Jones, A. C.; Berweger, S.; Wei, J.; Cobden, D.; Raschke, M. B. Nano-optical Investigations of the Metal–Insulator Phase Behavior of Individual VO₂ Microcrystals. *Nano Lett.* **2010**, 10, 1574.
- [19] Strelcov, E.; Lilach, Y.; Kolmakov, A. Gas Sensor Based on Metal–Insulator Transition in VO₂ Nanowire Thermistor. *Nano Lett.* **2009**, 9, 2322.
- [20] Wood, C. Materials for thermoelectric energy conversion, *Rep. Prog. Phys.*, **1988**, 51, 459–539.
- [21] Wackelgard, E. Characterization of black nickel solar absorber coatings electroplated in a nickel chlorine aqueous solution. *Sol. Energy Mater. Sol. Cells*, **1998**, 56, 35–44
- [22] Harding, G. L.; Craig, S. Composition and degradation of graded metal-carbon solar selective absorbing surfaces. *Sol. Energy Mater.*, **1981**, 4, 413–420.
- [23] Miyako, E.; Hosokawa, C.; Kojima, M.; Yudasaka, M.; Funahashi, R.; Oishi, I.; Hagihara, Y.; Shichiri, M.; Takashima, M.; Nishio K.; Yoshida, Y. Melt electrospun reduced tungsten oxide/polylactic acid fiber membranes as a photothermal material for light-driven interfacial water evaporation. *Angew. Chem., Int. Ed.*, **2011**, 12266–12270.
- [24] Green, M. A. Silicon Solar Cells: Advanced Principles and Practice; Bridge: Sydney, **1995**.
- [25] Koynov, S.; Brandt, M. S.; Stutzmann, M. Black nonreflecting silicon surfaces for solar cells. *Appl. Phys. Lett.* **2006**, 88, 203107.
- [26] Sun, C. H.; Jiang, B.; Jiang, P. Broadband moth-eye antireflection coatings on silicon. *Appl. Phys. Lett.* **2008**, 92, 061112.
- [27] Striemer, C. C.; Fauchet, P. M. Dynamic etching of silicon for broadband antireflection applications. *Appl. Phys. Lett.* **2002**, 81, 2980.
- [28] Ruby, D. S.; Zaidi, S. H.; Narayanan, S.; Damiani, B. M.; Rohatgi, A. Rie-texturing of multicrystalline silicon solar cells. *Solar Energy Materials and Solar Cells.* **2002**, 74, 133.

CHAPTER 3. Experimental Procedure

3.1 VO₂ based Micro-bolometer with infrared absorbing layer

We fabricated the micro-bolometer device by applying VO₂ (B) and absorber. A schematic diagram of fabrication of the microbolometer is shown in Figure 3. We proceeded with the commonly used bolometer process. Au film (250 nm) as reflector was deposited by sputter and patterned by photolithography onto SiN film we deposited. And then, polyimide (PI 2610) as sacrificial layer was spin-coated and cured at 350°C. This is for patterning and making the anchor areas. After that, 300 nm of silicon nitride (SiN) film was deposited using plasma enhanced chemical vapor deposition (PECVD). Holes were etched to be open by reactive ion etching (RIE). After formation of the via holes, 5 nm of strontium titanate (STO) buffer layer and 40 nm of vanadium oxide thin film were deposited using sputter. Via holes through the VO₂/STO thin film were formed using RIE. After formation of via holes, then, Cr (100 nm)/Au (50 nm) were deposited and those areas were patterned to connect bottom pad. Then, SiN (300 nm) were deposited using PECVD again, Then, another SiN with thickness of 300 nm was deposited for the passivation. The Ti/MgF₂ multi-layer with thickness of 10/320 nm as absorbing layer was deposited by electron beam evaporator (KVE-T8897) at room temperature. Finally, polyimide sacrificial layer was removed by oxygen plasma ashing. The SEM image of micro-bolometer with pixel size of 70 μm × 70 μm is shown in Figure 6. The size of active layer is 25 μm × 25 μm. As can be seen from the image, the suspended structure for infrared sensor was fabricated successfully. For the IR absorption measurement, the spectra were acquired with a Fourier transform infrared (FTIR) spectrophotometer (Vertex 80v) in the range of 2.5–13 μm. FTIR spectra were measured using a 10° specular reflectance accessory and a gold substrate alignment mirror at room temperature and the spectral resolution was approximately 0.9 cm⁻¹.

3.2 Directional Ostwald ripening for producing aligned arrays of nanowires

V-grooved SiO₂/Si substrates were fabricated by potassium hydroxide (KOH) etching. The native oxide on the Si (100) substrates was removed by buffered oxide etchant (BOE) and 500 nm-thick SiO₂ layer was deposited by using plasma-enhanced chemical vapor deposition (PECVD) to be used as a shadow mask for the wet etching process. By using a photomask having line patterns of pitch size from 2 to 6 μm and conventional lithography process, line patterns of photoresist (PR) were obtained. By reactive ion etching (RIE) process, the SiO₂ was selectively etched away, resulted in the formation of the line patterned SiO₂ on Si substrate. The sample was dipped in 45 % KOH solution for 1 h at 80°C to carry out the anisotropic wet etching, producing V-groove templates with different angles of the grooves, as shown in Figure 17. By changing the etching time, the morphology of the templates could be also controlled. The etched sample was subsequently dipped in the diluted hydrofluoric acid (HF:H₂O = 1:1) at room temperature to remove the SiO₂ etch mask layer. SiO₂ and V₂O₅ thin films were

deposited on the V-grooved Si substrate using PECVD and sputtering. (DC, 100W, Ar O₂ 30:11 sccm, 5 mTorr, 400° C 2h 200nm); VO₂ nanowires were grown by CVD without using any catalysts. Before heating the source material, the furnace tube was evacuated to about 10⁻³ Torr; the furnace temperature was increased at a rate of 18°C/min to a final temperature of ~ 750°C which was maintained for 2 h. A constant flow of high purity helium (1000 sccm) was maintained in the chamber throughout the experiment. The optimal deposition temperature was found to be between 700 °C and 750°C. The size distribution, lattice structure, and crystal orientation of the as-synthesized products were characterized by scanning electron microscopy (SEM), x-ray diffraction (XRD), and transmission electron microscopy (TEM).

In order to completely separate the VO₂ nanowire and the SiO₂ from the SiO₂/Si substrate, it was etched by BOE for 1 hour and rinsed with deionized water. The PDMS was prepared by mixing the liquid PDMS elastomer and a curing agent in the ratio 10:1 by weight. The liquid mixture was poured onto the VO₂ nanowire arrays grown on the Si substrates and thermally cured at 90°C for 30 min. After curing, the PDMS was peeled off the VO₂ nanowires array covered Si substrate, and Cr/Au (20/300 nm) electrodes were fabricated on the substrate across the VO₂ nanowires. A constant 1 V was applied to evaluate the performance of the strain sensor.

2.3 Solar absorbers with submicron-thick multilayer sheets

The samples, consisting of a layered metal/dielectric film structure, were fabricated by electron beam evaporator (KVE-T8897) at room temperature. The metal and dielectric films were deposited from targets of 99.99 % purity with a background pressure of 5.0×10^{-6} Torr. To control and adjust the layer thickness, the deposition rate of Ti and MgF₂ was calibrated in advance under the condition, 0.1 nm/s and 0.25 nm/s, respectively.

3.4 Optical design of ZnO-based antireflective layers for enhanced GaAs solar cell performance

High-aspect-ratio ZnO based double-nanotextured surfaces with core-shell morphologies were prepared via a hydrothermal method of ZnO nanowires and nanosheets, followed by means of RF sputtering for MgF₂ thin film deposition. For reflectance measurement of the antireflective surfaces, the nanowires were grown on ZnO/TiO₂ (100 nm/ 50 nm) and ZnO/ZnS (100 nm/ 50 nm) layers in a mixed solution of 0.020 M zinc nitrate hydrate and 0.020 M hexamethylenetetramine (HMT) in DI water for 9 hrs. The TiO₂ and ZnS were deposited by reactive sputtering using 80 W of RF power, 16 sccm of Ar and 4 sccm of O₂ at an operating pressure of 2 mTorr, and 50 W of RF power, 20 sccm of Ar at an operating pressure of 5 mTorr, respectively. The deposition condition was optimized to enhance good crystallinity. The ZnO, which acts effectively as the seed layer for growing ZnO nanowires, was then deposited by reactive sputtering using 100 W of RF power to the 2 in. ZnO target, 16 sccm (sccm denotes cubic

centimeter per minute at STP) of Ar and 4 sccm of O₂ at an operating pressure of 4 mTorr. For the growth of ZnO nanosheets, very thin layer of aluminum (0.5 to 3 nm) was deposited on the ZnS layer, followed by the growth of the ZnO nanosheets under the same growth condition. The MgF₂/ZnO was fabricated using 80 W of RF power to the 2 inch MgF₂ target, 15 sccm of Ar at an operating pressure of 25 mTorr.

CHAPTER 4. High Temperature VO₂ based Microbolometer with Enhanced Light Absorption

4.1 High temperature operation of VO₂ based micro-bolometer with infrared absorbing layer

4.1.1 Introduction

Many uncooled infrared (IR) detectors have been developed for many military and commercial applications, such as thermal sensors, night vision cameras, infrared cameras and surveillance devices. In particular, vanadium oxide-based microbolometer are the most widely used. Thermal sensor elements commonly used in commercial, uncooled thermal cameras. The merits of vanadium oxide (VO_x) uncooled microbolometer are suitable for low power consumption, room temperature operation, light weight and portable applications. Also, VO_x thin films are widely used due to high temperature resistance coefficients (TCR) and low noise. However, due to the metal-insulator-transition (MIT) property of the VO₂ thin film, it is difficult to fabricate a microbolometer at 68°C which can operate at high temperatures. Therefore, the commercial VO_x microbolometer operates mainly at room temperature and the TCR value of VO_x is 2 ~ 3%/K¹. Recently, TCR materials have been developed for obtain large TCR values such as VO_x/ZnO/VO_x multilayer², VVO layer³, and V₂O₅/V/V₂O₅ multilayer sandwich structure⁴.

In the case of infrared sensors, infrared absorber material is required inside the detector stack to perform absorption and then transfer heat to micro-bolometer because of thermal conduction. Infrared absorber materials have been used in the VO_x based microbolometer such as Titanium (Ti)⁵, silicon nitride (Si₃N₄)⁶, Titanium Nitride (TiN)⁷, Nichrome (NiCr)⁸ and gold black⁹. Most widely used gold black has very high absorption over a broad wavelength range. On the other hand, this low-density material is extremely fragile, which makes it difficult to integrate onto a micro-bolometer array, since usual fabrication processes destroy the film.

Here, we demonstrate optical absorption performance enhancement of vanadium oxide micro-bolometer with multi-layer infrared absorbing layer. Vanadium dioxide (VO₂) is deposited on the oxide thin film of perovskite structure. Thin VO₂ film is deposited using the reactive sputtering and TCR value is 3.4 %/K at room temperature and 1.46 %/K at 100°C. The measurement of the film system with Ti/MgF₂ absorbing layer indicates that it has about 70 % infrared absorption in the range of 8–14 μm. The infrared absorber of Ti/MgF₂ can be easily deposited using e-beam evaporation and shows broadband optical absorption and high thermal stability. All processes were fabricated under 350°C, which are compatible with read-out integrated circuit (ROIC) integration. By using thin VO₂ (B) film, micro-bolometer is operate at high temperature and obtain high responsivity because of infrared absorber. The micro-bolometer has a responsivity and detectivity of 4.90 x 10³ V/W and 1.45 x 10⁸ cmHz^{1/2}/W at 100°C.

4.1.2 Experimental

We fabricated the micro-bolometer device by applying VO₂ (B) and absorber. A schematic diagram of fabrication of the microbolometer is shown in Figure 3. We proceeded with the commonly used bolometer process. Au film (250 nm) as reflector was deposited by sputter and patterned by photolithography onto SiN film we deposited. And then, polyimide (PI 2610) as sacrificial layer was spin-coated and cured at 350°C. This is for patterning and making the anchor areas. After that, 300 nm of silicon nitride (SiN) film was deposited using plasma enhanced chemical vapor deposition (PECVD). Holes were etched to be open by reactive ion etching (RIE). After formation of the via holes, 5 nm of strontium titanate (STO) buffer layer and 40 nm of vanadium oxide thin film were deposited using sputter. Via holes through the VO₂/STO thin film were formed using RIE. After formation of via holes, then, Cr (100 nm)/Au (50 nm) were deposited and those areas were patterned to connect bottom pad. Then, SiN (300 nm) were deposited using PECVD again, Then, another SiN with thickness of 300 nm was deposited for the passivation. The Ti/MgF₂ multi-layer with thickness of 10/320 nm as absorbing layer was deposited by electron beam evaporator (KVE-T8897) at room temperature. Finally, polyimide sacrificial layer was removed by oxygen plasma ashing. The SEM image of micro-bolometer with pixel size of 70 μm × 70 μm is shown in Figure 6. The size of active layer is 25 μm × 25 μm. As can be seen from the image, the suspended structure for infrared sensor was fabricated successfully. For the IR absorption measurement, the spectra were acquired with a Fourier transform infrared (FTIR) spectrophotometer (Vertex 80v) in the range of 2.5–13 μm. FTIR spectra were measured using a 10° specular reflectance accessory and a gold substrate alignment mirror at room temperature and the spectral resolution was approximately 0.9 cm⁻¹.

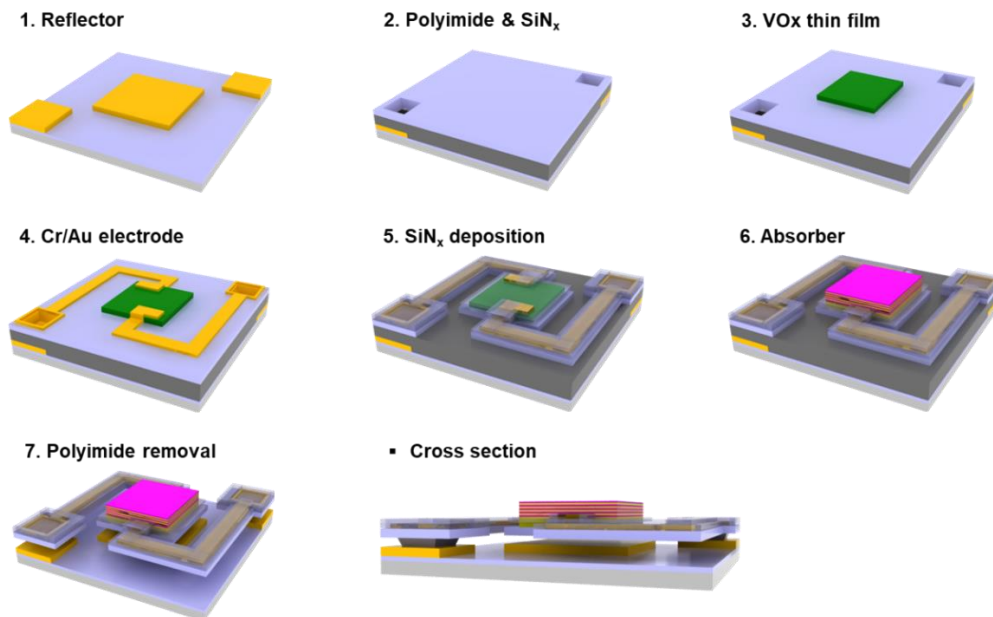


Figure 3. Fabrication process of micro-bolometer.

4.1.3 Result and discussion

VO₂ thin film design and characteristics

The resistors of the bolometer are required to have a large resistance change for small temperature changes, and at the same time they must be made of a low resistance material in order to reduce the noise of the bolometer, that is, Johnson noise. For the bolometer applications, vanadium oxide (VO_x) is widely used as it has a relatively large temperature coefficient of resistance (TCR) and can be deposited at low temperature. As Vanadium has multiple oxidation states, it can adopt a wide range of V:O ratio to form VO, VO₂, V₂O₃, V₂O₅, V₃O₇, V₄O₉, and V₆O₁₃. Moreover, each one can exhibit a number of polymorphic forms: for example, VO₂ can have three different crystal structures: tetragonal VO₂(A), monoclinic VO₂(B), and monoclinic VO₂(M) with a metal-insulator transition to tetragonal phase at high temperature (~68°C). Among these VO₂ polymorphs, VO₂(B) is the most promising candidate for the application of high temperature bolometer. First, the VO₂(B) phase is very stable in the temperature range from room temperature to ~100°C without any phase transition, and therefore, the electronic transport properties are continuously changing with temperature. On the other hand, VO₂(M) experience a metal-insulator-transition with a structural phase transformation at ~ 68°C. Near the room temperature, it is an insulator with a large temperature coefficient of resistance and high resistivity. Above 68°C, it transforms to a metal with a low temperature coefficient of resistance and low resistivity. Such a sudden change of electronic transport properties is detrimental to the precise and reliable operation of the high temperature bolometers. Second, the electronic transport property of VO₂(B) is very suitable to the bolometer operation. The temperature coefficient of VO₂(B) (>-3%/K) is larger, and the resistivity (<1 Ωcm) is lower than any other polymorphs. Moreover, even at high temperature, the temperature coefficient of resistance is still high (-1.5 %/K at 90°C) enough for bolometer operation.

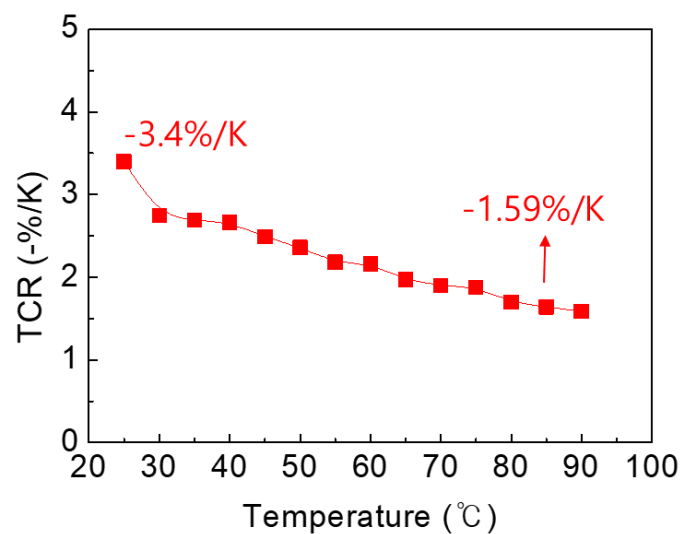


Figure 4. TCR value of VO₂(B) as a functional of temperature.

Absorber film characteristic

The absorber was mainly composed of titanium (Ti) metal and magnesium fluoride (MgF_2). As a key material for enhancing the adhesive property, a 10 nm thick Ti layer was deposited on the substrate via e-beam evaporation at a very low deposition rate of 0.1 nm/s. The dielectric film of 320 nm thick MgF_2 was then deposited on the Ti layer in the same way. Finally, the film consists of five stacks of alternating Ti and MgF_2 films, with a total thickness of approximately 1.65 μm . The light absorption of the multilayered film, composed of metal and dielectric layers, is based on the multiple reflections at the layer interfaces. After the light entering the film, the light is reflected back and forth at the interfaces. In general, the high absorption in the stack resulted from multipass of light through the dielectric layer. The reflected light should destructively interfere because of the phase difference between the alternating layers; thus, the reflected light is canceled. Thus, we optimized the thickness of each layer to enhance the destructive optical interferences of the reflected light¹⁰. IR absorption property was measured through FT-IR spectrometer. It is obvious that the film system was of good absorption in the wavelength range 8–14 μm as shown in figure 5. The average absorption of 8–14 μm is about 70%.

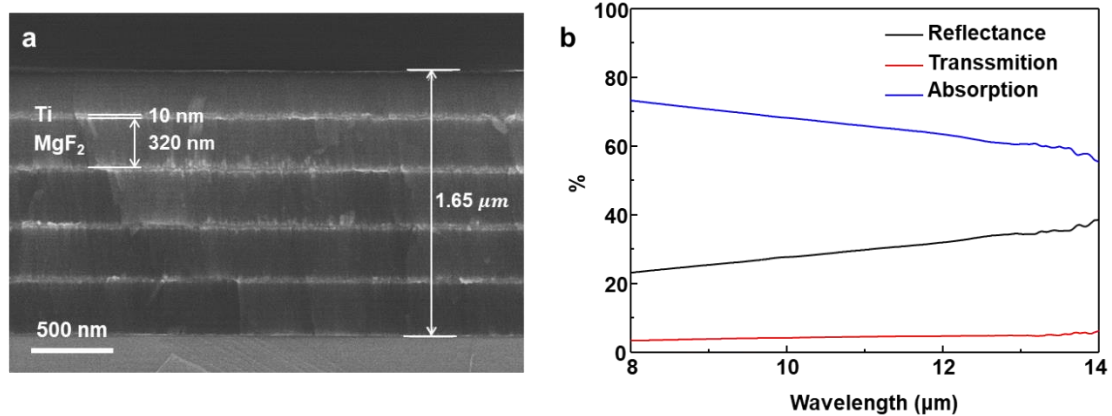


Figure 5. (a) SEM image of multi-layers infrared absorber and (b) Fourier transformed infrared spectroscopy (FT-IR) over a wavelength range from 8 to 14 μm .

Micro-bolometer design

Vanadium oxide was applied as thermal sensitive material. The suspended $\lambda/4$ cavity structure was designed to enhance the infrared light coupling¹¹. The gap of sacrificial layer between silicon nitride membrane and bottom reflector was 2 μm . The performances of bolometers are expressed in terms of device figures of merit such as responsivity (R_v), detectivity (D^*), thermal conductance (G) and temperature coefficient of resistance (TCR)¹².

Thermal conductance G was measured less than 1 mbar with the relation between the thermal conductance G and bias current I_b :

$$\frac{1}{R} = \frac{1}{R_0} - \frac{\alpha}{G} I_b^2 \quad (1)$$

Where R is resistance, R_0 is resistance at room temperature. The total thermal conductance (G) can be expressed as summation of thermal conductance of supporting legs (G_{leg}), gas (G_{gas}) and material radiation (G_{rad}): $G = G_{\text{leg}} + G_{\text{gas}} + G_{\text{rad}}$. The measurement of G is easily influenced on the vacuum condition. Without vacuum condition, G can be more than 10^{-5} W/K under atmosphere pressure owing to air flow, which is not good for detector performance. Thus, a proper vacuum condition is necessary. The thermal time constant τ is the relation of thermal conductance G and thermal capacitance C of the device, expressed as:

$$\tau = \frac{C}{G} \quad (2)$$

And responsivity of detector is defined as:

$$R_v = \frac{\alpha \eta I_b R_0}{G \sqrt{1 + \omega^2 \tau^2}} \quad (3)$$

where α is temperature coefficient of resistance described as $\alpha = \Delta R / R \Delta T$. η is infrared absorptivity; I_b is bias current applied to device; R_0 is bolometer resistance at room temperature; G is the thermal conductance; τ is thermal time constant; ω is modulation frequency. Δf is test bandwidth; A_d is effective area of absorber, V_n is signal noise. Detectivity D^* is defined as:

$$D^* = \frac{R_v \sqrt{A_d \Delta f}}{V_n} \quad (4)$$

From the above equations, we know that a design of the bolometer with the low thermal conductance and a use of the material with the high TCR and the low resistance are essential for obtaining the high-performance bolometer.

Detector characterization

Multi-layer infrared absorber was integrated into bolometer, as shown in the Figure 6 SEM image. Detector test system is shown in Figure 7. The detector was vacuum packaged in a chamber, which was pumped through a special pipeline. The black body which acts as infrared source radiated infrared rays through a hole with the diameter of 1 cm. The chopper controlled the modulation frequency. 8–14 μm Ge window was sets in front of the vacuum chamber, which acts as infrared spectrum filter so that only this infrared spectrum can get through. The bolometer was biased by current source. The lock-in amplifier and oscilloscope locked and showed the output signal. The modulation frequency was from 5 to 965 Hz. The black body temperature was controlled at 600°C. Vacuum pressure was pumped below 0.1 mbar. To compare with bolometer with absorber layer, the detector without absorber has been tested in which detector fabrication parameter was kept the same as the bolometer with absorber. Both IR bolometer test elements are fabricated with active area of $24 \times 26 \mu\text{m}^2$. Parameters with absorber have been compared with that without absorber and shown in Table 1 and 2.

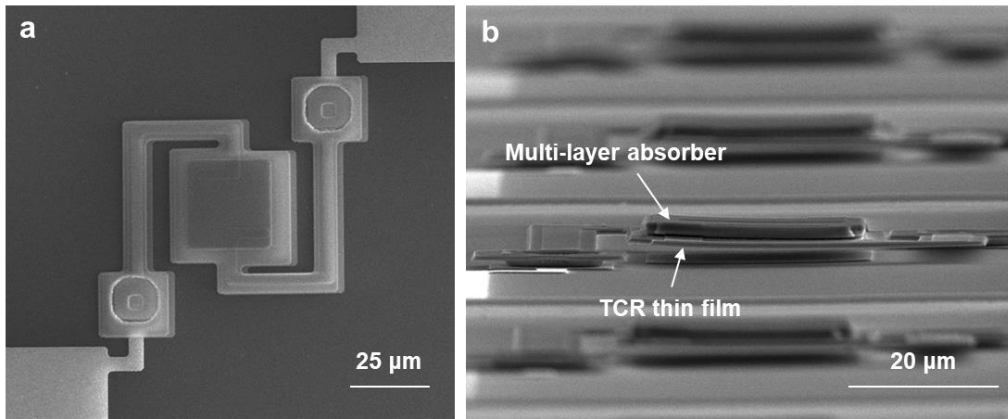


Figure 6. SEM image of micro-bolometer with VO₂(B) thin film and multi-layer infrared absorber.

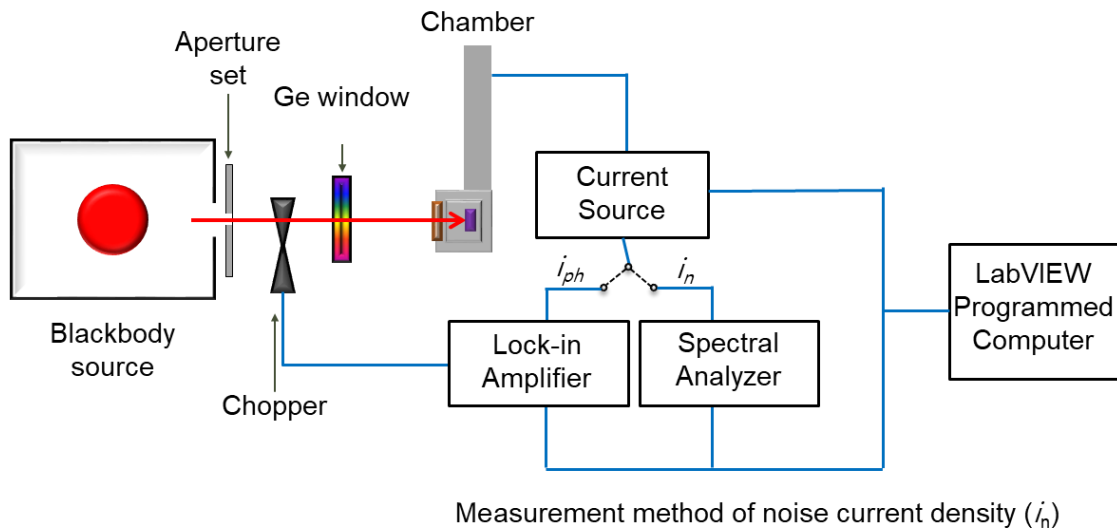


Figure 7. Schematic of micro-bolometer measurement system.

Figure 8 shows curves of the square of bias current vs. inverse of resistance. α/G was calculated 37,300 for bolometer with absorber (figure 8b) and 62,000 for bolometer without absorber (figure 8a), respectively. G was obtained to be about 5.42×10^{-7} W/K and 3.39×10^{-7} W/K in room temperature. So the G value of bolometer with absorber and without absorber was obtained to be about 2.10×10^{-7} W/K and 1.45×10^{-7} W/K at 100°C.

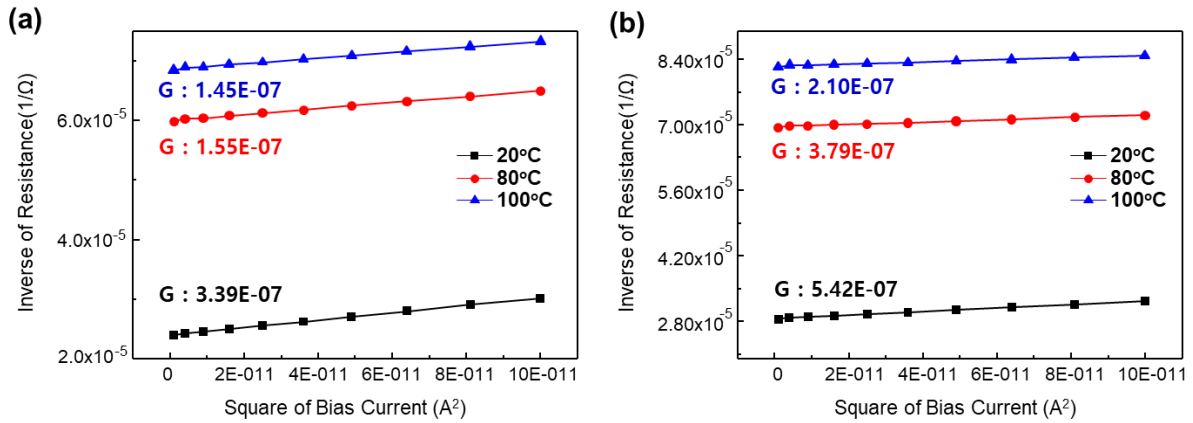


Figure 8. Inverse of resistance of micro-bolometer (a) without absorber and (b) with absorber as a functional of the square of bias current under various temperature.

We measured the responsivity dependence of frequency at 30 μ A for find 3dB frequency as shown in Figure 9. The fitting parameter τ and the just-determined value for G allow an estimate of heat capacity C using $\tau = C/G$. The C value of bolometer with absorber and without absorber was obtained to be about 1.88×10^{-9} W/K and 1.02×10^{-9} W/K in room temperature, respectively. 1.65 μ m thick layer of multi-layer absorber with 300 nm SiO₂ should add 0.87×10^{-9} J/K to the heat capacity, or a xx% increase, which is in reasonable agreement with the value obtained from the fit. Thus, the speed limitation of a device by the increase in heat capacity is small. As the temperature increase, the C value decrease because the G value increase. The C value of bolometer with absorber and without absorber was obtained to be about 7.60×10^{-10} W/K and 4.35×10^{-10} W/K at 100°C.

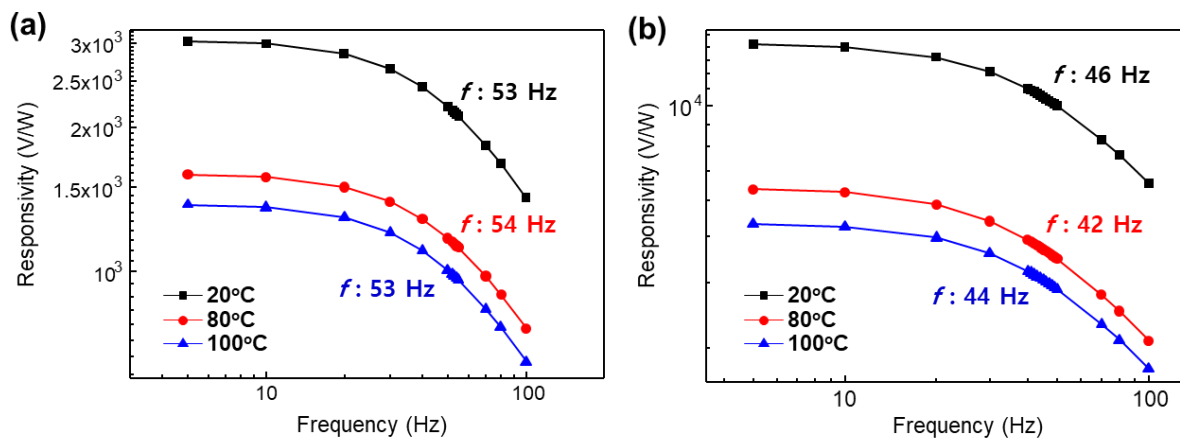


Figure 9. Responsivity of micro-bolometer (a) without absorber and (b) with absorber as a functional of frequency under various temperature.

Figure 10 shows the curves of responsivity, R_v , and noise dependence on bias current. It shows that

the micro-bolometer with absorber has better performance than micro-bolometer without absorber. As the current increased, both bolometer responsivity and noise voltage increased. The bolometer with absorber has reached responsivity of about 1.24×10^4 V/W while the other was 2.65×10^3 V/W at 30 μ A bias current, 30 Hz frequency. Bolometer vanadium oxide thin film noise with absorber has basically the same change with current comparing with the other one. The higher the temperature, the lower the responsivity of the micro-bolometer. However, due to the characteristics of the VO₂ (B) thin film, it operates up to 100°C. At 100°C, the bolometer with absorber has reached responsivity of about 4.90×10^3 V/W while the other was 1.21×10^3 V/W at 30 μ A bias current, 30 Hz frequency.

Table 1. Micro-bolometer parameters at room temperature.

Detector parameters	Without absorber	With absorber
Pixel size (μm^2)	24 X 26	24 X 26
Element resistance (K Ω)	40	40
TCR (%/K)	3.4	3.4
Depth of cavity (μm)	2.2	2.2
G (W/K)	3.39E-7	5.42E-7
τ (ms)	3.00	3.46
C (J/K)	1.02E-9	1.88E-9

Table 2. Micro-bolometer parameters at 100°C

Detector parameters	Without absorber	With absorber
Pixel size (μm^2)	24 X 26	24 X 26
Element resistance (K Ω)	15	15
TCR (%/K)	1.46	1.46
Depth of cavity (μm)	2.2	2.2
G (W/K)	1.45E-7	2.10E-7
τ (ms)	3.00	3.62
C (J/K)	4.35E-10	7.60E-10

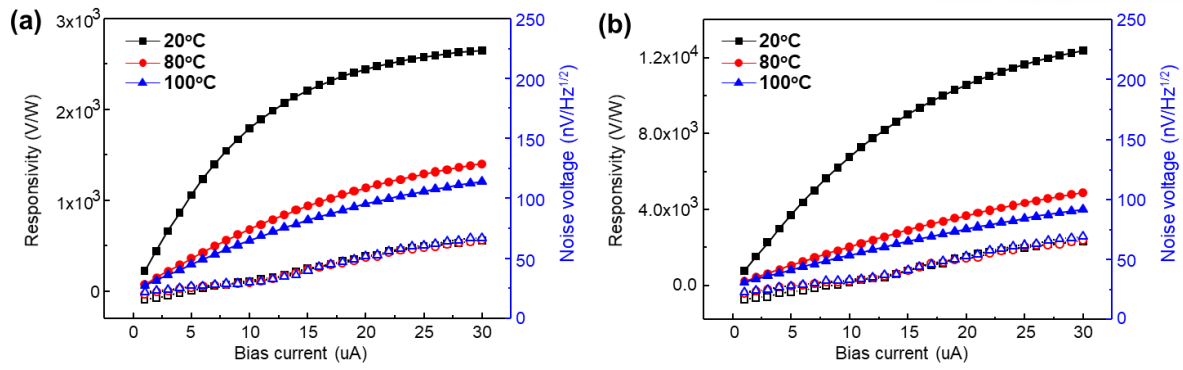


Figure 10. Responsivity and noise voltage of micro-bolometer (a) without absorber (b) with absorber as a functional of bias current under various temperature.

In Figure 11, it shows the trend that detectivity increased as current increased, while bolometer with absorber reached the acme of $5.86 \times 10^8 \text{ cmHz}^{1/2}/\text{W}$ at $13 \mu\text{A}$ and the other one is $1.46 \times 10^8 \text{ cmHz}^{1/2}/\text{W}$ at $12 \mu\text{A}$ in room temperature. At 100°C , the bolometer with absorber has reached detectivity of about $1.45 \times 10^8 \text{ cmHz}^{1/2}/\text{W}$ at $30 \mu\text{A}$ and the other one is $5.13 \times 10^7 \text{ cmHz}^{1/2}/\text{W}$ at $14 \mu\text{A}$. We consider that VO_2 (B) thin film and multi-layer absorber played good roles of high TCR value and absorption in this device.

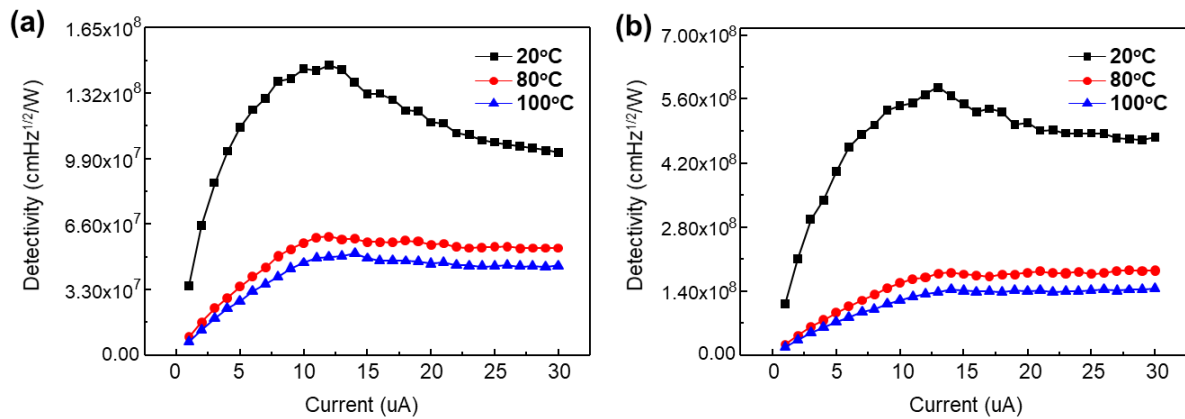


Figure 11. Detectivity of micro-bolometer (a) without absorber (b) with absorber as a functional of bias current under various temperature.

4.1.4 Conclusion

In summary, we demonstrate optical absorption performance enhancement of vanadium oxide micro-bolometer with infrared absorbing layer. At room temperature, high TCR vanadium oxide thin film of 3.4 %/K for micro-bolometer applications has been achieved by growing buffer layer of STO and VO_2 with the method of RF sputtering. It has nanostructured crystalline. Comparing with common VO_x thin film without annealing, micro-bolometer with VO_2 (B), has a significant improvement of

performance. Also, it has about 70 % infrared absorption in the range of 8–14 μm . At 100°C, we got responsivity and detectivity of $4.90 \times 10^3 \text{ V/W}$ and $1.45 \times 10^8 \text{ cmHz}^{1/2}/\text{W}$. The performance of this bolometer, comparing with that of common bolometer, has a better result. We consider that it can apply in various fields such as a heat generation environment.

4.1.5 Reference

- [1] Wood, R.A. Uncooled Thermal Imaging with Monolithic Silicon Focal Arrays. *Infrared Technology XIX, Proc. SPIE*. **1993**, 2020, 322-329.
 - [2] Han, M.-S.; Kim, D. H.; Koa, H. J.; Kim H. Vanadium Oxide Microbolometer Using ZnO Sandwich Layer. *ASCT*. **2015**, 24, 178-183.
 - [3] Chi-Anh, N.; Shin, H.-J.; Kim, K.; Han, Y.-H.; Moon, S. Characterization of uncooled bolometer with vanadium tungsten oxide infrared active layer. *Sens. Actuators A, Phys.* **2005**, 123-124, 87-92.
 - [4] Han, Y.-H.; Choi, I.-H. Fabrication of a Surface Micromachined Uncooled Microbolometer Based on the $V_2O_5/V/V_2O_5$ Sandwich Structure. *JKPS*, **2004**, 45, 1655-1658.
 - [5] Cheng, Q.; Paradis, S.; Bui, T.; Almasri, M. Design of dual-band uncooled infrared micro bolometer. *IEEE Sensors J.* **2011**, 11, 167–175.
 - [6] Wang, L.-X.; Li, X.-A. Preparation of VO_2 microbolometer for CO_2 gas detection. *In Proc. Int. Conf. Microw. Millim. Wave Technol. (ICMMT)*, **2010**, 1774–1777.
 - [7] Chi-Anh, N.; Shin, H.-J.; Kim, K.; Han, Y.-H.; Moon, S. Characterization of uncooled bolometer with vanadium tungsten oxide infrared active layer. *Sens. Actuators A, Phys.* **2005**, 123–124, 87–92.
 - [8] Awad, E.; Al-Khalli, N.; Abdel-Rahman, M.; Debbar, N. Comparison of V_2O_5 Microbolometer Optical Performance Using NiCr and Ti Thin-Films. *IEEE Photonics Technology Letters*, **2014**, 27, 462-465.
 - [9] Wang, B.; Lai, J.; Zhao, E.; Hu, H.; Liu, Q.; Chen, S. Vanadium oxide microbolometer with gold black absorbing layer. *Opt. Eng.* **2012**, 51, 074003.
 - [10] Lee, H. J.; Jung, D.-H.; Kil, T.-H.; Kim, S. H.; Lee, K.-S.; Baek, S. -H.; Choi, W. J.; Baik, J. M. Mechanically Robust, Stretchable Solar Absorbers with Submicron-Thick Multilayer Sheets for Wearable and Energy Applications. *ACS Appl. Mater. Interfaces*. **2017**, 9, 18061–18068.
 - [11] Liddard, K. C. Application of interferometric enhancement to self-absorbing thin film thermal IR detectors, *Infrared Physics*. **1993**, 34, 379–387.
- Wang, B.; Lai, J.; Li, H.; Hu, H.; Chen, S. Nanostructured vanadium oxide thin film with high TCR at room temperature for micro-bolometer. *Infr. Phys. Technol.* **2013**, 57, 8–13.

4.2 Directional Ostwald ripening for producing aligned arrays of nanowires

4.2.1 Introduction

Today's engineers envision miniaturized circuits interconnected by nanowires with specialized electronic¹⁻⁴, photonic⁵⁻⁸, energy conversion^{9,10}, gas sensing^{11,12}, and biosensing^{13,14} properties. Unlike conventional wires, nanowires must be grown using physical and chemical processes such as liquid-phase self-assembly¹⁵, templated growth in nanometer-size pores¹⁶, and chemical vapor deposition¹⁷⁻¹⁹. Fabrication of circuits with nanometer scale control requires growth processes that can precisely position and align nanowires and produce them with highly uniform dimensions. This remains a largely unsolved problem. A clue to a solution comes from the studies of vanadium dioxide (VO₂) nanowire growth²⁰. A previous study showed that a V₂O₅ film heated on a SiO₂ substrate at a temperature substantially below the melting point of V₂O₅ dewets and forms supercooled liquid nanodroplets that spontaneously form randomly distributed single crystal VO₂ nanowires with uniform dimensions. Nanowires composed of the oxides of molybdenum, ruthenium, and iron were also produced by a mechanism that involves supercooled nanodroplet mobility, coalescence and Ostwald ripening²⁰.

In this paper, we show that highly uniform, self-aligned and millimeter-long VO₂ nanowires can be produced by the supercooled nanodroplet growth mechanism on a textured growth substrate. "We employed the V-groove surface as an example to demonstrate *directional* Ostwald ripening for the self-alignment of the nanowires on the millimeter length scale. We believe that the method described here has great potential for the fabrication of aligned and highly uniform nanowires of a wide range of materials on any nonplanar substrate. In previous studies, the V-groove substrates were also used as simple templates, such as a shadow mask to obtain a significant shadowing effect²¹, and as the vessel for the assembly of polystyrene spheres into the V-grooves²² in order to fabricate metallic nanostructures. Regarding the growth mechanism, it was found that the segregation of group III atoms underlying the formation of the wires was driven by the characteristic faceting of the growth front at the bottom of the V-groove oriented in the specific crystal direction²³⁻²⁷. By contrast, our unique strategy involved growing the uniform and aligned one-dimensional millimeter-long nanostructures driven by the directional Ostwald Ripening process and nanodroplet coalescence from the dewetting of the V₂O₅ film through the guidance by the V-groove." To illustrate our growth process, we study the underlying melt droplet transport using molecular dynamics simulations of simple spherical particles interacting through Lennard-Jones potentials. These simulations show how surface morphology can be used to control nanowire growth by *directional* Ostwald Ripening and nanodroplet coalescence. We demonstrate the utility of this approach by producing horizontally aligned VO₂ nanowires from which we fabricated highly sensitive strain sensor arrays through chemical transfer onto a polymer substrate. The methods described here have the potential to produce aligned and highly uniform nanowires for a wide range of materials.

4.2.2 Experimental

VO₂ nanowire growth

For the growth of the VO₂ nanowires, thin V₂O₅ films were initially deposited onto a 200nm thick, thermally grown SiO₂ layer on a Si(100) single crystal substrate in an RF reactive sputtering chamber with a Vanadium target (99.99%), flowing argon/oxygen mixtures at an operating pressure of 2×10^{-6} torr and substrate temperature of 500°C. The thickness of the thin films was controlled in the approximate range 20 nm to 60 nm by adjusting the deposition time. The thin film was then transferred to the center of a horizontal quartz tube furnace to grow VO₂ nanowire growth at atmospheric pressure. Nanowire growth was carried out for 3 hours at 650°C with flowing high purity He (99.999%) at 200 sccm.

Fabrication of VO₂ nanowire array

V-grooved SiO₂/Si substrates were fabricated by potassium hydroxide (KOH) etching. The native oxide on the Si (100) substrates was removed by buffered oxide etchant (BOE) and 500 nm-thick SiO₂ layer was deposited by using plasma-enhanced chemical vapor deposition (PECVD) to be used as a shadow mask for the wet etching process. By using a photomask having line patterns of pitch size from 2 to 6 μm and conventional lithography process, line patterns of photoresist (PR) were obtained. By reactive ion etching (RIE) process, the SiO₂ was selectively etched away, resulted in the formation of the line patterned SiO₂ on Si substrate. The sample was dipped in 45 % KOH solution for 1 h at 80°C to carry out the anisotropic wet etching, producing V-groove templates with different angles of the grooves, as shown in Figure 17. By changing the etching time, the morphology of the templates could be also controlled. The etched sample was subsequently dipped in the diluted hydrofluoric acid (HF:H₂O = 1:1) at room temperature to remove the SiO₂ etch mask layer. SiO₂ and V₂O₅ thin films were deposited on the V-grooved Si substrate using PECVD and sputtering. (DC, 100W, Ar O₂ 30:11 sccm, 5 mTorr, 400° C 2h 200nm); VO₂ nanowires were grown by CVD without using any catalysts. Before heating the source material, the furnace tube was evacuated to about 10⁻³ Torr; the furnace temperature was increased at a rate of 18°C/min to a final temperature of ~ 750°C which was maintained for 2 h. A constant flow of high purity helium (1000 sccm) was maintained in the chamber throughout the experiment. The optimal deposition temperature was found to be between 700 °C and 750°C. The size distribution, lattice structure, and crystal orientation of the as-synthesized products were characterized by scanning electron microscopy (SEM), x-ray diffraction (XRD), and transmission electron microscopy (TEM).

Fabrication of strain sensor

In order to completely separate the VO₂ nanowire and the SiO₂ from the SiO₂/Si substrate, it was etched

by BOE for 1 hour and rinsed with deionized water. The PDMS was prepared by mixing the liquid PDMS elastomer and a curing agent in the ratio 10:1 by weight. The liquid mixture was poured onto the VO₂ nanowire arrays grown on the Si substrates and thermally cured at 90°C for 30 min. After curing, the PDMS was peeled off the VO₂ nanowires array covered Si substrate, and Cr/Au (20/300 nm) electrodes were fabricated on the substrate across the VO₂ nanowires. A constant 1 V was applied to evaluate the performance of the strain sensor.

Molecular dynamical simulation

Molecular dynamical simulations were performed using the open source package, GROMACS v 4.5.4. Lennard-Jones (LJ) particles were assumed to interact via a LJ potential with a cutoff at 2.5σ and $\epsilon_{pp} = 2.0k_B T$. The surfaces were constructed by arranging LJ particles whose positions were fixed. The mobile LJ particles also interact with the surface particles via the LJ potential with a cutoff at 2.5σ but with $\epsilon_{ps} = 0.8k_B T$. (k_B is the Boltzmann constant, T is the absolute temperature, σ is an approximate diameter of LJ particles, which were set to 1, and $k_B T$ is set to 1.0 using the V-rescale method.)

Characterization

The morphologies of the VO₂ nanowire was investigated using a cold field emission scanning electron microscope (FE-SEM, S-4800, Hitachi) with an accelerating voltage of 10 kV. Elemental analysis was carried out in the SEM using energy-dispersive X-ray spectroscopy (EDX). The high-resolution TEM images were collected using a Cs-corrected JEM-2100F operated at 200 kV. For EELS experiments, a dedicated scanning transmission electron microscope JEM-2100F was used. The microscope was operated at 200 keV. It is equipped with an electron energy-loss spectrometer (Gatan, Enfina). The energy resolution in EELS, as measured by the full width at half maximum of the zero-loss peak, was 0.8 eV.

4.2.3 Result and discussion

Figure 12a shows scanning electron microscopy (SEM) images of randomly oriented VO₂ nanowires on a flat SiO₂/Si substrate. The nanowires have similar lengths and widths with narrow distributions as shown in Figure 13. Only nanowires are observed on the surface with no nanodroplets present, in contrast to the typical structures observed when this growth method is used. As mentioned above, nanowire growth is driven by Ostwald ripening, followed by the supercooling of the liquid nanodroplets. Normally, when this procedure is used many nanodroplets that are not consumed by the growth of the nanowires remain, in contrast to our observation (e.g., Figure 12a) of uniform nanowire growth with no unused nanodroplets remaining.

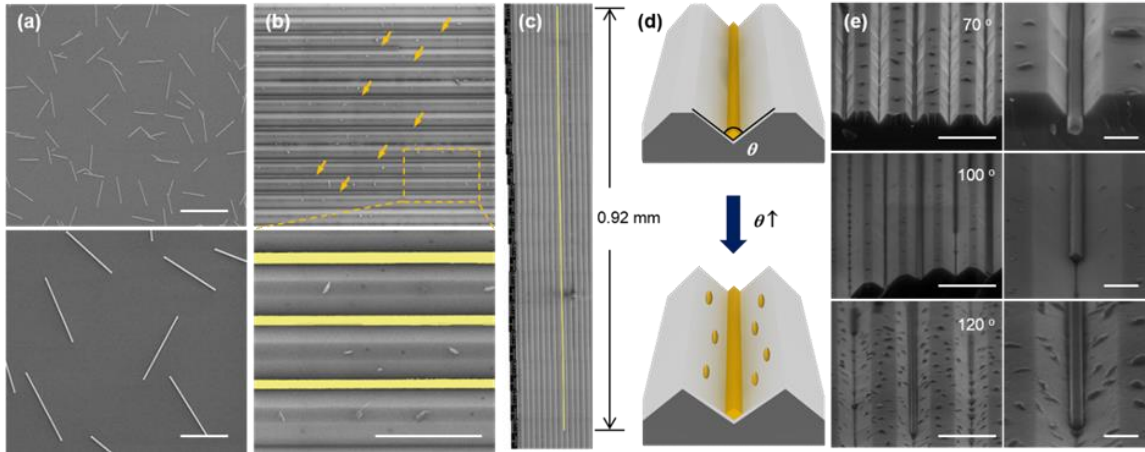


Figure 12. SEM image of VO₂ nanowires. (a, b) SEM images of randomly oriented VO₂ nanowires on a flat SiO₂/Si substrate and aligned along the direction of the V-groove, respectively. Scale bars in a are 20 μm (top) and 5 μm (bottom). Scale bar in b, 5 μm. (c) Millimeter-long horizontally aligned nanowire. (d) Schematic diagram of the VO₂ nanowire growth with the angle of V-groove. (e) SEM images with the angle of V-groove (70°, 100°, and 120°). Scale bars, 5 μm (left) and 1 μm (right).

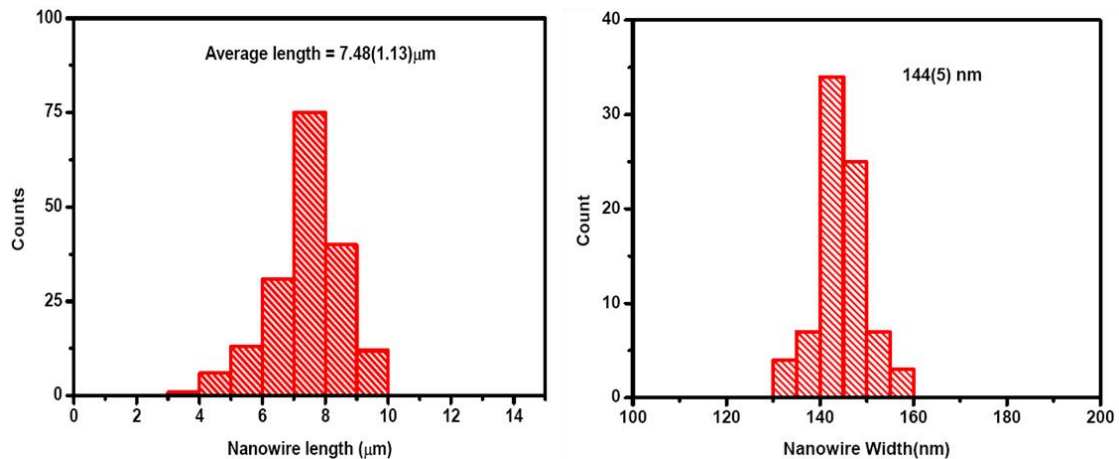


Figure 13. The histogram of length and width of randomly oriented VO₂ nanowires on a SiO₂/Si substrate.

When V₂O₅ was deposited on a V-grooved SiO₂/Si substrate by sputtering followed by annealing at 700°C in He atmosphere, it was observed that nanowire growth occurs only on the V-grooved surface with the nanowires aligned along the direction of the V-groove (Figure 12b). The lateral dimensions of the nanowires are in the range 20-690 nm, depending on the thickness of the deposited V₂O₅ film which varies from 20 to 200 nm, as shown in Figure 14. The nanowires were also observed to have different cross-sectional shapes depending on the shape of the grooved surface, as shown in Figure 15. Nanowires with a rhombus shape were formed in V-grooved surfaces with a flat groove bottom, while a rectangular shape was observed in the grooves with a V-shaped bottom. These results may be obtained because the

direction of the droplets transported along the V-grooved surface to the nanowires depends on the angle of the grooves and is different from that of the nanowires transported along a flat substrate.

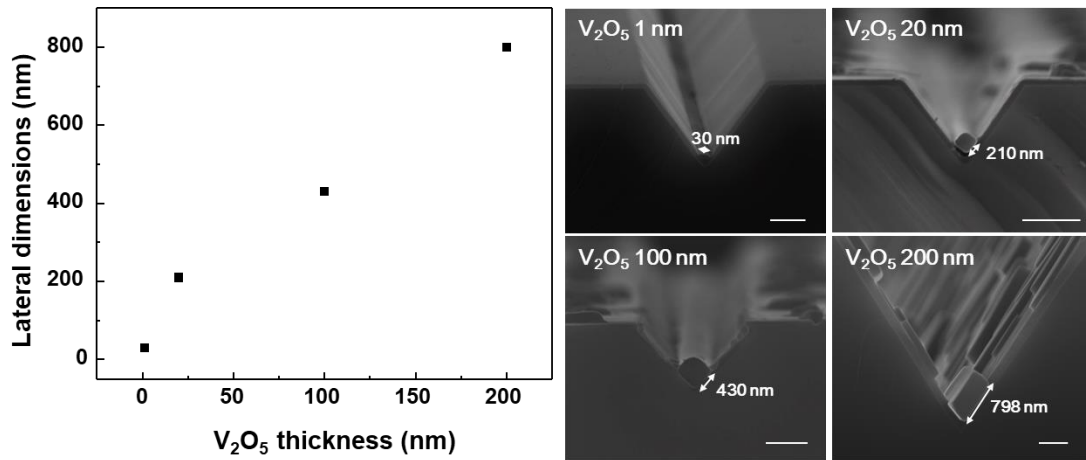


Figure 14. The VO₂ nanowire growth as a function of the V₂O₅ thin film thickness. Scale bars, 500 nm.

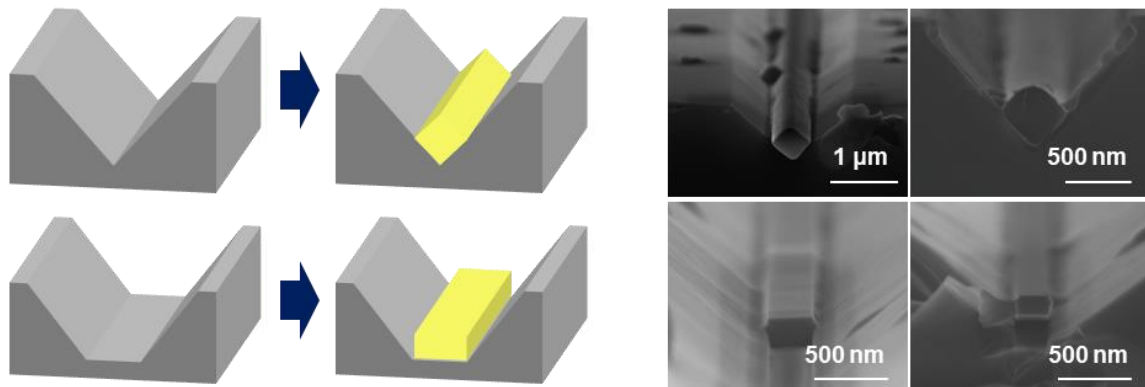


Figure 15. The cross-sectional images of the grown VO₂ with the shape of the V-grooved surface.

Interestingly, we observed that a few millimeter-long nanowires could be grown on the V-grooved surface as shown in Figure 12c. The synthesis of the nanowires longer than millimeter scale with ultrahigh aspect ratio ($> 10,000$) is essential for the fabrication of the commercial products using conventional semiconductor processes. To date, most efforts for producing such nanowires relied on nanolithography such as e-beam lithography and nanoimprint lithography due to the short length and random distribution of the wires. Although some studies attempting the synthesis of such long nanowires by various techniques such as chemical vapor deposition, wet-chemical method, and slip-coating method have been performed, these approaches are limited to a few types of materials and it is not easy to obtain a high degree of crystallinity²⁸⁻³⁰. The approach suggested here is more generally applicable to other metal-oxide nanowires²⁰. “However, it was not easy to synthesize the millimeter-long VO₂ nanowires with high yield. It was found that various parameters such as temperature, He flow

rate, V_2O_5 thin film thickness, and substrate surface morphology should be optimized to increase the yield. For example, very short nanowires were produced at high temperatures ($> 800^\circ\text{C}$) and low He flow rates due to the increase in the amount of residual oxygen atoms present in the quartz tube. Optimization of the parameters increased the yield of long nanowires.” The electrical property of the single nanowire was also evaluated by the current-voltage measurements of the millimeter-long VO_2 nanowire outfitted with Ti/Au (10/200 nm) electrodes by optical lithography and e-beam metal vapor deposition in a two-terminal configuration at room temperature in series with a $10\text{ k}\Omega$ resistor. It is well-known that as the applied voltage increases, the current slowly increases at low voltage values and then rapidly increases when a certain voltage is reached, at which point the Mott transition occurs. Presumably, at this voltage the resistive heating is sufficient to cause the temperature to reach the Mott transition temperature over a significant portion of the nanowire. Figure 16 shows that the voltages measured from a single nanowire were approximately 3 V and the resistance changes with the voltage were very similar. This means that the electrical properties are fully uniform inside the very long nanowire.

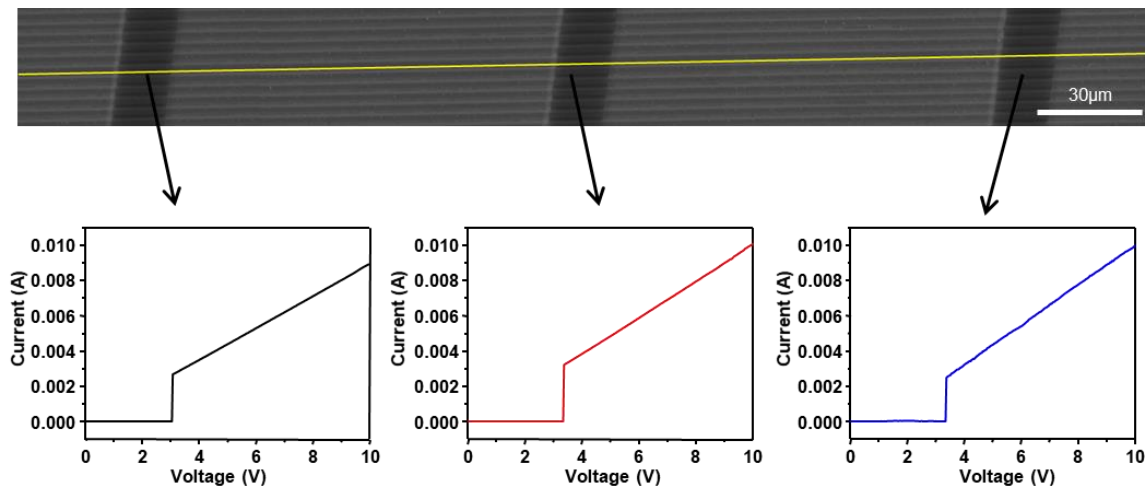


Figure 16. The millimeter-long VO_2 nanowires SEM image and I-V measurement graph.

The droplets observed on the flat surface between the V-grooves (Figure 12b) suggest that the V_2O_5 deposited on the top surface is not fully consumed to form the nanowires. To find the origin of the source material for the nanowire growth, the angle of the V-groove was varied from 70° to 120° using conventional photolithography and dry/wet etching processes, as shown in Figures 12d and 17, where the nanowires were grown under the same growth conditions. Regardless of the groove angles, many droplets were observed on the flat top surface between the grooves in Figure 12e. For a groove angle of 120° , the droplets were observed on the entire surface. As the angle decreases to 100° , the amount of the droplets on the sides of the V-groove surface decreased significantly and no droplets were observed

on the sides for a groove angle of 70° , suggesting that the droplets on the sides were consumed to form the nanowires.

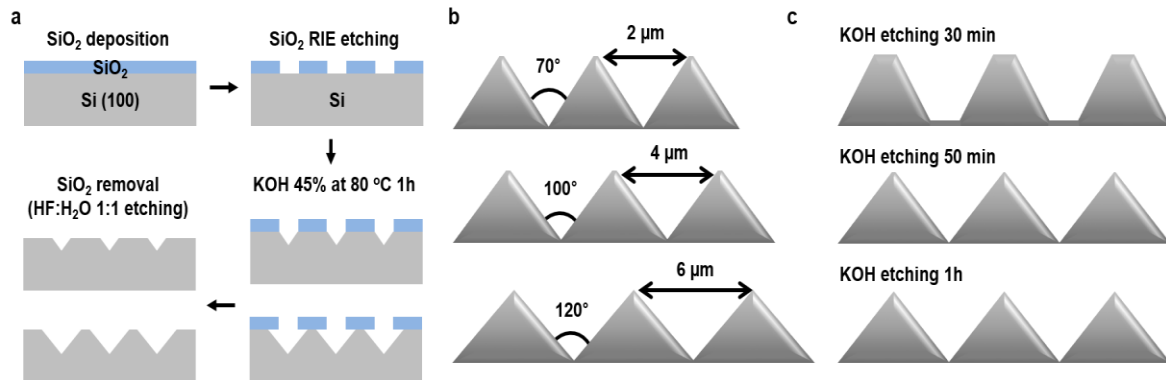


Figure 17. (a) Schematic fabrication process of V-groove templates and schematic diagrams of the V-groove templates with different pitch size (b) and KOH etching time (c).

The conversion of the droplets to nanowires was systematically investigated by investigating the V₂O₅-covered surface as a function of temperature and growth time, as shown in Figure 18. When the V₂O₅ was deposited on the V-grooved substrate, the flat surface became covered uniformly with a 30 nm thick oxide film. When subsequently heated to 500°C and immediately cooled, the film on the sides of the V-grooved surface broke up into nanodroplets which were present at or near the bottom region of the groove. By contrast, the droplets were randomly distributed on the flat surface. As the heating temperature increased to 600°C, the number of the nanodroplets on the groove surfaces decreased significantly, and a nanowire with a morphology that appeared to be quite rough was observed at the bottom of the groove. On a flat surface, the nanodroplets became quite larger. A further increase in the temperature to 700°C appeared to significantly increase the roughness of the nanowire. However, after cooling for 5 min, the nanowire surfaces appeared to become more smooth and the droplets decreased in size. This suggests that the droplets on the entire surface are transported to the V-grooved surface and are consumed in the nanowire growth process, indicating that the Ostwald ripening process occurred preferentially in the observed direction.

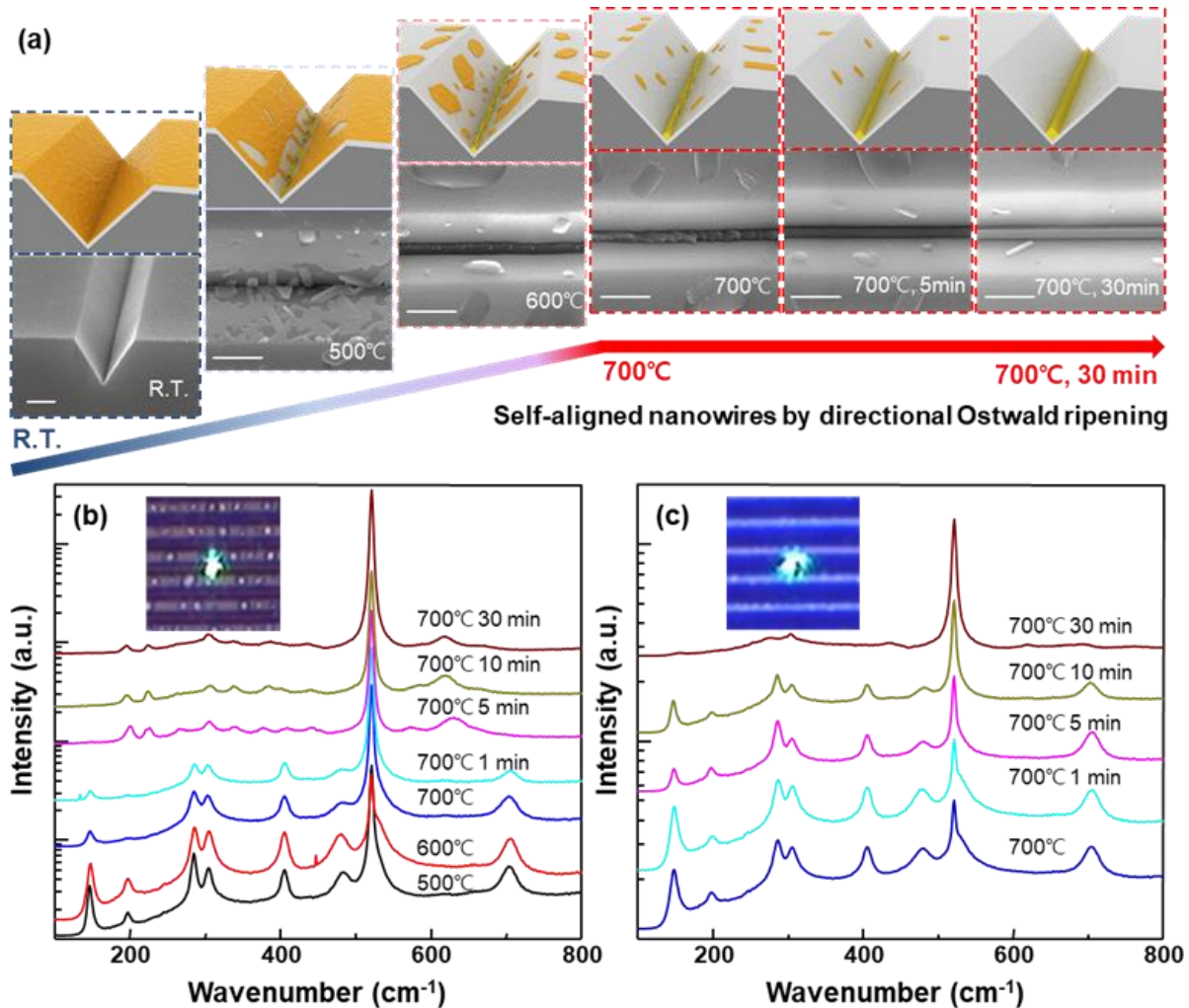


Figure 18. Morphological and structural evolution. (a) Ex-situ SEM images of morphological evolution of the vanadium oxide as a function of temperature and growth time. Scale bar: 1 μm . (b, c) Raman spectra obtained with the laser incident on the V-grooved surface and the flat surface between the V-grooves, respectively.

The microstructural changes with temperature and growth time were also investigated by Raman spectroscopy. Figure 18b shows the Raman spectra obtained with the laser incident on the V-grooved surface. For the samples annealed at the temperature lower than 700°C, the Raman spectra consistently show features at 148, 198, 280, 300, and 700 cm^{-1} that are characteristic of both crystalline and amorphous V_2O_5 . Upon annealing to 700°C, the intensities of the peaks decrease but do not disappear, meaning that the material in the V-grooved surface is still V_2O_5 even though it is collected from the disordered materials produced at such a high temperature. Upon increasing the time of the annealing at 700°C to 5 min, the nanowires were converted to VO_2 , and no further significant change in the Raman spectra was observed for a further increase in time. However, the droplets on the flat surface between the V-grooves are still V_2O_5 even after annealing at 700°C for 30 min. As mentioned above, this can be

explained either in terms of Ostwald ripening or coalescence followed by the supercooling of the liquid nanodroplets. Nanometer-size V_2O_5 droplets form with a freezing point that is strongly suppressed below that of the bulk due to their small size and interactions with the substrate that prevent the droplet from fully wetting the surface. The V_2O_5 nanodroplets then grow through Ostwald ripening or coalescence. Continued growth of the droplet leads to supercooled V_2O_5 that can then crystallize by the subsequent loss of O_2 in the reducing environment of the furnace, forming VO_2 crystallites and nanowires.

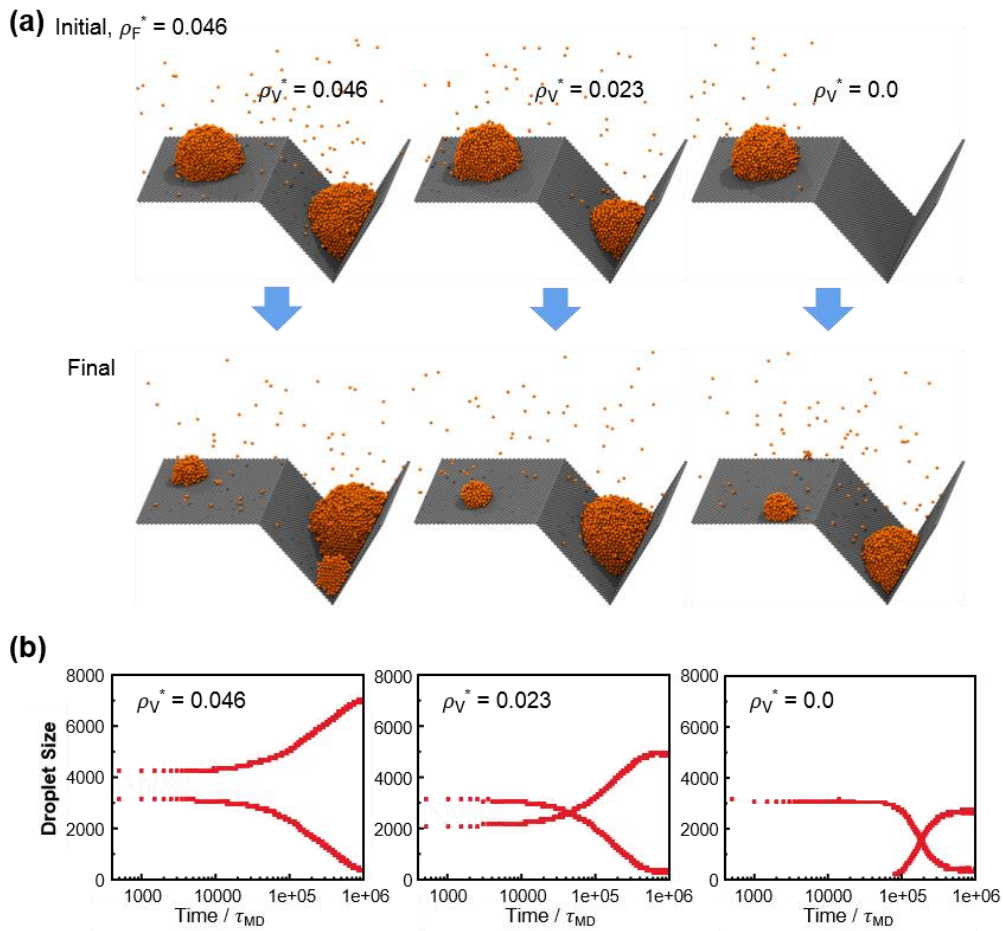


Figure 19. MD simulation results for directional Ostwald ripening. (a) MD simulation of a simple spherical particles interacting with Lennard-Jones (LJ) potential on a surface with a half flat and the other half V-shaped. (b) time-evolution of droplets size.

Molecular dynamics (MD) simulations were also carried out for spherical particles interacting with the Lennard-Jones (LJ) potential on a surface for which one half is flat, while the other half is V-shaped, in order to better understand the influence of the surface inclination on the Ostwald ripening of V_2O_5 droplets. The initial distributions of the LJ droplets on surfaces with flat and V-shaped geometries

(Figure 19a) are constructed in two steps: the droplets are formed separately in the systems only with the flat surface at the LJ particle reduced number density of ρ_F^* and only with the V-shaped groove at the LJ particle reduced number density of ρ_V^* , and they are combined to have one droplet each on the flat surface and on the V-shaped groove. LJ particles interact with each other via the LJ potential with an attraction strength of $\epsilon_{pp} = 2.0k_B T$ and with the surface particles via the same LJ potential but with $\epsilon_{ps} = 0.8k_B T$, where k_B is the Boltzmann constant, T is the absolute temperature, and $k_B T$ is equal to 1.0. The density of the LJ particles on the flat surface was chosen as $\rho_F^* = 0.046$, while that on the V-shaped groove was varied as follows $\rho_V^* = 0.046, 0.023, \text{ and } 0.0$. The attraction parameters were chosen such that the LJ particles form stable droplets and the droplets are adsorbed onto the surface and diffuse on the surface. Several values of the attraction parameter were tested and it was verified that the obtained results do not change qualitatively when the value of the attraction parameter was varied in the range investigated in this work. Various values of the LJ density on the V-shaped groove were investigated to verify that the varying size of the initial droplet on the V-shaped groove does not significantly influence the directional Ostwald ripening mechanism.

For a simulation duration of $10^6 \tau_{MD}$ (the unit time for the MD simulations), it was found that the droplet on the flat surface moves and its size decreases. On the other hand, the droplet size on the V-shaped groove increases in size with time, as shown in Figure 19a. The droplet size changes were quantified by cluster analysis. To identify a cluster of LJ particles, we measured the distances of a given LJ particle with respect to all of the other LJ particles and counted the number of neighboring LJ particles within a critical distance equal to 1.5σ (where σ is approximately the average diameter of the LJ particles). If the LJ particle has five or more neighbors within this distance, it is defined as a member of a cluster. The results of the cluster analysis are presented in Figure 19b. The droplet size defined as the number of LJ particles in the droplet (or cluster) is shown as a function of the simulation time. At the beginning, each figure in Figure 19b has two symbols representing the sizes of two droplets on the flat surface and the V-shaped groove; these sizes are 3150 and 4250 in the first case with $\rho_V^* = 0.046$, and 3150 and 2050 in the second case with $\rho_V^* = 0.023$. In the third case with $\rho_V^* = 0.00$, only one symbol at 3150 is shown, representing the droplet size on the flat surface. With increasing time, the droplets on the flat surface shrink continuously whereas those on the V-shaped groove grow continuously. The continuous change in the droplet size is consistent with Ostwald ripening that occurs through the constituent atoms and/or molecules of smaller particles leaving these particles to diffuse and ultimately join the larger particles. If the droplet growth mechanism instead involved the diffusion of entire droplets and their subsequent coalescence, the droplet sizes would change discontinuously due to the abrupt increase in the droplet size by the coalescence of the droplets. The simulation trajectories showed that the droplets did not diffuse from the flat surface onto the V-shaped groove or vice versa. Only a mechanism in which an increase/decrease in droplet size occurs by molecular transfer from one

droplet to another is consistent with the results of our simulations.

It was also known that at a high temperature such as 700°C, the nanodroplets are liquid due to the low melting point ($\sim 690^\circ\text{C}$) of the bulky V_2O_5 and the melting-point depression of nanosized particles. Once the droplets are filled on a concave surface such as V-groove, the liquid droplets will show a concave surface because at a high temperature, such as 700°C, the surface is quite hydrophilic (Figure 20), which shows the tails located on both ends of the nanowire. The angle-dependent study also indicates that as the angle decreases, the concavity of the liquid on the concave surface increases, so that the surface energy increases. This will also increase the surface energy of a concave surface, increasing the flux of the materials.

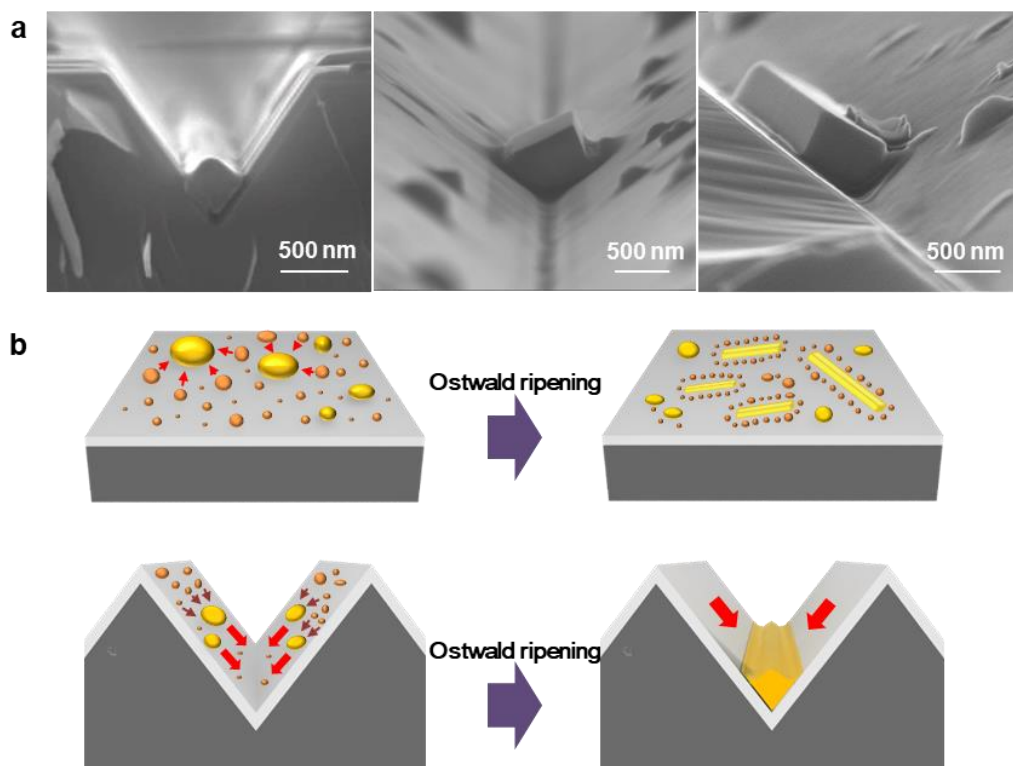


Figure 20. (a) The SEM image of VO_2 nanowire tail located on V groove substrate and (b) the schematic image of Ostwald ripening process on flat substrate and V groove substrate.

The microstructural analysis of a single VO_2 nanowire in the V-grooved surface was performed by high-resolution transmission electron microscopy (HR-TEM). Figure 21a show the cross-sectional images of the nanowire present in the V-groove with a sharp bottom with the angle of $\sim 70^\circ$. It is clearly observed that the cross-section of the nanowire is rhombus- or diamond-shaped with very sharp edges except for one edge. The shape of the nanowire appears to be determined by the shape of the V-groove, as shown in Figure 15. The angle ($\sim 70^\circ$) of the edges is larger than the angle of the V-groove which will induce the incursion of the nanowires into the SiO_2 region with the thickness of 100 nm. Figure 21b

shows the HR-TEM image of the region 'b' and Fourier transformation (FFT) image along the $\langle 001 \rangle$ zone axis in the monoclinic VO_2 phase. It shows clear lattice fringes in the entire region and the marked lattice spacing of 0.467 nm corresponds to the interplane spacing of the (010) and (001) planes of monoclinic VO_2 crystals. This confirms the high crystallinity of the nanowire grown in a V-grooved surface.

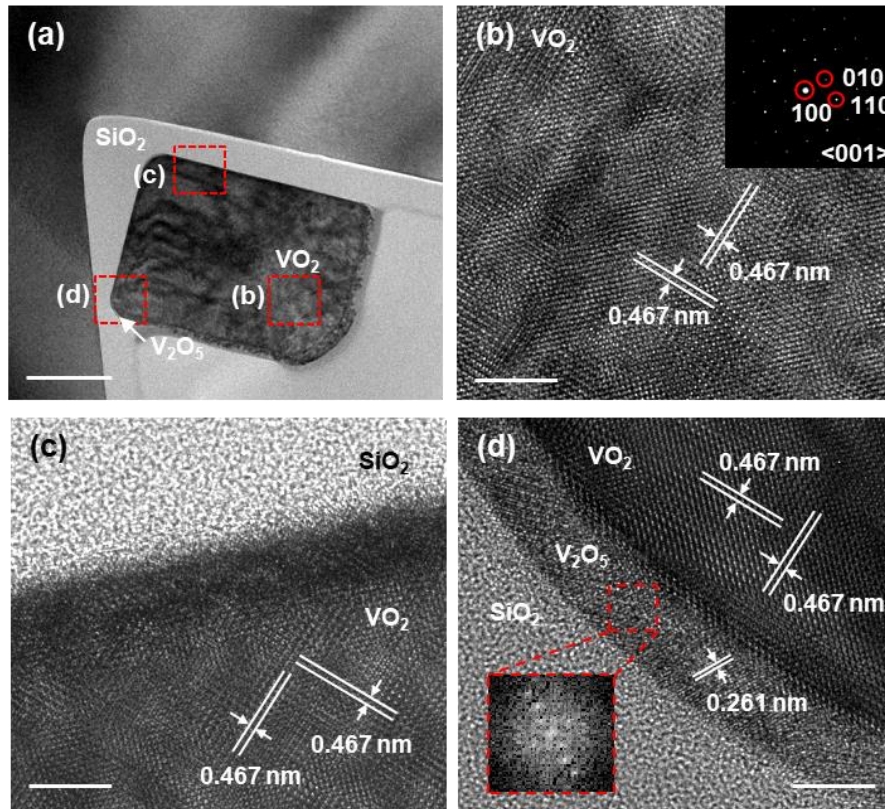


Figure 21. Cross-sectional TEM images of VO_2 nanowire grown in V-grooved surface. (a) Cross-sectional low-resolution transmission electron microscope (TEM) image of single VO_2 nanowire grown in V-grooved surface. Scale bar, 0.2 μm . (b) high-resolution TEM image of the VO_2 nanowire. Scale bar, 5 nm. (c, d) high-resolution TEM images of the VO_2 nanowire at the interface region near the SiO_2/Si substrate. Scale bar, 5 nm. The corresponding fast Fourier transform (FFT) in b and d are shown.

An interesting feature in the TEM images can be observed by comparing the images of Figure 21c and 4d obtained from the regions 'c' and 'd', respectively. In Figure 21c, a high-magnification view of the region near the interface clearly shows high crystallinity of VO_2 nanowire. Indeed, only very few atomic layers (< 3 nm) are observed which may be due to various imaging conditions, and particularly the focus of the objective lens. In Figure 21d, it appears that the crystallinity is also good and there is no significant difference in the lattice spacing, implying that no impurity atoms were incorporated during the growth. However, a clear interfacial layer with a thickness of approximately 5 nm was observed in

Figure 21d. Because the interface is too thin to be analyzed, the lattice image and the corresponding FFT image are not clear, however, the lattice distance and FFT result suggest the possibility of oxygen-rich vanadium oxide such as V_2O_5 . This was confirmed by the electron energy loss spectroscopy (EELS) obtained at the interface, as shown in Figure 22. In VO_2 , $V-L_{2,3}$ edges were due to the excitation from the ground state with the $2p^63d^n$ V configuration toward the $2p^53d^{n+1}$ V states³¹, which are separated by approximately 6.5 eV. Strong shoulders on the lower energy side of the L_3 and L_2 lines were also observed. The spectrum obtained at the interface between VO_2 and SiO_2 showed a chemical shift of the lines by 0.1 eV and an increase in the intensity of the O K edge, indicating that the oxidation state changed from V^{5+} to V^{4+} , so that the material formed at the interface was V_2O_5 . In fact, the oxygen atoms at the interface do not appear to be out-diffused even in the reducing environment.

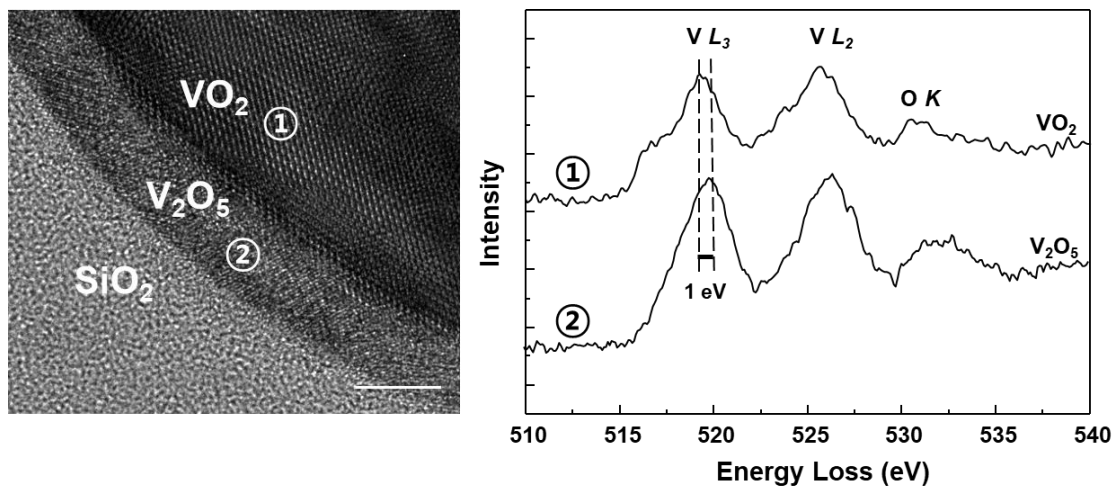


Figure 22. Electron energy loss spectroscopy (EELS) in V_2O_5 and VO_2 regions.

At the growth temperature of 750°C , V_2O_5 exists in the liquid form due to its low melting point ($\sim 690^\circ\text{C}$). At the interface, it can be suggested that the SiO_2 is dissolved into the liquid phase of V_2O_5 , forming a complex composed of vanadium, silicon, and oxygen. This shows that it also stays in liquid at grown temperature. When the mixture was cooled, it is believed that the liquid droplets were crystallized by the subsequent loss of oxygen in the reducing environment of the furnace obtained by introducing the He gas to the nanowires. According to phase diagram suggested in previous work³², the solubility limit of solid SiO_2 in solid V_2O_5 is extremely low and the two phases are completely immiscible at the temperatures lower than 661°C . Additionally, it is expected that the solubility of SiO_2 in solid VO_2 is much lower because the eutectic temperature ($\sim 1700^\circ\text{C}$) of the VO_2 - SiO_2 system is much higher than that (661°C) of the V_2O_5 - SiO_2 system³³. VO_2 - SiO_2 eutectic temperature can be predicted by the cation field strength. The relationship between the cation field strength of the metallic ions and the melting point of their oxide suggests Dietzel's approach to amorphous silicon formation.

This principle was applied to obtain a relation between the cation field strength of the metallic ions and their ability to react with SiO₂, based on the values of the lowest eutectic temperatures in the silica-oxide binary systems. Using the data of Albright and of Levin and Mc-Murdic et al., a good correlation was obtained between the lowest eutectic temperature in the various silica-oxides binary systems and the cation field strength calculated as Z/a^2 , where Z is the valence of the cation and a is the actual cation-oxygen distance in the oxide. The oxides with lower cation field strengths (Al₂O₃, ZrO₂, MgO, VO₂ and ThO₂) are very strong, stiff, and difficult to shear even at high temperatures, because their cations interact with each other and form strong bonds. This means that during crystallization to VO₂, the Si would be in-diffused to SiO₂/Si, and a VO₂ phase with high purity in reducing environment would be produced in which a very thin interfacial layer composed of oxygen-rich oxides would remain.

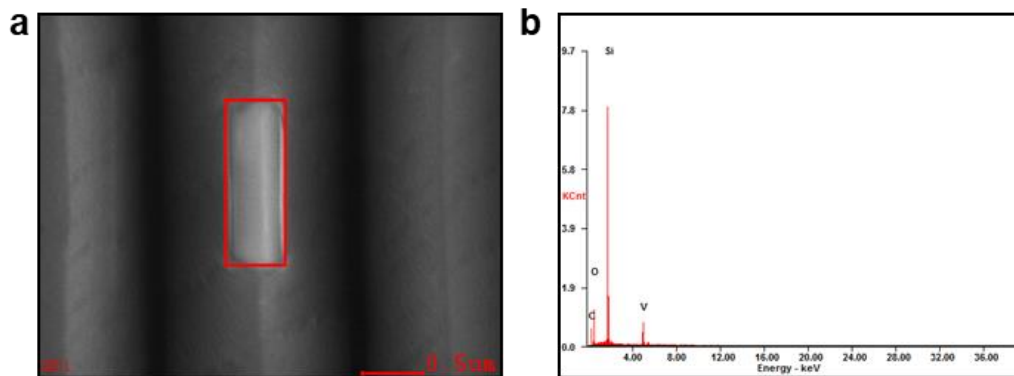


Figure 23. (a) SEM image and (b) EDXS result of the transferred VO₂ nanowire onto PDMS substrate.

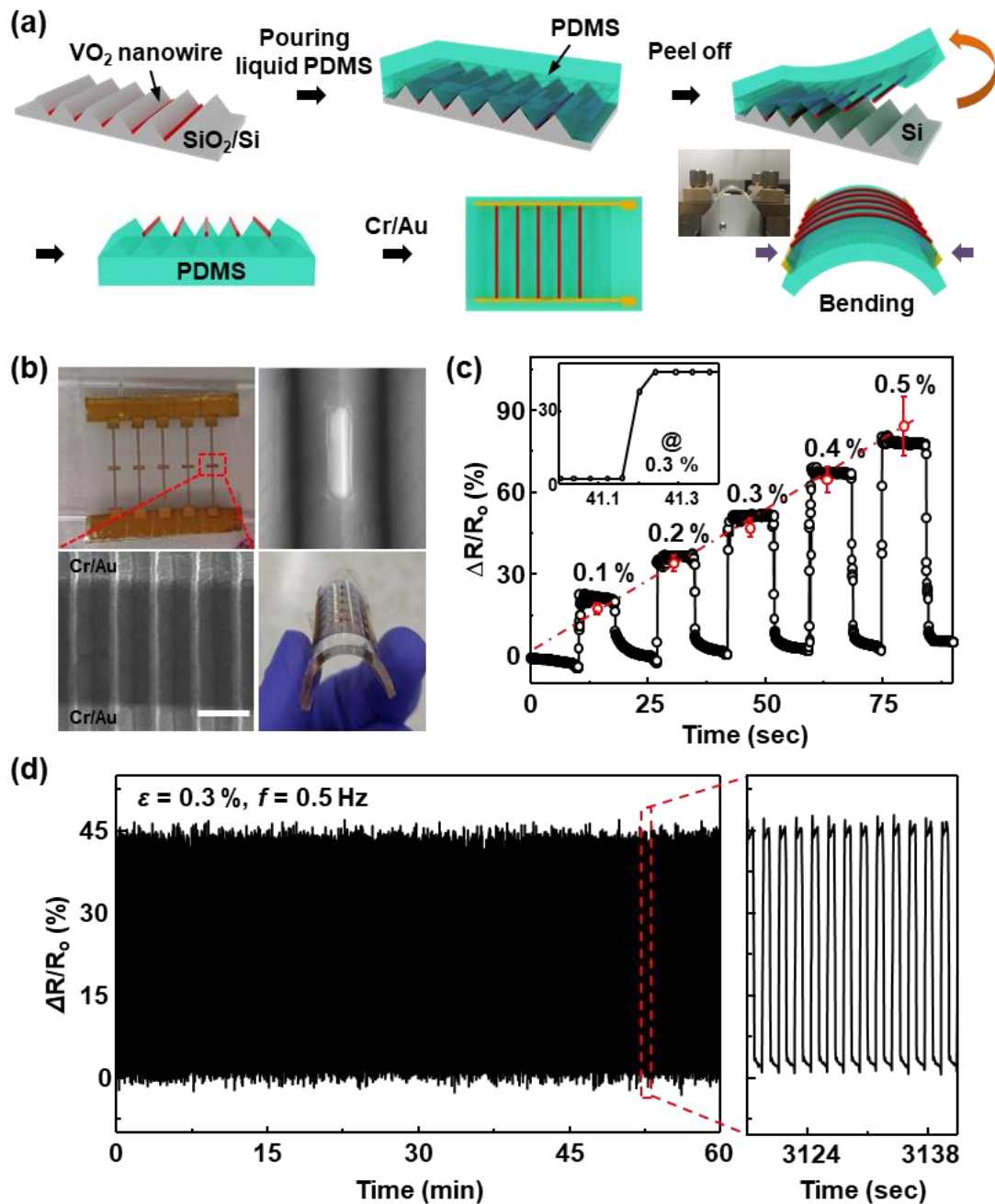


Figure 24. Highly sensitive strain sensor made with VO₂ nanowire arrays. (a) Schematic diagrams of the fabrication process for the strain sensor array with VO₂ nanowire transferred onto the PDMS substrate. (b) Photos of the strain sensor and the SEM images of the VO₂ nanowires transferred onto PDMS substrate. To measure the resistance of the device, Cr/Au electrode was deposited onto the nanowires. (c) Change in resistance ($\Delta R/R_0 = (R - R_0)/R_0$) with the bending motion and the magnitude of the strain. The inset shows the expanded view of the change in resistance at the strain of 0.3%. (d) Change in the resistance of VO₂ nanowire array with the strain of 0.3% during 1 hour as bending and release cycles.

Finally, a flexible VO₂ nanowire array was fabricated by pouring polydimethylsiloxane (PDMS) on the substrate followed by the peeling off of the PDMS layer from the substrate, as shown in Figure 24a. Prior to the peel-off process, the SiO₂ layer underneath the nanowires was chemically etched by buffered oxide etchant (BOE). Figure 24b shows a photograph of the strain sensor made using aligned VO₂ nanowire array transferred to the PDMS substrate and the SEM images of the nanowire. It is clear that the nanowire was positioned on the top surface of the V-shaped region, as is also supported by the Energy-dispersive X-ray spectroscopy (EDX) results shown in Figure 23. On the nanowires, Cr/Au (30/50 nm) metals were deposited in a perpendicular electrode configuration. The sensor can be bent and released smoothly on the joint of an index finger, indicating that it is quite flexible. Using the bending motion, the change in the resistance of the nanowires ($\Delta R/R_o = (R - R_o)/R_o$) was measured with the strain magnitude varying from 0.1% to 0.5% and is plotted in Figure 24c. As the sensor was bent, the resistance of the nanowires increased with a very fast response time of several tens of milliseconds (~88 ms), as shown in the inset, indicating that the change in the electrical property was mainly due to the phase transition between the M₁ and M₂ phases³⁴. After the force was released, the resistance returned to 90% of its original value with a very fast recovery time of several hundreds of milliseconds (~781 ms). “The recovery time is relatively long compared to the response time, which may be due the residual strain present in the PDMS substrate even after the external bending force was released^{35,36}.” As the magnitude of the strain increased, the change in the resistance significantly and almost linearly increased and reached 100% at the strain of 0.5%. The strain sensitivity ($S = 1.02$ at 0.5%) was also high in comparison with other resistive pressure sensors³⁷⁻³⁹. The gauge factor (GF), defined as the ratio of the normalized change in the electrical resistance ($\Delta R/R_0$) to the mechanical strain ε was calculated to be approximately 215, comparable to the results reported to date⁴⁰⁻⁴⁷. Interestingly, no multiple steps were observed in the change in the resistance when the sensor was bent, indicating that the nanowires were electrically uniform and mechanically flexible. As plotted in Figure 24d, no significant change was observed in the change in the resistance for 1 h, indicating the good long-term stability of the sensor. This work is the first demonstration of the strain sensor composed of the VO₂ nanowires array on the flexible substrate⁴⁸⁻⁵⁰.

4.2.4 Conclusion

In summary, we describe a simple approach for growing millimeter-long and linearly, self-aligned VO₂ nanowires based on directional Ostwald Ripening. This process was inspired by the idea that a thin V₂O₅ film deposited on a silicon oxide substrate can completely dewet into a large assembly of very small and uniform droplets, resulting in the successful growth of uniform small-diameter (± 5 nm) VO₂ nanowires with narrow length distributions size (± 1.13 nm) on silicon oxides substrate via the complete wetting. This work was expanded by designing the substrate composed of V-grooved surface deposited

by silicon oxides in which the transport of liquid particles is controlled by the chemical potential energy and surface morphology, causing the particle coarsening process to become directional. The process was successfully explained by molecular dynamics simulations of spherical particles on two surface morphologies interacting via the Lennard-Jones potential. The coupled effects of the interactions of the particles on the two surfaces side-by-side resulted in the nanowires' preferentially self-aligning in the V-grooved surface, resulting in the successful growth of millimeter-long nanowires with very uniform metal-insulator transition properties and self-alignment. By utilizing millimeter-long horizontally aligned VO₂ nanowires, we also fabricated strain sensor arrays with high sensitivity ($S = 1.02$ at 0.5%) and very fast response time of several tens of milliseconds through the chemical transfer onto a PDMS substrate.

4.2.5 Reference

- [1] Javey, A. The 2008 Kavli Prize in Nanoscience: Carbon Nanotubes. *ACS Nano* **2008**, 2, 1329–1335.
- [2] Hang, Q.; Wang, F.; Carpenter, P. D.; Zemlyanov, D.; Zakharov, D.; Stach, E. A.; Buhro, W. E.; Janes, D. B. Role of Molecular Surface Passivation in Electrical Transport Properties of InAs Nanowires. *Nano Lett.* **2008**, 8, 49–55.
- [3] Lee, J.; Lee, P.; Lee, H.; Lee, D.; Lee, S. S.; Ko, S. H. et al. Very long Ag nanowire synthesis and its application in a highly transparent, conductive and flexible metal electrode touch panel. *Nanoscale*. **2012**, 4, 6408-6414.
- [4] Lee, J.; Lee, P.; Lee, H. B.; Hong, S.; Lee, I.; Yeo, J.; Lee, S. S.; Kim, T. -S.; Lee, D.; Ko, S. H. Room-Temperature Nanosoldering of a Very Long Metal Nanowire Network by Conducting-Polymer-Assisted Joining for a Flexible Touch-Panel Application. *Adv. Funct. Mater.* **2013**, 23, 4171–4176.
- [5] Wallentin, J. et al. InP Nanowire Array Solar Cells Achieving 13.8% Efficiency by Exceeding the Ray Optics Limit. *Science*, **2013**, 339, 1057-1060.
- [6] Liu, C.; Dasgupta, N. P.; Yang, P. Semiconductor nanowires for artificial photosynthesis. *Chem. Mater.* **2013**, 26, 415.
- [7] Yu, Z.; Zhang, Q.; Li, L.; Chen, Q.; Niu, X.; Liu, J.; Pei, Q. Highly flexible silver nanowire electrodes for shape-memory polymer light-emitting diodes. *Adv. Mater.* **2011**, 23, 664–668.
- [8] Wu, J.; Agrawal, M.; Becerril, H. A.; Bao, Z.; Liu, Z.; Chen, Y.; Peumans, P. Organic Light-Emitting Diodes on Solution-Processed Graphene Transparent Electrodes. *ACS Nano*. **2010**, 4, 43–48.
- [9] Kolmakov, A.; Zhang, Y.; Cheng, G.; Moskovits, M. Detection of CO and O₂ using tin oxide nanowire sensors. *Adv. Mater.* **2003**, 15, 997.
- [10] Kumar, B.; Atla, V.; Brian, J. P.; Kumari, S.; Nguyen, T. Q.; Sunkara, M.; Spurgeon, J. M. Reduced SnO₂ Porous Nanowires with a High Density of Grain Boundaries as Catalysts for Efficient Electrochemical CO₂-into-HCOOH Conversion. *Angew.Chem. Int.Ed.* **2017**, 56, 3645 –3649.
- [11] Moos, R. A brief overview on automotive exhaust gas sensors based on electroceramics. *Int. J. Appl. Ceram. Technol.* **2005**, 2, 401–413.
- [12] Zhang, R.; Pang, W.; Feng, Z.; Chen, X.; Chen, Y.; Zhang, Q.; Zhang, H.; Sun, C.; Yang, J.; Zhang, D. Enabling selectivity and fast recovery of ZnO nanowire gas sensors through resistive switching. *Sens Actuators B Chem.* **2017**, 238, 357-363.
- [13] Shao, M. W.; Shan, Y. Y.; Wong, N. B.; Lee, S. T. Silicon nanowire sensors for bioanalytical applications: glucose and hydrogen peroxide detection. *Adv. Funct. Mater.* **2005**, 15, 1478.

- [14] Hsu, C. -L.; Lin, J. -H.; Hsu, D. -X.; Wang, S. -H.; Lin, S. -Y.; Hsueh, T. -J. Enhanced non-enzymatic glucose biosensor of ZnO nanowires via decorated Pt nanoparticles and illuminated with UV/green light emitting diodes. *Sens Actuators B Chem.* **2017**, *238*, 150-159.
- [15] Park, J. H.; Kim, K. H.; Park, Y. W.; Lagerwall, J. P. F.; Scalia, G. Ultralong Ordered Nanowires from the Concerted Self-Assembly of Discotic Liquid Crystal and Solvent Molecules. *Langmuir.* **2015**, *31*, 9432–9440.
- [16] Li, Y.; Meng, G. W.; Zhang, L. D. Ordered semiconductor ZnO nanowire arrays and their photoluminescence properties. *Appl. Phys. Lett.* **2000**, *76*, 2011.
- [17] Li, S. Y.; Lee, C. Y.; Tseng, T. Y. Copper-catalyzed ZnO nanowires on silicon (100) grown by vapor–liquid–solid process. *J Cryst Growth.* **2003**, *247*, 357-362.
- [18] Zhang, Y.; Ouyang, B.; Xu, J.; Jia, G.; Chen, S.; Rawat, R. S.; Fan, H. J. Rapid Synthesis of Cobalt Nitride Nanowires: Highly Efficient and Low-Cost Catalysts for Oxygen Evolution. *Angew. Chem. Int. Ed.* **2016**, *55*, 8670 –8674.
- [19] Xu, L.; Li, X.; Zhan, Z.; Wang, L.; Feng, S.; Chai, X.; Shen, W. L. J.; Weng, Z.; Sun, J. Catalyst-Free, Selective Growth of ZnO Nanowires on SiO₂ by Chemical Vapor Deposition for Transfer-Free Fabrication of UV Photodetectors. *ACS Appl. Mater. Interfaces.* **2015**, *7*, 20264–20271.
- [20] Kim, M. H.; Lee, B.; Lee, S.; Larson, C.; Baik, J. M.; Yavuz, C. T.; Seifer, S.; Vajda, S.; Winans, R. E.; Moskovits, M.; Stucky G. D.; Wodtke. A. M. Growth of metal oxide nanowires from supercooled liquid nanodroplets. *Nano Lett.* **2009**, *9*, 4138–4146.
- [21] Jorritsma, J.; Gijs, M. A. M.; Kerkhof, J. M.; Stienen, J.G.H. General technique for fabricating large arrays of nanowires. *Nanotechnology.* **1996**, *7*, 263–265.
- [22] Li, X. V.; Cole, R. M.; Milhano, C. A.; Bartlett, P. N.; Soares, B. F.; Baumberg, J. J.; Groot, C. H. The fabrication of plasmonic Au nanovoid trench arrays by guided self-assembly. *Nanotechnology.* **2009**, *20*, 285309.
- [23] E. Kapon, D. M. Hwang, and R. Bhat, Stimulated Emission in Semiconductor Quantum Wire Heterostructures. *Phy. Rev. Lett.*, **1989**, *63*, 430.
- [24] M. Walther, E. Kapon, J. Christen, D.M. Hwang, and R. Bhat, Carrier capture and quantum confinement in GaAs/AlGaAs quantum wire lasers grown on V-grooved substrates. *Appl. Phys. Lett.* **1992**, *60*, 1992.
- [25] Gustafsson, A.; Reinhardt, F.; Biasiol, G.; Kapon, E. Low-pressure organometallic chemical vapor deposition of quantum wires on V-grooved substrates. *Appl. Phys. Lett.* **1995**, *67*, 3673.
- [26] Biasiol, G.; Reinhardt, F.; Gustafsson, A.; Martinet, E.; Kapon, E. Structure and formation mechanisms of AlGaAs V-groove vertical quantum wells grown by low pressure organometallic chemical vapor deposition. *Appl. Phys. Lett.* **1996**, *69*, 2710.

- [27] Martinet, E.; Reinhardt, F.; Gustafsson, A.; Biasiol, G.; Kapon, E. Self-ordering and confinement in strained InGaAs/AlGaAs V-groove quantum wires grown by low-pressure organometallic chemical vapor deposition. *Appl. Phys. Lett.* **1998**, *72*, 701.
- [28] Tsvion. D.; Schwartzman, M.; Ronit P.-B.; Huth, P.; Joselevich E. Guided Growth of Millimeter-Long Horizontal Nanowires with Controlled Orientations. *Science*. **2011**, *333*, 1003-1007.
- [29] Lee, J. H.; Lee, P.; Lee, D.; Lee, S. S.; Ko, S. H. Large-Scale Synthesis and Characterization of Very Long Silver Nanowires via Successive Multistep Growth. *Cryst. Growth Des.* **2012**, *12*, 5598–5605.
- [30] Spinal, M.; Bonvin, E.; Sienkiewicz¹, A.; Náfrádi, B.; Forró, L.; Horváth E. Controlled growth of CH₃NH₃PbI₃ nanowires in arrays of open nanofluidic channels. *Sci. Rep.* **2016**, *6*. 19834.
- [31] Laffont, L.; Wu, M. Y.; Chevallier, F.; Poizot, P.; Morcrette, M.; Tarascon, J. M. High resolution EELS of Cu–V oxides: Application to batteries materials. *Micron*, **2006**, *37*, 459–464.
- [32] AdabiFiroozjaei, E.; Koshy, P.; Sorrell, C. C. Effects of V₂O₅ addition on the corrosion resistance of andalusite-based low-cement castables with molten Al-alloy. *J. Eur. Ceram. Soc.* **2012**, *32*, 1463–1471.
- [33] Armstrong, W. M.; Chaklader, A. C. D.; De Cleene, M. L. A. Interface Reactions Between Metals and Ceramics: Refractory Metals–Fused SiO₂ System. *J Am Ceram Soc.* **1962**, *9*, 407-412.
- [34] Hu, B.; Ding, Y.; Chen, W.; Kulkarni, D.; Shen, Y.; Tsukruk, V. V.; Wang, Z. L. External-Strain Induced Insulating Phase Transition in VO₂ Nanobeam and Its Application as Flexible Strain Sensor. *Adv. Mater.* **2010**, *22*, 5134–5139.
- [35] Drozdov, A. D.; Clyens, S.; Theilgaard, N. Multi-cycle deformation of silicone elastomer: observations and constitutive modeling with finite strains. *Meccanica*. 2013, *48*, 2061.
- [36] Dorfmann, A.; Ogden, R.W. A constitutive model for the Mullins effect with permanent set in particle-reinforced rubber. *Int. J. Solids Struct.* 2004, *41*, 1855.
- [37] Cheng, Y.; Wang, R.; Sun, J.; Gao, LA. Stretchable and Highly Sensitive Graphene-Based Fiber for Sensing Tensile Strain, Bending, and Torsion. *Adv. Mater.* **2015**, *27*, 7365–7371.
- [38] Qin, Y.; Peng, Q.; Ding, Y.; Lin, Z.; Wang, C.; Li, Y.; Xu, F.; Li, J.; Yuan, Y.; He, X.; Li, Y. Lightweight, Superelastic, and Mechanically Flexible Graphene/Polyimide Nanocomposite Foam for Strain Sensor Application. *ACS Nano*. **2015**, *9*, 8933-8941.
- [39] Amjadi, M.; Pichitpajongkit, A.; Lee, S.; Ryu, S.; Park, I. Highly Stretchable and Sensitive Strain Sensor Based on Silver Nanowire–Elastomer Nanocomposite. *ACS Nano*. **2014**, *8*, 5154–5163.
- [40] Liao, X.; Liao, Q.; Zhang, Z.; Yan, X.; Liang, Q.; Wang, Q.; Li, M.; Zhang, Y. A Highly Stretchable ZnO@Fiber-Based Multifunctional Nanosensor for Strain/Temperature/UV Detection. *Adv. Funct. Mater.* **2016**, *26*, 3074–3081.

- [41] Xiao, Xu.; Yuan, L.; Zhong, J.; Ding, T.; Liu, Y.; Cai, Z.; Rong, Y.; Han, H.; Zhou, J.; Wang, Z. L. High-Strain Sensors Based on ZnO Nanowire/Polystyrene Hybridized Flexible Films. *Adv. Mater.* **2011**, *23*, 5440–5444.
- [42] Cheng, Y.; Wang, R.; Zhai, H.; Sun, J. Stretchable electronic skin based on silver nanowire composite fiber electrodes for sensing pressure, proximity, and multidirectional strain. *Nanoscale.* **2017**, *9*, 3834-3842.
- [43] Amjadi, M.; Pichitpajongkit, A.; Lee, S.; Ryu, S.; Park, I. Highly Stretchable and Sensitive Strain Sensor Based on Silver Nanowire-Elastomer Nanocomposite. *ACS Nano.* **2014**, *8*, 5154–5163.
- [44] Yu, X. -G.; Li, Y. -Q.; Zhu, W. -B.; Huang, P.; Wang, T. -T.; Hu, N.; Fu, S. -Y. A wearable strain sensor based on a carbonized nano-sponge/silicone composite for human motion detection. *Nanoscale.* **2017**, *9*, 6680.
- [45] Cheng, Y.; Wang, R.; Sun, J.; Gao, L. A Stretchable and Highly Sensitive Graphene-Based Fiber for Sensing Tensile Strain, Bending, and Torsion. *Adv. Mater.* **2015**, *27*, 7365–7371.
- [46] Inomata N.; Toan, N. V.; Toda, M.; Ono, T. Evaluation of Piezoresistive Property of Vanadium Oxide Thin Film Deposited by Sputtering. *IEEE Sens. Lett.* **2018**, *2*, 2500204.
- [47] Liao, F.; Zhu, Z.; Yan, Z.; Yao, G.; Huang, Z.; Gao, M.; Pan, T.; Zhang, Y.; Li, Q.; Feng, X.; Lin, Y. Ultrafast response flexible breath sensor based on vanadium dioxide. *J. Breath Res.* **2017**, *11*, 036002.
- [48] Kim, M.-W.; Jung, W.-G.; Cho, H.; Bae, T.-S.; Chang, S.-J.; Jang, J.-S.; Hong, W.-K.; Kim, B.-J. Substrate-mediated strain effect on the role of thermal heating and electric field on metal-insulator transition in vanadium dioxide nanobeams. *Sci. Rep.* **2015**, *5*, 10861.
- [49] Hu, B.; Zhang, Y.; Chen, W.; Xu, C.; Wang, Z. L. Self-heating and External Strain Coupling Induced Phase Transition of VO₂ Nanobeam as Single Domain Switch. *Adv. Mater.* **2011**, *23*, 3536-3541.
- [50] Sedlmayr, A.; Mönig, R.; Boles, S.T.; Kilibarda, G.; Kraft, O. Strain-induced phase transformation and piezoresistivity in VO₂ nanowires. *MRS COMMUN.* **2012**, *2*, 41-45.

4.3 Mechanically robust, stretchable solar absorbers with submicron-thick multilayer sheets for wearable and energy applications

4.3.1 Introduction

Solar thermal technologies, which convert solar energy into heat, have received increasing interest during the past few decades and are considered a promising candidate due to high energy storage density and high energy conversion efficiency in many emerging applications such as solar collectors^{1, 2} for heating and cooling systems, solar cookers^{3, 4}, solar heated clothes^{5, 6}, and steam generators⁷⁻⁹. The solar thermal efficiency is strongly dependent on the optical properties of the solar absorber. In general, for high-temperature applications, optimal solar-thermal energy conversion¹⁰⁻¹³ can be achieved by selectively absorbing solar energy with high infrared (IR) transmittance. With the high efficiency, it should be easy to manufacture and cost-effective, chemically and thermally stable at elevated temperatures.

Oxide-based cermetes have been widely studied, providing some of the few commercially available solar selective coatings. Esposito et al. fabricated multi-layer structures based on the composites of metallic particles and dielectrics (Mo-SiO₂), in which solar absorptance was higher than 0.94¹⁴. Mo-Al₂O₃ cermet selective surfaces using the double cermet layer structure with an absorptance of 0.955¹⁵ were also deposited by vacuum co-evaporation. The thickness of the film, and the size and concentration of the metallic particles have been considered as main factors for the selective absorption. There are, however, some issues about nonuniform film thickness, high thermal emittance, and the environmental concerns of electroplating method usually used.

Recently, metamaterial absorbers¹⁶⁻¹⁹, typically made of metals (e.g., Au, Ag, Ni) and dielectrics (e.g., HfO₂, SiO₂, Al₂O₃) are able to significantly increase the optical cross section of the structure, leading to greatly enhanced absorption in certain wavelength ranges caused by surface plasmon excitations. A plasmonic resonant visible light absorber, composed of a square array of vertically coupled nanowires coated with metal film, was developed, achieving ca. 75 % average absorption over a wavelength range from 0.4 to 0.8 μm. Hedayati and coworkers proposed perfect plasmonic metamaterial absorbers with an absorption of around 100 % over the entire visible region²⁰. However, the metamaterials require accurate lithography techniques for sub-wavelength feature sizes such as metallic concentric ring patterns and the absorption is critically dependent on the absorption angle. Flexible and stretchable substrates, such as polymer and fabrics, also limit the size of metadata that can be achieved with mechanical deformations that are not available in flexible applications.

Here, we demonstrate a facile scalable method to fabricate mechanically robust, stretchable solar absorber with broad band absorption for stretchable heat generation and enhanced thermoelectric generation. The absorber is a very thin (~ 500 nm) film, composed of metal/dielectric multilayer by alternating e-beam evaporation. By a matrix method, based on the medium boundary and propagation

matrices²¹, the titanium (Ti) and magnesium fluoride (MgF₂) was chosen and the structure was optimized for a high solar absorption. The multilayer thin films were known to have an enhanced absorption caused by multiple reflections at layer interfaces, however, most of works have focused on the high temperature generation²²⁻²⁴. Furthermore, the dielectrics were usually prepared on an elevated temperature. Recently, ultra thin film-based planar solar absorbers were reported to have broadband and wide-angle optical absorption properties by using two-dimensional materials and metallic substrates²⁵⁻²⁷. However, these methods may not be available at wearable substrates such as fabrics.

Carbonaceous films can be considered as an existing technology of the absorber owing to the abundance in nature and the excellent properties, such as high absorption over the solar spectrum and stability against heat, water and chemicals^{28, 29}. However, due to the poor adhesion on the wearable materials, such as fabrics, it cannot be also applicable to the wearable applications. Low-/mid-temperature absorbers were also reported by employing various methods such as paint coating, deposited cermet, and chemical conversion, such as CrN–Cr₂O₃, TiC/TiOxNy/AlN, and Ni–NiO etc.³⁰ Although these absorbers have a high absorptance over 90 %, the flexibility and mechanical strength was not clear. Here, the mechanical robustness for the wearable application was achieved by applying the mechanical stresses such as bending and stretching to the film, which produces a lot of micro-sized sheets of approximately 500 nm in thickness. They clearly showed great adhesion on any stretchable substrates. The absorbers showed a high absorption of approximately 85 % over a wavelength range from 0.2 to 4.0 μm and the selective absorption can be tuned by the thickness of each layer. Under 1-sun illumination, the solar absorber increased the substrate temperature to approximately 60°C and there was no significant decrease in the temperature under highly bent and stretched condition, or even after washing or rubbing them several times. The film was also deposited on the top surface of thermoelectric generator and the output power was enhanced by approximately 60 % under 1-sun irradiation. With incident solar radiation flux of 38.3 kW/m², the output power increased to 24 mW/cm² due to the increased surface temperature to 141°C.

4.3.2 Experimental

Fabrication of solar absorber and FDTD simulation

The samples, consisting of a layered metal/dielectric film structure, were fabricated by electron beam evaporator (KVE-T8897) at room temperature. The metal and dielectric films were deposited from targets of 99.99 % purity with a background pressure of 5.0×10^{-6} Torr. To control and adjust the layer thickness, the deposition rate of Ti and MgF₂ was calibrated in advance under the condition, 0.1 nm/s and 0.25 nm/s, respectively. The surface morphology of the film was characterized using tapping mode atomic force microscope (AFM). In order to optimize the optical absorption of the structure, FDTD solutions software with a RF module was also employed for two-dimensional finite element frequency domain simulation.

Optical properties measurement of solar absorber

The scanning electron microscopy (SEM) was done using a cold field emission scanning electron microscope (FE-SEM, S-4800, Hitachi) with an accelerating voltage of 10 kV. Absorption data were obtained at wavelengths ranging between 250 and 2500 nm using a UV-Vis spectrometer (Perkin-Elmer Lambda 750) equipped with specular reflectance spectroscopy. To see the optical properties with the incident angle, the specular spectra were obtained with the angles of incidence ranging from 20 ° to 70 ° using variable angle specular reflectance accessory. For the IR absorption measurement, the spectra were acquired with a Perkin-Elmer Spectrum and a Fourier transformed infrared (FTIR) spectrophotometer (vertex 80v) in the range of 2.5 – 4 μm. FTIR spectra were measured with a 10 ° specular reflectance accessory and a gold substrate alignment mirror at room temperature and the spectral resolution was about 0.9 cm⁻¹.

Application of solar absorber to wearable solar heater and thermoelectric generator

The optimized solar absorber was deposited on various polyurethane film, fabrics (linen, spandex, cotton napping and cotton) and PDMS in the same way. The temperature images were captured in real-time by an IR camera (GILTRON GTE-P). The absorber was also deposited to the hot side of a commercial thermoelectric generator module (1MC04-030-03 RMT thermoelectric) and an aluminium substrate was attached to the cold end of the module with thermally conductive sliver paste. The thermoelectric generator was tested by solar cell simulator with a xenon lamp (McScience XES-301S) and under AM 1.5G illumination at an intensity of 100 mW cm⁻². A Keithley instrument was used to measure the output performance.

4.3.3 Result and discussion

Multilayer films of Ti/MgF₂ and the flexibility

The absorber was mainly composed of titanium (Ti) metal and magnesium fluoride (MgF₂). As a key material for enhancing the adhesive property, a 7.3 nm-thick Ti layer was deposited via e-beam evaporation at a very low deposition rate of 0.1 nm/s on the substrate. The dielectric film of MgF₂ was then deposited on the Ti layer in the same way, with nanometer range of thickness from 20 to 300 nm. Finally, the film consists of 5 stacks of alternating Ti and MgF₂ films, with a total thickness of approximately 0.52 μm when the 96.5 nm-thick MgF₂ is deposited. The very thin (of submicron thickness) film is expected to have excellent mechanical robustness³¹. A cross-sectional SEM image in Figure 25a clearly confirms the alternating stacked film of 520 nm in thickness on glass substrate of 3 × 4 cm area. It was to be seen quite dark, meaning that the visible light absorption was high. The AFM images in Figure 26 also show that the film has quite low root mean square value of about 2.8 nm, meaning that it is very flat.

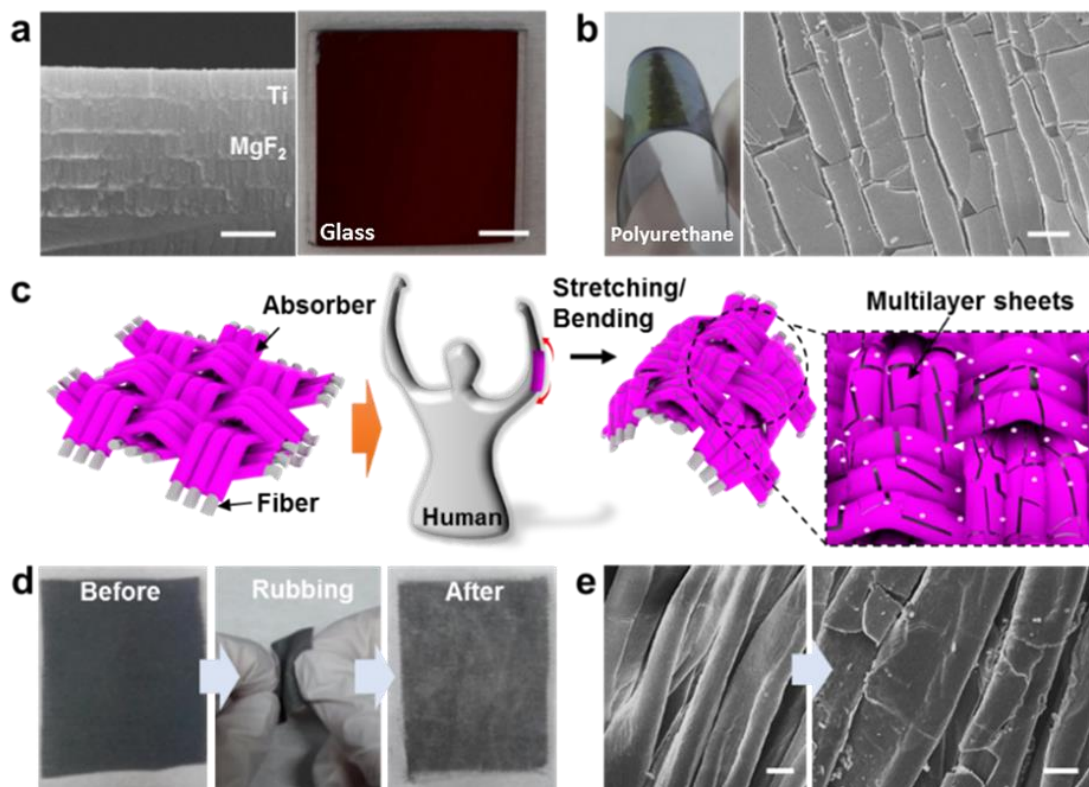


Figure 25. (a) (left) Cross-sectional SEM image and (right) photo of the multilayer film deposited on glass substrate. The scale bar is 0.2 μm and 1 cm, respectively. (b) Photo showing bending of the multilayer deposited on polyurethane and SEM image after the bending (scale bar 50 μm). (c) Schematic illustration showing that the micro-sized sheets are produced after simple mechanical stresses such as bending and stretching. (d) Photos of fabric with the absorber before and after the rubbing (e) SEM image of each fabric (The scale bar 10 μm , respectively).

The multilayer was also deposited on the flexible polyurethane substrate. It is well-known that the fabric made of polyurethane film is a waterproof fabric and used in several industries such as active wears³². After it was bent several hundreds of times, as shown in Figure 25b, the SEM image showed that many micro-sized sheets, showing excellent adhesion to the substrate, were produced. This means that the solar absorber is applicable to the fabric for wearable applications. Figure 25c shows the schematic illustration for fabricating the stretchable solar absorber with micro-sized sheets by simple bending and stretching processes. To demonstrate feasibility, the solar absorber was deposited on the cotton fabric (Figure 25d), rubbed several times. After that, the fabric seemed to have been made a little whiter. However, the SEM image (Figure 25e) showed that the sheets were quite adhesive to the fabric without any serious peel-off. This shows the excellent adhesion properties of the film and the possibility of application that can be worn.

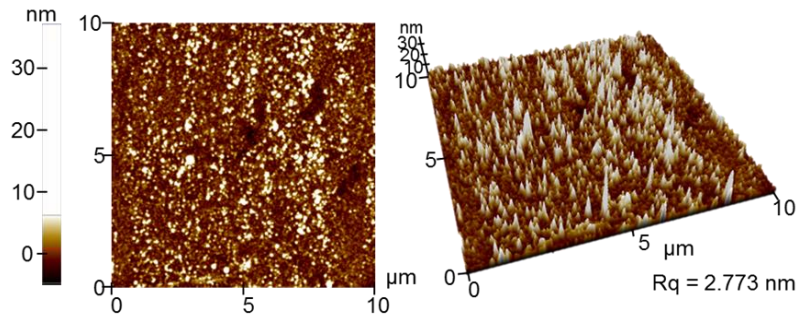


Figure 26. 2D and 3D AFM images of the absorber deposited on glass.

Optimization for a high efficient solar absorber

The light absorption of the multilayered film, composed of metal and dielectric layers, is based on the multiple reflections at the layer interfaces. After the light entering the film, the light is reflected back and forth at the interfaces. In general, the high absorption in the stack is resulted from multi-pass of light through the dielectric layer. The reflected light should destructively interfere due to the phase difference between the alternating layers, thus, the reflected light is canceled. Thus, we simulated and optimized the thickness of each layers to enhance the destructive optical interferences of the reflected light.

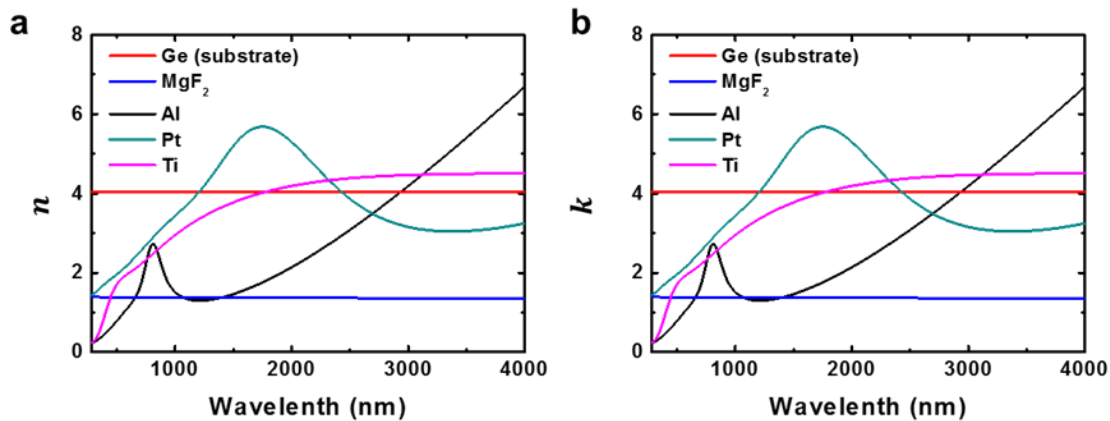


Figure 27. Refractive indices of each materials (Al, Pt, Ti) with wavelength.

To optimize the structure of the metal/dielectric multilayer film for a high efficient solar absorber, we estimated the solar absorptance for various multilayer films based on the Maxwell's equations and the solar irradiance. We assumed normal incidence of the solar light to the film surface. To calculate the optical properties of the multilayer film structure, Maxwell's equations were adopted to the multilayer structure with refractive indices³³⁻³⁵ as shown in Figure 27, and the boundary conditions at each interface were applied. For detailed calculation method, see Figure 27a. Figure 28 indicates representative calculation results for absorptance as a function of wavelength for given 5-stack Ti/MgF₂ multilayer

films. The absorbance spectrum changes dramatically according to the thickness of each layer. The steep drop occurs when the wavelength of the light is comparable to the periodicity of the alternating film structure (see Figure 29 for detail). Since the most of the solar irradiance is located at the visible light range as shown in the lower part of Figure 28a, such absorption dips should be avoided at that range for the high solar absorption.

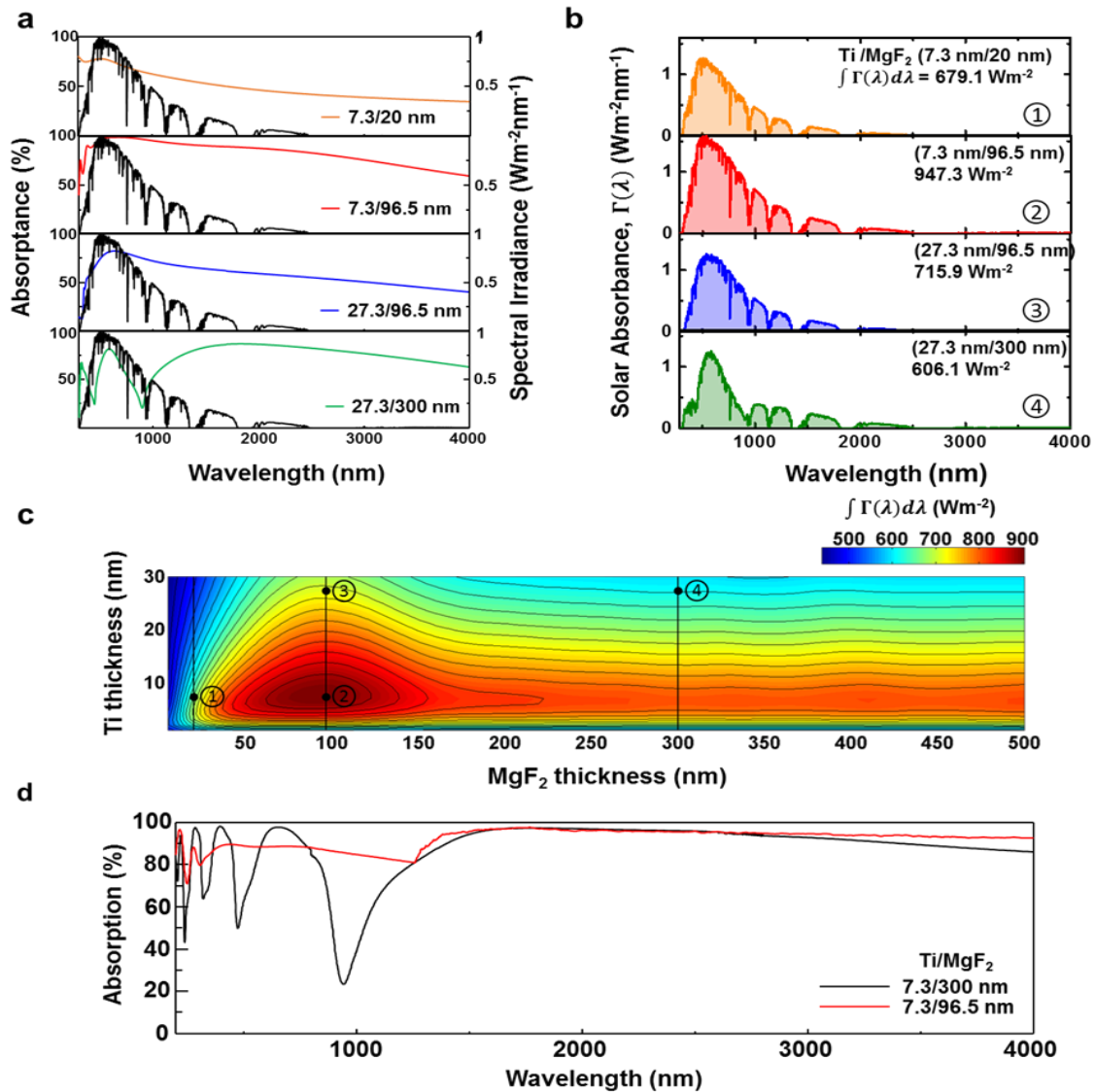


Figure 28. (a) Calculated absorbance and solar irradiance as a function of wavelength for given multilayer films. (b) The solar absorption spectrum with different thickness of multilayers. (c) Total solar absorption versus thickness of each layer, Ti and MgF₂. (d) Absorption measured by UV-Vis-NIR spectroscopy and Fourier transformed infrared spectroscopy over a wavelength range from 0.2 to 4 μm .

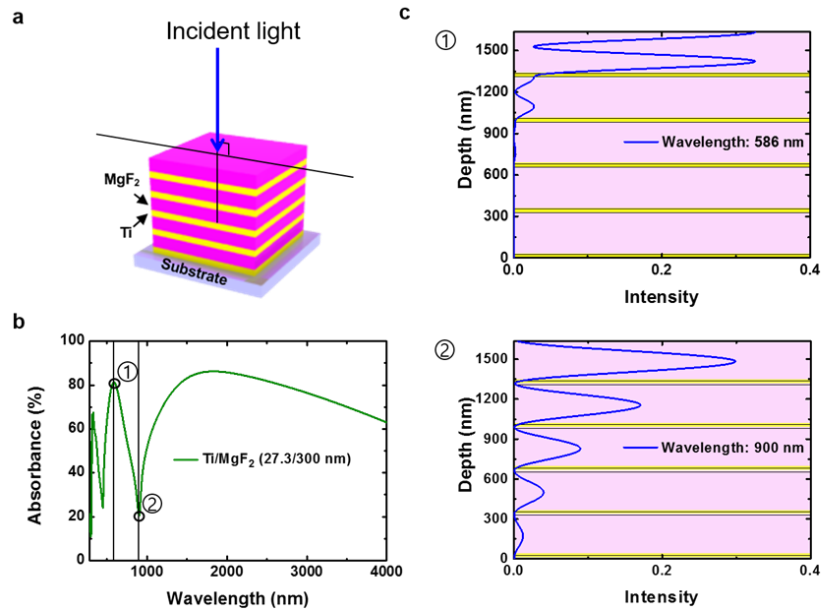


Figure 29. (a) Schematic of the case of a normal incident light for multilayers. (b) An example of absorption-spectrum calculation for Ti (27.3 nm)/MgF₂ (300 nm) multilayer structure. (c) The electric field profile through the thickness from the propagation matrix.

To obtain the solar absorption spectrum, (λ), the solar irradiance (the lower part of Figure 28a) was multiplied to the calculated absorption spectrum (the upper part of Figure 28a) for a given multilayer film as shown in Figure 28b. The area ($\int I(\lambda)d\lambda$) of the solar absorption spectrum reflects the total solar absorption which directly relates the heat generation of the solar absorber. It should be noted that the integration of the solar absorption spectrum was done with respect to the wavelength ranging from 280 nm to 4000 nm which are available data range of the solar irradiance³⁶. The area for the multilayer structure with 7.3-nm Ti and 96.5-nm MgF₂ thickness which has smooth and high absorption profile for visible light range shows the highest total solar absorption, whereas the structure with 27.3-nm Ti and 300-nm MgF₂ thickness which shows huge dips at the visible light range shows the lowest value of the total solar absorption.

To optimize the 5-stack Ti/MgF₂ multilayer structure, we calculated the total solar absorption versus thickness of each layer, Ti and MgF₂ as shown in Figure 28c. We found that the highest value of the total solar absorption occurs at the thickness of Ti and MgF₂ are 7.3 nm and 96.5 nm, respectively, which was chosen in our experiments. Further increase in the thickness significantly decreased the solar absorption of the layer although the adhesive properties of the layer can be expected to be enhanced with thicker Ti layer. Furthermore, we optimized 5-stack metal/dielectric (MgF₂) multilayer structure for other metal materials Al and Pt. Figure 30 reveals the optimum structure for each metal and Ti shows the best total solar absorption among these metals. Additionally, there was no significant increase in the solar absorption when the number of layer is larger than 5, as shown in Figure 31.

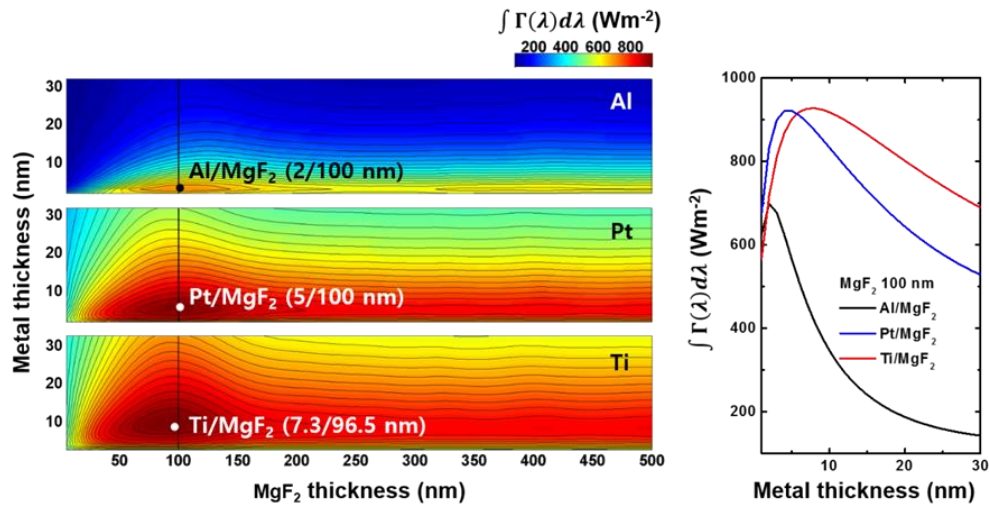


Figure 30. The total solar absorption of the optimum metal thickness for Al, Pt and Ti.

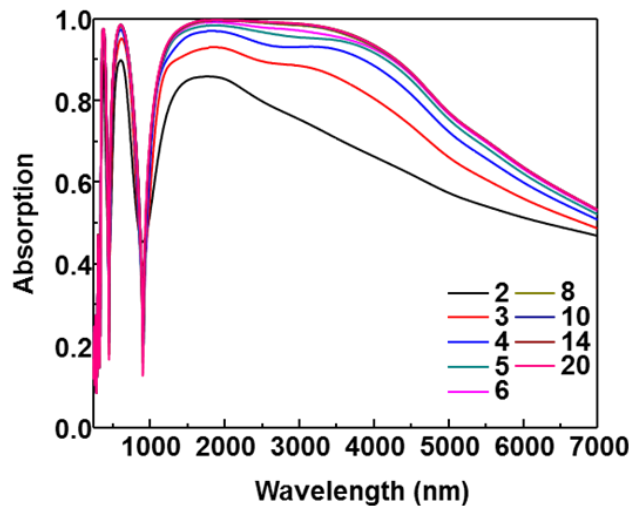


Figure 31. The simulated solar absorption of the multilayer as a function of the number of the layer.

Figure 28d shows the optical absorption spectra of the absorber with different thickness (7.3 nm/96.5 nm and 7.3 nm/300 nm, respectively) deposited on a glass substrate over a wavelength range from 0.2 to 4.0 μm using UV-VIS-IR spectroscopy with specular reflectance spectroscopy. At 7.3 nm/300 nm, the measured absorption spectrum demonstrates the quite high absorption of the film in the wavelength range, while an oscillation is clearly seen in the visible region due to the phase and intensity interference effect, suppressing the light reflection of the film³⁷. As the thickness of the MgF_2 decreased to 96.5 nm, which showed the highest total solar absorption in Figure 28c, the spectra showed quite high light absorption of approximately 85 % over a wavelength range from 0.2 to 1.0 μm with higher absorption

of UV and IR light. However, this absorption in visible light is not as high as expected, possibly due to variations in the thickness of each layer. However, the absorption spectra show a high-consistency with the simulation results with to the wavelength. The optical absorption spectra were obtained with the angle of incidence ranging from 20° to 70° , plotted in Figure 32. As the angle decreases, a little decrease in light absorption is observed, but there is no significant decrease by 30° and the rate of the decrease in the absorption with the angle is smaller than that of metamaterial based absorber reported previously³⁸. Finally, the optical absorption of the optimized absorber was also measured after annealing at 200°C and 400°C for 1 hr to investigate the stability of the absorber at the high temperatures, plotted in Figure 33. It was clearly seen that there is no significant decrease of the absorption even after annealing at 400°C , meaning that the multilayered film was so stable.

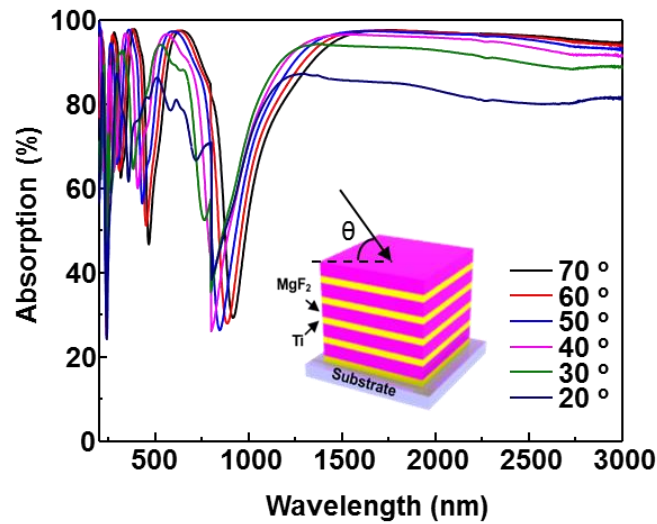


Figure 32. The optical absorption of the multilayered films with the incident angle.

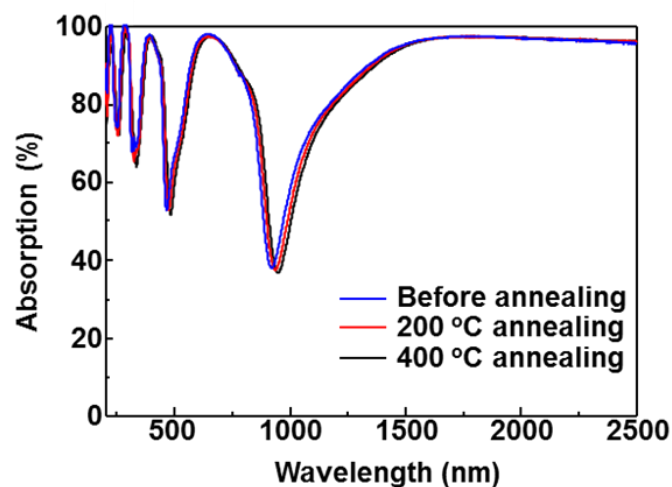


Figure 33. The optical absorption of the multilayered films as a function of annealing temperature.

Stretchable Heat Generation based on Solar Thermal Energy Conversion

The absorber with number of stacks of alternating Ti and MgF₂ films was deposited on polyurethane and the surface temperatures of the polyurethane were measured as a function of measuring time under AM1.5G illumination (100 mW/cm², 1-sun) at room temperature, plotted in Figure 34a. Without light illumination, it was measured to be approximately 30°C. As the light turns, the temperature increased up to 32°C within 5 min and there was no more significant increase after that. As 2-stack (Ti/MgF₂) was deposited, the temperature increased up to 48°C. As the number of the stacks increased to 5, the temperature was reached up to 61°C. The significant increase was clearly also seen in the thermal image measured by an IR camera in Figure 34b. The absorber was also deposited on a variety of fabrics such as linen, spandex, cotton napping and cotton. Irrespective of the kind of fabrics, as shown in Figure 35, the other fabrics were also heated to 67 ~ 73°C, showing an increase of the temperature by approximately 26°C. For the real wearable application, the temperature of the absorber deposited on cotton substrate was measured outdoors by an IR camera. The intensity of the light outside was measured to be about 80 mW/cm². With the incident light, it was observed that the temperature increased up to about 50.1°C within 10 min, while the substrate without absorber increased up to 32.1°C, as shown in Figure 36. This shows that the absorber can be promising as a potential candidate of wearable solar heater.

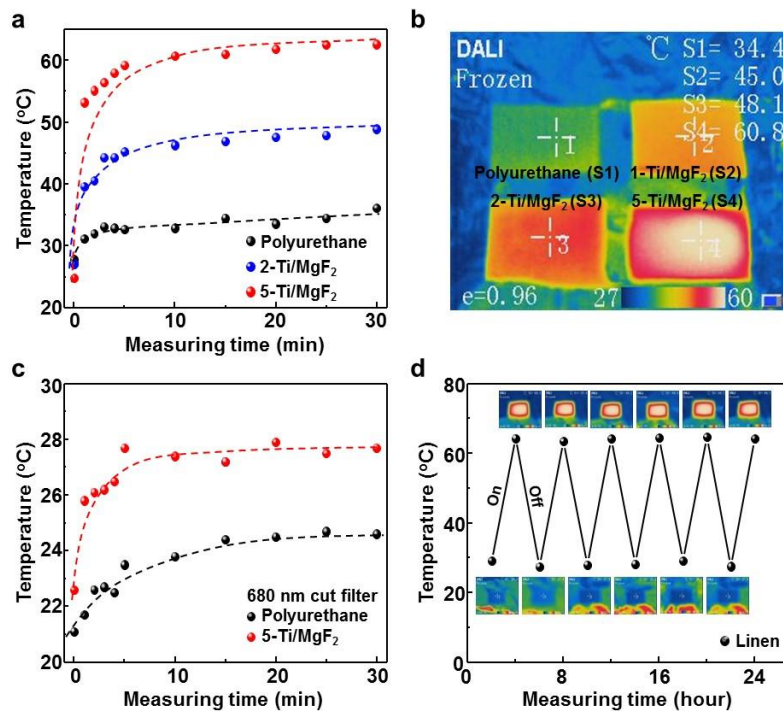


Figure 34. (a) Surface temperature (b) Top view thermal image of the multilayer (Ti/MgF₂ = 7.3 nm/96.5 nm) deposited on polyurethane as a function of the number of layers under 1-sun illumination. (c) Surface temperature measured under illumination of 680 nm-filtered light (> 680 nm). (d) Surface temperature obtained by turning on and off repeatedly every 10 mins.

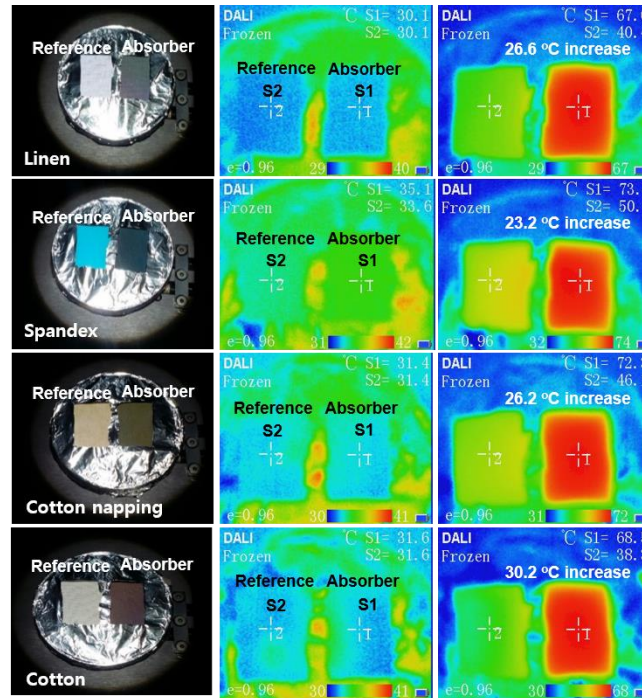


Figure 35. The photograph and thermal image comparison of absorber deposited on fabrics such as linen, spandex, cotton napping and cotton under AM 1.5G illumination.

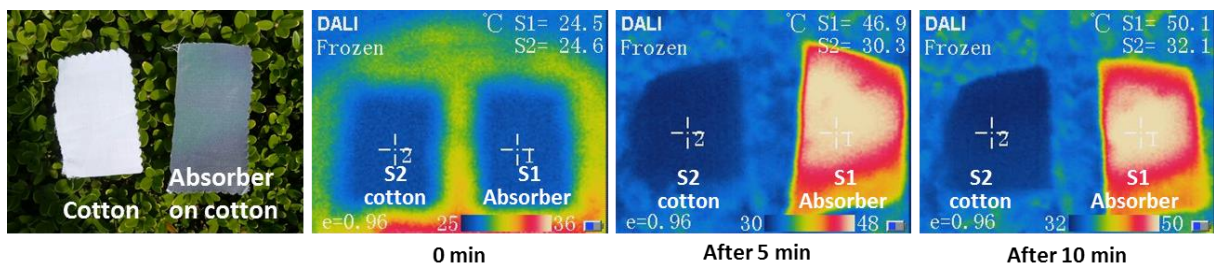


Figure 36. Real photos of cottons with and without absorber. The surface temperatures of the substrates were measured as a function of measuring time outside.

The increase of the temperature by the light illumination is due to the solar light absorption³⁹. As mentioned above, the solar thermal energy conversion efficiency is critically dependent on the solar selective absorption properties, such as large absorption in visible light and large transmission in infrared light. Here, the film showed a high absorption (> 80 %) in visible light, while a significant absorption (approximately 70 ~ 80 %) was also observed over a wavelengths range from 1 to 4 μm . The measured absorption spectra showed a high consistency with those simulated. With only IR and near-IR light at wavelengths higher than 680 nm, the temperature was also increased by approximately 4 ~ 5°C, as shown in Figure 34c. This means that we can wear warmer clothes on cloudy or cold days without the sun. The temperature increase by sunlight was repeated several times and there was no significant change in the temperature, showing good reproducibility, as shown in Figure 34d.

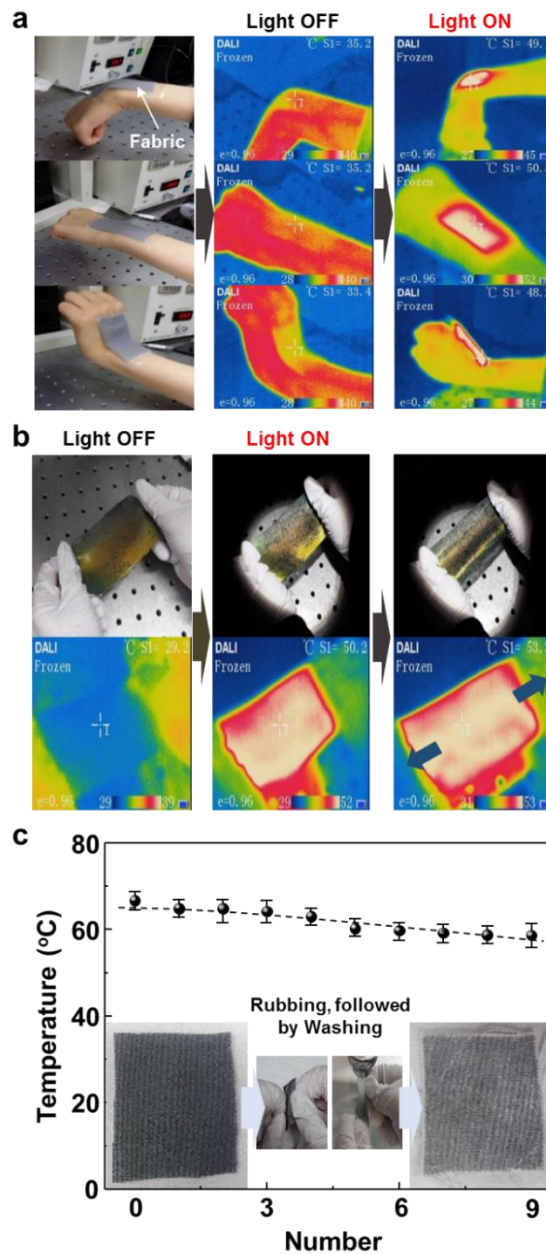


Figure 37. (a) Photos and thermal images of the fabrics with the absorber attached on the surface of a wrist under concave bending (top), neutral (center) and convex bending (bottom) condition. (b) Photos and thermal images of PDMS with the absorber under highly stretched condition. (c) Surface temperature measured under 1-sun illumination after rubbing and washing several times the fabrics. The inset shows the photos and thermal images.

Further evaluation was performed to see the durability and stability under various mechanical stresses such as bending, stretching, rubbing, and even washing. As a test substrate, cotton fabric with the solar absorber was attached on the surface of the human wrist with a sticking plaster and the temperature was measured with the bending motion, as shown in Figure 37a. Without the light illumination, the

temperature of the cotton was approximately 35°C, a little lower than that of human skin. As the light was turned on, the temperature increased up to 50.5°C, 15°C higher than that of human skin. When the wrist was under both concave and convex bending, the temperature was measured to be 49.1 and 48.2°C, respectively, indicating that there was no significant change in the temperature depending on the direction of the bending. A video clip clearly showed real-time temperature evolution of the fabric in supplementary Movie 1a in Supporting Information. The absorber was also deposited on PDMS and was stretched by approximately 36.4 % for 1 min. We found that there was also no significant change in the temperature, as shown in Figure 37b. This demonstrates good stability and durability with mechanical disturbances including compression and tensile strain. Finally, the cotton fabric with the absorber was rubbed by a human hand for 1 min and washed in flowing DI water. It was repeated several times and the temperature was measured after it was fully dried, as shown in Figure 37c.

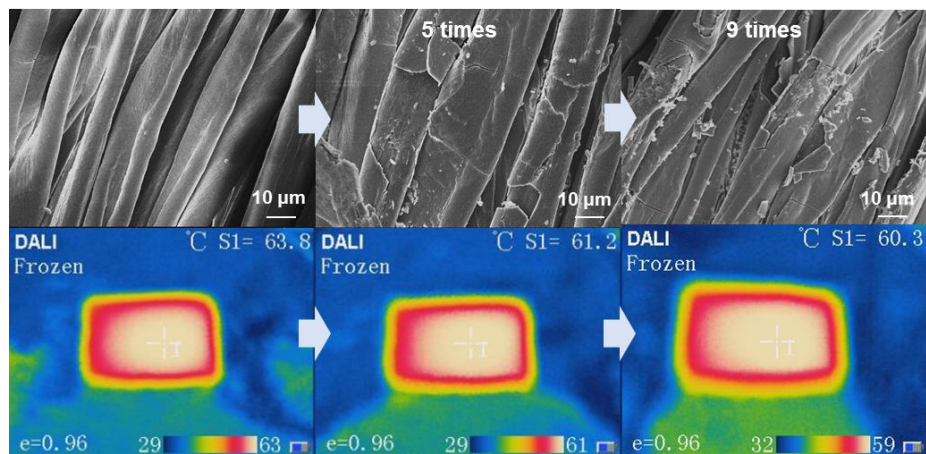


Figure 38. SEM images of the absorber on cotton fabrics after rubbing and washing several times and thermal images of the samples measured under AM 1.5G illumination.

As the number of the mechanical stresses increased, it was found that it decreased very slowly, due to the peel-off the absorber from the fabric. However, Figure 38 shows that the peel-off of the film is not significant at even 9 times. There is no significant decrease of the light absorption after the mechanical stresses are applied, as shown in Figure 39. There was also no change in the temperature in the temperature even after bending 200 times, as shown plotted in Figure 40. These results indicate the mechanical robustness of the absorber on the fabric.

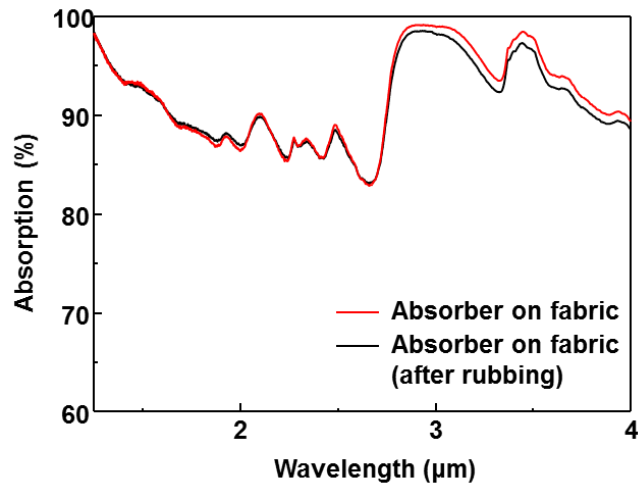


Figure 39. The optical absorption of the cotton fabrics with the absorber before and after rubbing.

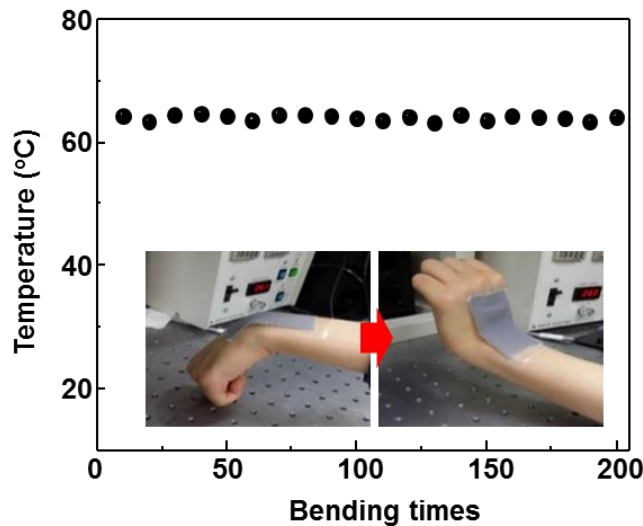


Figure 40. The temperature of the absorber as a function of bending times.

Enhanced Output Power of Thermoelectric Generator

The heat generated by the solar absorber may be effective in enhancing the output power of the thermoelectric generator without any other heat sources. The absorber was deposited on the alumina (Al_2O_3) top layer of a thermoelectric module and the output power of the thermoelectric generator was then examined. Figure 41a shows the schematic diagram of the thermoelectric generator and the measurement system used when the output power was measured. The size of the active area in the thermoelectric generator is approximately $1.5 \text{ cm} \times 1.5 \text{ cm}$ and the absorber covers the entire area. The efficiency of the thermoelectric generator was measured under AM1.5G illumination (100 mW/cm^2 , 1-sun) at room temperature. To generate a temperature difference across the thermoelectric generator and investigate its output characteristics, a cooling system was set up and the temperature of the cold side

could be changed from 5 to 30°C. Figure 41b shows the temperature difference of thermoelectric generator as a function of cooling temperature from 5 to 30°C. At the cooling temperature of 5°C, the thermoelectric generator with the absorber showed that the top and bottom temperature difference increased up to 18.4°C, 26 % higher compared to that without the absorber. As the temperature increased, the difference also decreased, meaning that the maximum temperature of the top layer was approximately 39.2°C.

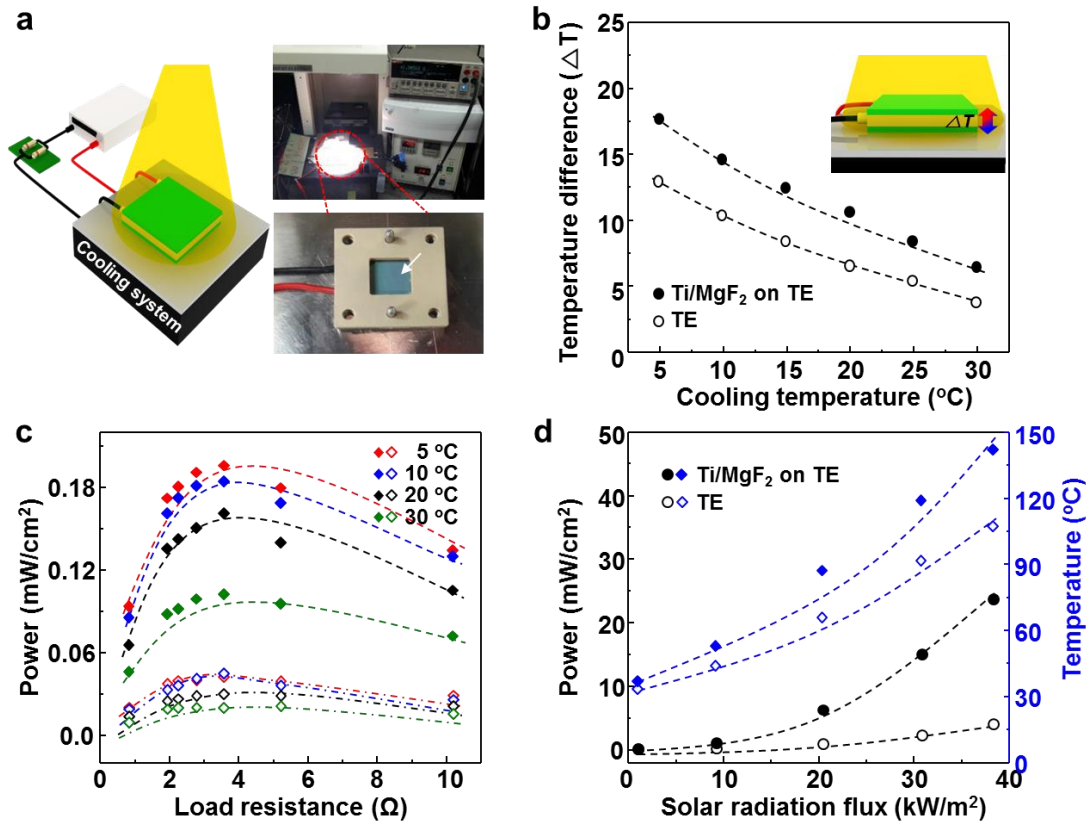


Figure 41. (a) (left) Schematic images of the solar absorber formed on the top surface of the thermoelectric generator and (right) the measurement tools. (b) Temperature difference of the thermoelectric generator as a function of cooling temperature. The open and closed diamonds are the output powers of thermoelectric generators with and without the solar absorber, respectively. (c) Output power of the thermoelectric generator as a function of load resistance. (d) Output power and surface temperature of the thermoelectric generator as incident solar radiation flux.

We also measured the output power of the thermoelectric generator as a function of load resistance from 1 to 10 ohm, plotted in Figure 41c. Due to the large temperature difference at low cooling temperature, the output power increased as the cooling temperature decreased. At the ambient temperature of 20°C, the thermoelectric generator with the absorber showed 0.07 mW/cm², 60 % higher compared to that without the absorber. The output power increased with load resistance up to 0.16

mW/cm² at 3.58 Ω and the power enhancement by the absorber also increased up to 433 %. Further increase in the load resistance significantly decreased the output power because the load resistance became larger than the internal resistance of thermoelectric generator module. For a given temperature difference and a given TEG, the output power is only a function of the load resistance applied to the circuit, as below;⁴⁰

$$P_{TEG} = \frac{(N\alpha_{Circuit})^2 (T_H - T_c)^2}{R_{TEG} + R_{Load}} - \left[\frac{N\alpha_{Circuit} (T_H - T_c)}{R_{TEG} + R_{Load}} \right]^2 R_{TEG} \quad (1)$$

Thus, the maximum power is achieved when the load applied to the thermoelectric generator is equal to the resistance of the thermoelectric generator. The solar light was also concentrated by using a Fresnel lens and the thermoelectric generator was then exposed to the concentrated light. The absorber significantly increased the power of the thermoelectric generator up to 24 mW/cm² at incident solar radiation flux of 38.3 kW/m² due to the increase in the temperature of the top layer up to 141°C. However, there was no such significant increase in the thermoelectric generator without the absorber.

4.3.4 Conclusion

Here, we reported a facile scalable method to fabricate a stretchable solar absorber, based on the very thin (~ 500 nm) periodic metal/dielectric multilayer and the use of titanium. After various mechanical stresses such as bending, stretching, and rubbing were applied, a lot of micro-sized sheets with 500 nm thickness were produced and they still showed great adhesion on stretchable substrates such as fabrics and PDMS. The optical absorption spectra showed that it has high light absorption of approximately 85 % over a wavelength range from 0.2 to 4.0 μm. Two-dimensional finite element frequency domain simulation supported the high visible light absorption of over 90 %.

Under 1-sun illumination, the solar absorber on various stretchable substrates increased the temperature to approximately 60°C, irrespective of various mechanical stresses such as bending, stretching, rubbing, and even washing. The thermoelectric generator with the absorber also showed an enhanced output power of 60 % compared to that without the absorber. With incident solar radiation flux of 38.3 kW/m², the output power increased to 24 mW/cm² with the increased surface temperature of 141°C. These results may show the possibility of the absorber for wearable energy applications, operable by only sunlight.

4.3.5 Reference

- [12] Tian, Y.; Zhao, C.Y. A Review of Solar Collectors and Thermal Energy Storage in Solar Thermal Applications. *Appl. Energy*. **2013**, 104, 538-553.
- [13] Zhu, G.; Wendelin, T.; Wagner, M.J.; Kutscher, C. History, Current State, and Future of Linear Fresnel Concentrating Solar Collectors. *Solar Energy*. **2014**, 103, 639-652.
- [14] Cuce, E.; Cuce, P.M. A Comprehensive Review on Solar Cookers. *Appl. Energy*. **2013**, 102, 1399-1421.
- [15] Cuce, E.; Cuce, P.M. Theoretical Investigation of Hot Box Solar Cookers Having Conventional and Finned Absorber Plates. *International Journal of Low-Carbon Technologies*. **2015**, 10, 238-245.
- [16] Zhu, J.; Riffat, S.; Oliveira, A.C. Experimental Study on Solar Clothes Dryer using Evacuated Tube Collector and PV Panel. *Journal of Energy & Climate Change*. **2008**, 3, 125-132.
- [17] Autier, P.; Dore', J.-F.; Cattaruzza, M.S.; Renard, F.; Luther, H.; Silverj, F.G.; Zantedeschi, E.; Mezzetti, M.; Monjaud, I.; Andry, M.; Osborn, J.F.; Grivegne, Sunscreen Use, Wearing Clothes, and Number of Nevi in 6-to 7-year-old European Children. *J. Natl. Cancer Inst.* **1998**, 90, 24.
- [18] Polman, A. Solar Steam Nanobubbles. *ACS Nano*. **2013**, 7, 15-18.
- [19] Sandler, J.; Fowler, G.; Cheng, K.; Kavscek, A.R. Solar-Generated Steam for Oil Recovery: Reservoir Simulation, Economic Analysis, and Life Cycle Assessment. *Energy. Convers. Manag.* **2014**, 77, 721-732.
- [20] Rovira, A.; Montes, M.J.; Varela, F.; Gil, M. Comparison of Heat Transfer Fluid and Direct Steam Generation Technologies for Integrated Solar Combined Cycles. *Appl. Therm. Eng.* **2013**, 52, 264-274.
- [21] Li, P.; Liu, B.; Ni, Y.; Liew, K.K.; Sze, J.; Chen, S.; Shen, S. Large-Scale Nanophotonic Solar Selective Absorbers for High-Efficiency Solar Thermal Energy Conversion. *Adv. Mater.* **2015**, 27, 4585-4591.
- [22] Lenert, A.; Wang, E.N. Optimization of Nanofluid Volumetric Receivers for Solar Thermal Energy Conversion. *Solar Energy*. **2012**, 86, 253-265.
- [23] Lizama-Tzec, F.I.; Macías, J.D.; Estrella-Gutiérrez, M.A.; Cahue-López, A.C.; Arés, O.R.; Coss, de.; Alvarado-Gil, J.J.; Oskam, G.J. Electrodeposition and Characterization of Nanostructured Black Nickel Selective Absorber Coatings for Solar-Thermal Energy Conversion. *Mater Sci: Mater Electron*. **2015**, 26, 5553-5561.
- [24] Yang, J.; Qi, G.-Q.; Tang, L.-S.; Bao, R.-Y.; Bai, L.; Liu, Z.-Y.; Yang, W.; Xie, B.-H.; Yang, M.-B. Novel Photodriven Composite Phase Change Materials with Bioinspired Modification of BN for Solar-Thermal Energy Conversion and Storage. *J. Mater. Chem. A*. **2016**, 4, 9625-9634.

- [25] Esposito, S.; Antonaia, A.; Addonizio, M.L.; Aprea, S. Fabrication and Optimisation of Highly Efficient Cermet-Based Spectrally Selective Coatings for High Operating Temperature. *Thin Solid Films*. **2009**, 517, 6000-6006.
- [26] Zhang, Q.-C.; Yin, Y. D.; Mills, R. High Efficiency Mo-Al₂O₃ Cermet Selective Surfaces for High-Temperature Application. *Sol. Energy Mater. Sol. C*. **1996**, 40, 43-53.
- [27] Shrekenhamer, D.; Chen, W.-C.; Padilla, W.J. Liquid Crystal Tunable Metamaterial Absorber. *PRL*. **2013**, 110, 177403.
- [28] Huang, L.; Chowdhury, D.R.; Ramani, S.; Reiten, M.T.; Luo, S.-N.; Taylor, A.J.; Chen, H.-T. Impact of Resonator Geometry and its Coupling with Ground Plane on Ultrathin Metamaterial Perfect Absorbers. *Appl. Phys. Lett*. **2012**, 101, 101102.
- [29] Li, W.; Guler, U.; Kinsey, N.; Naik, G.V.; Boltasseva, A.; Guan, J.; V Shalaev, M. A.; Kildishev, V. Refractory Plasmonics with Titanium Nitride: Broadband Metamaterial Absorber. *Adv. Mater*. **2014**, 26, 7959-7965.
- [30] Dayal, G.; Ramakrishna, S.A. J. Design of Multi-Band Metamaterial Perfect Absorbers with Stacked Metal–Dielectric Disks. *Opt*. **2013**, 15, 055106.
- [31] M. K.; Faupel, F.; Elbahri, M. Tunable Broadband Plasmonic Perfect Absorber at Visible Frequency. *Appl. Phys. A: Mater. Sci. Process*. **2012**, 109, 769.
- [32] Qiu, Z.Q.; Bader, S.D. Surface Magneto-Optic Kerr Effect. *Rev. Sci. Instrum*. 2000, 71, 1243-1255.
- [33] Gremion, C.; Seassal, C.; Drouard, E.; Gerthoffer, A.; Pelissier, N.; Ducros, C. Design, Properties and Degradation Mechanisms of Pt-Al₂O₃ Multilayer Coating for High Temperature Solar Thermal Applications. *Surf. Coat. Tech*. **2015**, 284, 31-37.
- [34] Jyothi, J.; Chaliyawala, H.; Srinivas, G.; Nagaraja, H.S.; Barshilia, H. C. Design and Fabrication of Spectrally Selective TiAlC/TiAlCN/TiAlSiCN/TiAlSiCO/TiAlSiO Tandem Absorber for High-Temperature Solar Thermal Power Applications. *Sol. Energy. Mat. Sol. C*. **2015**, 140, 209-216.
- [35] Selvakumar, N.; Barshilia, H.C.; Rajam, K.S.; Biswas, A. Structure, Optical Properties and Thermal Stability of Pulsed Sputter Deposited High Temperature HfO_x/Mo/HfO₂ Solar Selective Absorbers. *Sol. Energy. Mat. Sol. C*. **2010**, 94, 1412-1420.
- [36] Liu D, Li Q. Sub-Nanometer Planar Solar Absorber. *Nano Energy*, **2017**, 34: 172-180.
- [37] Liu D, Yu H T, Yang Z, Duan Y Y. Ultrathin Planar Broadband Absorber through Effective Medium Design. *Nano Res*, **2016**, 9: 2354-2363.
- [38] Liu D, Yu H T, Duan Y Y, Li Q, Xuan Y M. New Insight into the Angle Insensitivity of Ultrathin Planar Optical Absorbers for Broadband Solar Energy Harvesting. *Sci Rep*, **2016**, 6: 32515.
- [39] Chena, Z.; Jainb, A.; Boström, T. Simulation of Anti-Reflection Coated Carbonaceous Spectrally Selective Absorbers. *Energy Procedia*. **2014**, 58, 179-184.

- [40] Mastai, Y.; Polarz, S.; Antonietti, M. Silica-Carbon Nanocomposites: A New Concept for the Design of Solar Absorbers. *Adv. Funct. Mater.* **2002**, 12, 197-202.
- [41] Zhang, K.; Hao, L.; Du, M.; Mi, J.; Wang, J. -N.; Meng, J. -P. A Review on Thermal Stability and High Temperature Induced Ageing Mechanisms of Solar Absorber Coatings. *Renew. Sust. Eenergy. Rev.* **2017**, 67, 1282-1299.
- [42] Kim, B.J.; Shin, H.-A.-S.; Lee, J.-H.; Yang, T.-Y.; Haas, T.; Gruber, P.; Choi, I.-S.; Kraft, O.; Joo, Y.-C. Effect of Film Thickness on the Stretchability and Fatigue Resistance of Cu Films on Polymer Substrates. *J. Mater. Res.* **2014**, 29, 23.
- [43] ÖZDİL, N.; ANAND, S. Recent Developments in Textile Materials and Products Used for Activewear and Sportswear. *Electronic Journal of Textile Technologies.* **2014**, 8, 68-83.
- [44] ASTM G 173-03. Standard Tables for Reference Solar Spectral Irradiances: Direct Normal and Hemispherical on 37° Tilted Surface. West Conshohoken, PA: ASTM International; **2003**. DOI: 10.1520/G0173-03R12.
- [45] Li, H.H. J. Refractive Index of Alkaline Earth Halides and Its Wavelength and Temperature Derivatives. *Phys. Chem. Ref. Data.* **1980**, 9, 161.
- [46] Rakić, A.D.; Djurišić, A.B.; Elazar, J.M.; Majewski, M.L. Optical Properties of Metallic Films for Vertical-Cavity Optoelectronic Devices. *Appl. Opt.* **1998**, 37, 5271-5283.
- [47] Barnes, N.P.; Piltch, M.S. Temperature-Dependent Sellmeier Coefficients and Nonlinear Optics Average Power Limit for Germanium. *J. Opt. Soc. Am.* **1979**, 69, 178-180.
- [48] Saleh, B.E.A.; Teich, M.C.; Saleh, B.E. *Fundamentals of photonics.* **1991**, 22.
- [49] Ghasemi. M, Choudhury. P. K, Baqir. M. A, Mohamed. M. A, Zain. A. R, Majlis. B. Y, Metamaterial Absorber Comprising Chromium–gold Nanorods-Based Columnar Thin Films. *J. Nanophoton.* **2017**, 11, 043505.
- [50] Elsasser, W.M. Heat Transfer by Infrared Radiation in the Atmosphere. No. 6. Harvard University and Blue Hill meteorological observatory, USA, **1942**.
- [51] Finnerty, D. The Development of Methodologies and a Novel Test Facility for the Characterisation of Thermoelectric Generators. (Thesis) McMaster University, May, **2013**.

4.4 Optical design of ZnO-based antireflective layers for enhanced GaAs solar cell performance

4.4.1 Introduction

Antireflective (AR) coatings based the ZnO nanostructures have received increasing interest during the past few decades and may be considered as one of the promising candidates due to the excellent optical properties and the controllable anisotropic growth of ZnO¹⁻³. In particular, the ZnO can easily be synthesized as a various form of nanostructures such as nanowires, nanobelts, nanoplatelets, and nanorods by well-developed methods, demonstrated by many research groups⁴⁻⁸. However, as a promising candidate, most work has focused on the nanowires-based AR coatings. The graded refractive index to the active region of the solar cell, which is essential in obtaining low reflectance, can be achieved by the gradual decrease in the diameter of the nanowires to the bottom from the top⁹⁻¹³. Various experimental parameters such as substrate, growth time, temperature, amount of precursor and additives should be considered for the fine control of the nanowires diameter. However, the morphology was found to be quite sensitivity to these parameters. Recently, it was reported that the coaxial-type surface by coating low refractive index materials on the nanowires could decrease the reflectance, significantly at low angle of incident light, thereby, enhancing the solar cell performance over broadband and wide angle ranges^{14, 15}. However, the enhancement of the performance of solar cell with the ZnO nanowires-based AR coatings may not be huge, although the AR coatings show quite low reflectance comparable to those of conventional multilayered antireflective films¹⁶⁻²⁰.

Here, a series of hierarchical ZnO nanostructures-based AR coatings was synthesized and the reflection over a broadband range was simultaneously examined. The GaAs solar cells with the AR coatings were then fabricated and the AR characteristics were compared with the performance of the solar cell. As the nanostructures, the ZnO nanowires and nanosheets were prepared hydrothermally on high-refractive index layer (ZnS and TiO₂), followed by the RF sputtering of MgF₂ layer for coaxial nanostructures. For the nanosheets growth, very thin aluminium layer less than 1 nm was deposited on the ZnS layer by using e-beam evaporator. The nanosheets-based AR coatings exhibited large reflection in the range of 300 – 800 nm, > 5 % at a shorter wavelength than 450 nm, while ZnO nanowires-based coatings showed ~ 2 % in entire region. However, the GaAs single-junction solar cells with nanosheets-based AR coatings showed the largest enhancement of 43.9 %, compared with pristine solar cell. It is believed that the results are explained by the increase of the optical bandgap of the ZnO nanosheets by the incorporation of aluminum atoms, increasing the optical transmittance.

4.4.2 Experimental

Fabrication of ZnO nanowires and nanosheets

High-aspect-ratio ZnO based double-nanotextured surfaces with core-shell morphologies were prepared via a hydrothermal method of ZnO nanowires and nanosheets, followed by means of RF sputtering for

MgF₂ thin film deposition. For reflectance measurement of the antireflective surfaces, the nanowires were grown on ZnO/TiO₂ (100 nm/ 50 nm) and ZnO/ZnS (100 nm/ 50 nm) layers in a mixed solution of 0.020 M zinc nitrate hydrate and 0.020 M hexamethylenetetramine (HMT) in DI water for 9 hrs. The TiO₂ and ZnS were deposited by reactive sputtering using 80 W of RF power, 16 sccm of Ar and 4 sccm of O₂ at an operating pressure of 2 mTorr, and 50 W of RF power, 20 sccm of Ar at an operating pressure of 5 mTorr, respectively. The deposition condition was optimized to enhance good crystallinity. The ZnO, which acts effectively as the seed layer for growing ZnO nanowires, was then deposited by reactive sputtering using 100 W of RF power to the 2 in. ZnO target, 16 sccm (sccm denotes cubic centimeter per minute at STP) of Ar and 4 sccm of O₂ at an operating pressure of 4 mTorr. For the growth of ZnO nanosheets, very thin layer of aluminum (0.5 to 3 nm) was deposited on the ZnS layer, followed by the growth of the ZnO nanosheets under the same growth condition. The MgF₂/ZnO was fabricated using 80 W of RF power to the 2 inch MgF₂ target, 15 sccm of Ar at an operating pressure of 25 mTorr.

Fabrication of the GaAs single junction solar cell

The GaAs single junction solar cell structure was grown on a GaAs substrate by metal-organic chemical vapor deposition, in which AsH₃, PH₃, trimethylgallium (TMGa), and trimethylindium (TMIn) were used as precursors. SiH₄ and Dimethylzinc (DMZn) were also employed as *n*-type and *p*-type dopants, respectively. The structure consists of 0.5 μm thick Si-doped GaAs, 0.05 μm thick Si-doped, $3 \times 10^{18} \text{ cm}^{-3}$, Ga_{0.5}In_{0.5}P), 3.5 μm thick Si-doped GaAs, 0.5 μm thick Zn-doped, $1 \times 10^{18} \text{ cm}^{-3}$, GaAs), 0.03 μm thick Zn-doped Ga_{0.5}In_{0.5}P, and 0.3 μm thick Zn-doped GaAs. For the fabrication of solar cells, *n*-type Ni/Au/Ge/Ni/Au (20/100/30/30/200 nm) ohmic contact was deposited on the *n*⁺ GaAs layer, followed by the mesa etching in the H₃PO₄ and HCl-based solutions for GaAs and InGaP etching, respectively. The *p*-type Pt/Ti/Pt/Au (20/30/20/200 nm) ohmic contact on the bottom *p*⁺GaAs layer. Rapid thermal annealing was then carried out at 400°C for 40 s to reduce contact resistance and *n*⁺GaAs contact layer on the window was etched for efficient light absorption. The antireflective surfaces based on ZnO nanowires and nanosheets are produced on the top surface of the solar cells.

Characterization

The scanning electron microscopy (SEM) was done using a cold field emission scanning electron microscope (FE-SEM, S-4800, Hitachi) with an accelerating voltage of 10 kV. The high-resolution TEM images were collected using a Cs-corrected JEM-2100 operated at 200 kV. Reflectance data were obtained at wavelengths ranging between 300 and 1000 nm using a UV-Vis spectrometer (Perkin-Elmer Lambda 750) equipped with integrating sphere. The reflected light was collected into the angular acceptance range characterized by the minimum and maximum acceptance angles. In order to verify

the effect of MgF_2 on reflectance of the ZnO nanosheets, FDTD solutions software with a RF module was employed for two-dimensional finite element frequency domain simulation. The J - V curves of the devices were measured under AM 1.5G illumination at intensity of 100 mW cm^{-2} with McScience XES-301S. The external quantum efficiency (EQE) spectra were obtained from an incident photon-to-current conversion efficiency (IPCE) with K3100 Spectral IPCE Measurement System consisting of a 400W Xe lamp as a light source.

4.4.3 Result and discussion

ZnO based on antireflective layers

Figure 42a shows a schematic image of GaAs solar cells with three representative nanostructured antireflective surfaces; MgF_2/ZnO nanowires/ ZnO/TiO_2 , MgF_2/ZnO nanowires/ ZnO/ZnS , and MgF_2/ZnO nanosheets/ Al/ZnS . The corresponding cross-sectional scanning electron microscope (SEM) images are shown in Figure 42b, 42c, and 42d. The ZnO nanowires are approximately $3.0 \mu\text{m}$ in length and 65 nm in diameter, respectively. The ZnO nanosheets are seen in 25 nm in thickness, about 3 times smaller than the nanowires, as shown in Figure 43. The thickness of the nanosheet increases as the thickness of the Al layer increases. On the Al layer of less than 0.5 nm , nanowires were also observed, meaning that the Al layer was not formed uniformly. For elemental analysis, the nanosheets were transferred onto a foreign substrate and Energy-dispersive X-ray spectroscopy (EDXS) was performed. This analysis showed that the nanosheet was composed of zinc, oxygen, and aluminium (Figure 44c), while Zn and O were the only components in the nanowire. The Al was also observed in X-ray photoelectron spectroscopy (XPS), as shown in Figure 45. The peak in the Al $2p$ spectra corresponds to Al-O and Al-Zn-O bonds. The Al-O binding energy was observed at 73.63 eV , lower than that ($\sim 75.6 \text{ eV}$) of the pure Al_2O_3 . By RF magnetron sputtering, MgF_2 film was deposited on the ZnO nanowires and nanosheets. After MgF_2 film deposition, the diameter increased to approximately 100 nm and 60 nm , respectively, meaning that the thickness of MgF_2 film is about 17 nm in Figure 46.

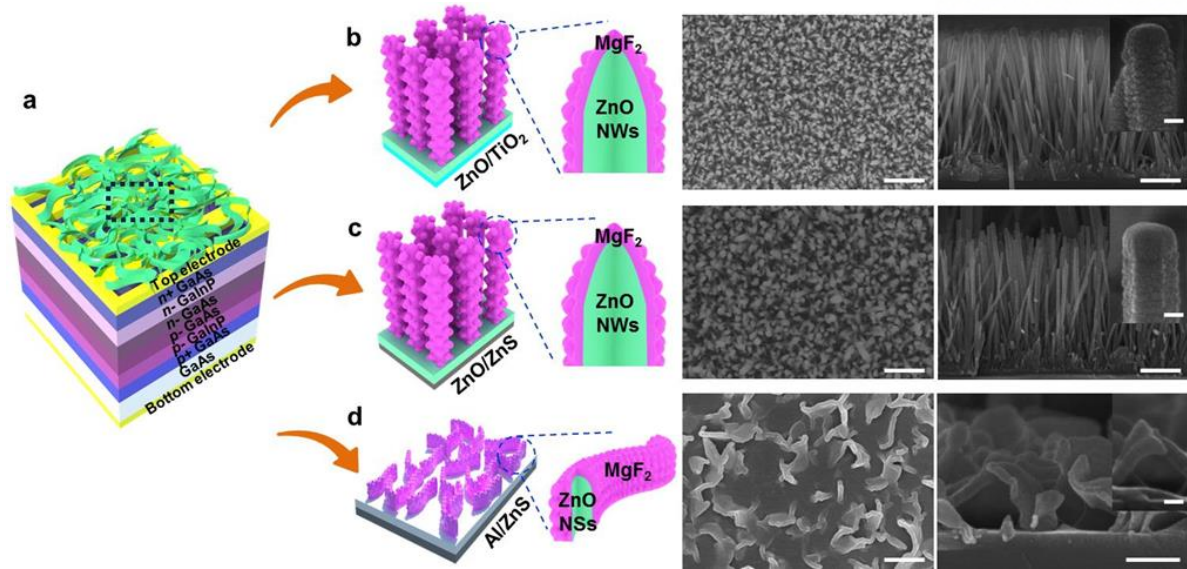


Figure 42. (a) Schematic images of a GaAs based solar cell with MgF_2/ZnO nanosheet/Al/ZnS as the AR coatings. Schematic and SEM images of (b) MgF_2/ZnO nanowires/ ZnO/TiO_2 , (c) MgF_2/ZnO nanowires/ ZnO/ZnS , and (d) MgF_2/ZnO nanosheet/Al/ZnS. The scale bars in the SEM images are $1\ \mu\text{m}$ except of the right image of (d), which is $250\ \text{nm}$. The insets also show the enlarged images (scale bar $50\ \text{nm}$).

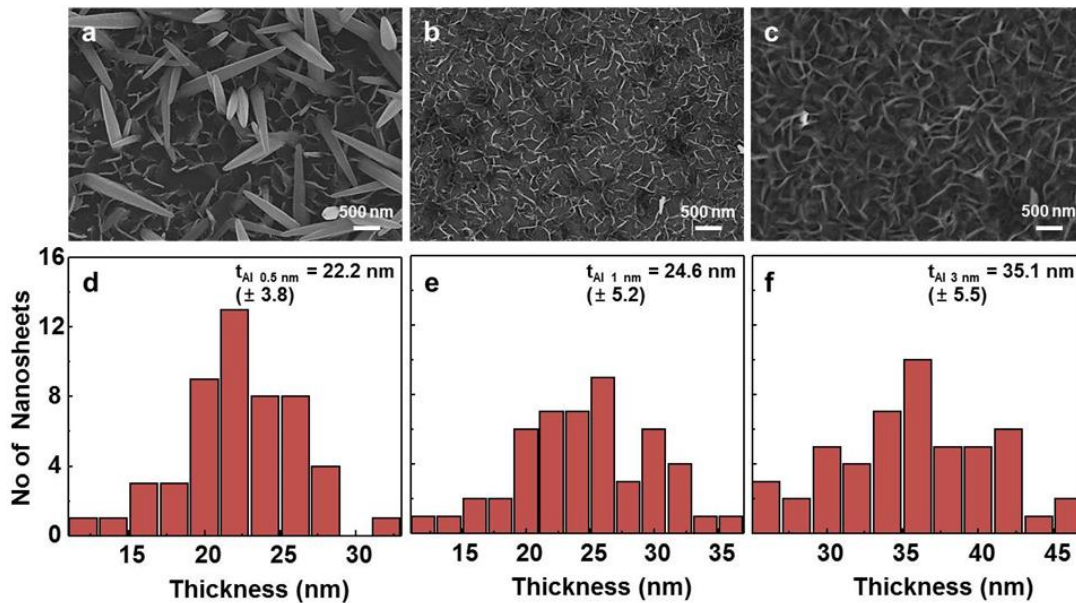


Figure 43. Top view of SEM image for ZnO nanosheet/Al/ZnS with thickness of Al (a) $0.5\ \text{nm}$, (b) $1\ \text{nm}$, (c) $3\ \text{nm}$ and (d-f) histogram of the ZnO nanosheets thickness distributions along Al thickness, respectively.

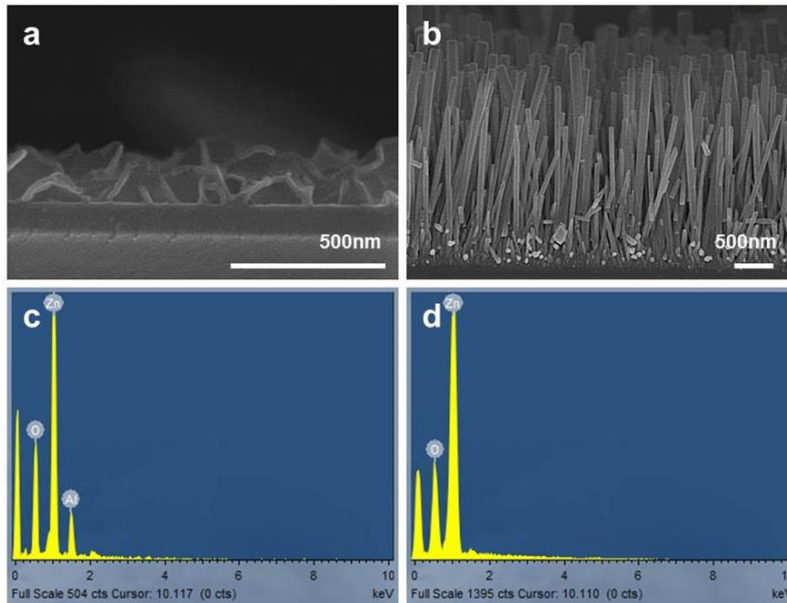


Figure 44. Scanning electron micrographs of ZnO nanosheet grown on Si substrates; (a) Top view and (b) cross-sectional SEM image, Energy-dispersive X-ray spectroscopy (EDXS) of (c) ZnO nanosheet/Al/ZnS, (d) ZnO nanowires/ZnO/ZnS.

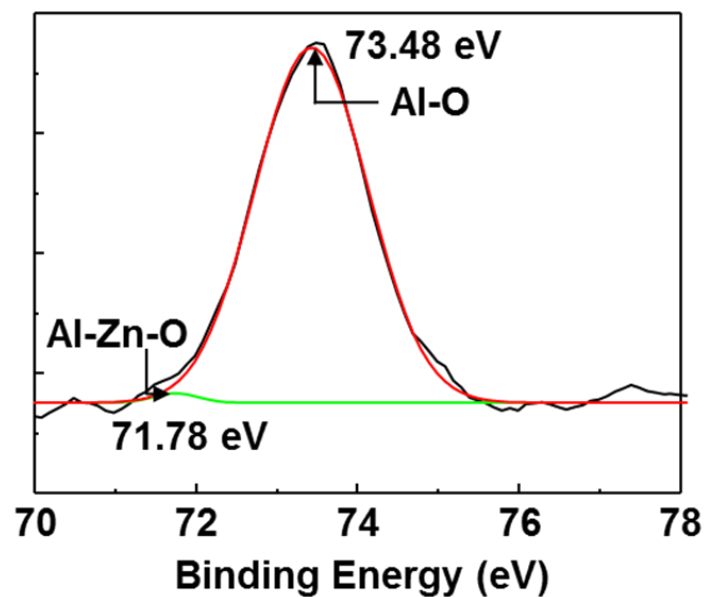


Figure 45. The peak in the Al 2p spectra corresponds to Al-O and Al-Zn-O bonds. The Al-O binding energy was observed at 73.48 eV, lower than that (~ 75.6 eV) of the pure Al_2O_3 .

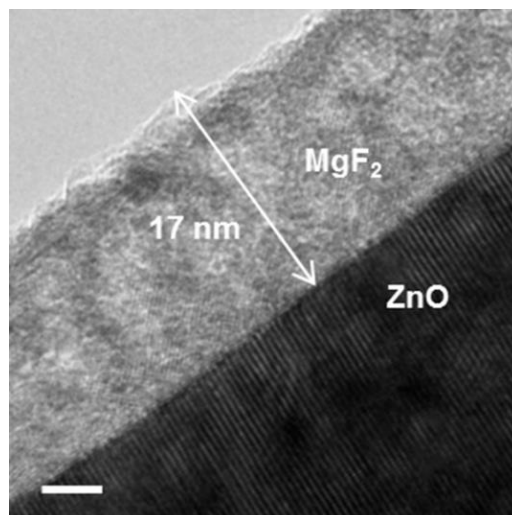


Figure 46. Transmission electron microscopy (TEM) images of MgF₂ thickness on MgF₂/ZnO nanowires (scale bar is 5 nm).

The crystal structures at the interface of MgF₂ and ZnO layers were characterized by low- and high-resolution transmission electron microscopy (HR-TEM) images. Figure 47 and 47b show TEM images of MgF₂-coated ZnO nanowires with the Fast Fourier Transform (FFT). Thin MgF₂ shells are clearly visible and they appear to be quite uniform along the body of the nanowire. The corresponding atomic spots and the diffraction patterns reveal that the layers are highly crystalline. FFT patterns taken along the $[2\bar{1}\bar{1}0]$ zone axis, together with measured lattice spacing of the adjacent planes, confirm that the nanowire grew along the *c*-axis. For the nanosheets, it is also clearly seen that the ZnO was preferentially grown in the same direction. According to the mechanism suggested previously^{21,22}, prior to the growth, the Al is oxidized to Al₂O₃, forming the AlO₂⁻ ions in the solution. The AlO₂⁻ ions at the surface react with the Zn²⁺ ions, producing ZnAl₂O₄ at the nanolevel, promoting the growth along the direction by decreasing the growth rate of different facets in ZnO.

In Figure 44, a small amount of Al is present in nanosheets, meaning that the Al from the ultrathin Al layer was diffused and incorporated into the ZnO during the growth. The Al doping by the diffusion was already reported and have been commonly observed when the layers were annealed at high temperature (> 800°C)²³. It is unlikely that the Al easily diffuse into ZnO because the growth temperature is not so high (~ 90°C). However, it can be expected that the Al atoms can move via a defect-mediated mechanism (the vacancy-mediated diffusion) into and inside the ZnO. Actually, the TEM results shows that the Al doping increases the spacing between two adjacent planes along the *c*-axis by approximately 10 %, as shown in Figure 47b and 47d. Furthermore, the defects commonly observed at the interface between ZnO and seed layer will promote the nucleation of the ZnAl₂O₄ at the surface for nanosheet growth. The incorporation of the Al atoms into the ZnO nanosheet was also reported in a hydrothermal process when Al substrate was used²⁴.

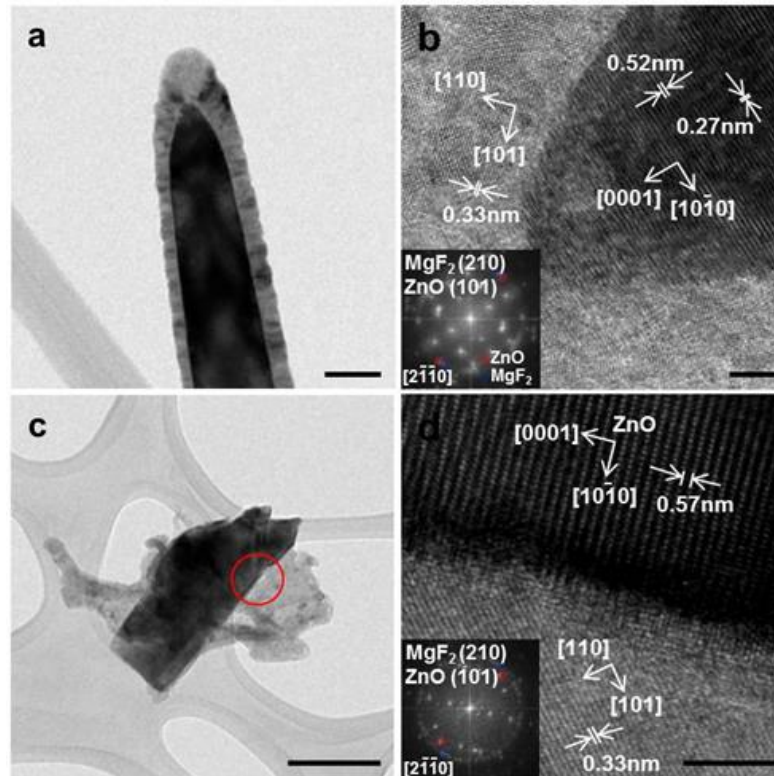


Figure 47. Transmission electron microscopy (TEM) images of MgF₂/ZnO nanowires and MgF₂/ZnO nanosheet. (a) Low-magnification MgF₂/ZnO nanowires (scale bar is 50 nm) and (b) High-resolution TEM (HR-TEM) image of MgF₂/ZnO nanowires (scale bar is 5 nm). (c) Low-magnification MgF₂/ZnO nanosheet (scale bar is 0.2 μm) and (d) HR-TEM image of MgF₂/ZnO nanosheet (scale bar is 5 nm). The inset shows a Fast Fourier Transform (FFT) of the image.

Optical properties of ZnO nanostructure

To investigate the AR characteristics of the nanostructured surfaces based on nanowires and nanosheets over the broad range of wavelength, we observed the total reflection over a wavelength range from 300 to 800 nm, as shown in Figure 48a. The incident angle with respect to the parallel of the sample was 83 ° in this measurement. After the MgF₂ was deposited on ZnO nanowires grown on TiO₂ layer, the reflectance was found to be less than 2 % in the UV and visible range. This ascribes to the decrease in effective refractive index from the bottom to the top of the nanowires and the low refractive index (~ 1.38) of the MgF₂, well-known previously²⁵. The TiO₂ layer was also reported to be effective in decreasing the reflectance, thereby, enhancing the solar cell performance. As the TiO₂ is replaced by the ZnS, the reflectance increases, but it is still found to be less than 3 % in the range.

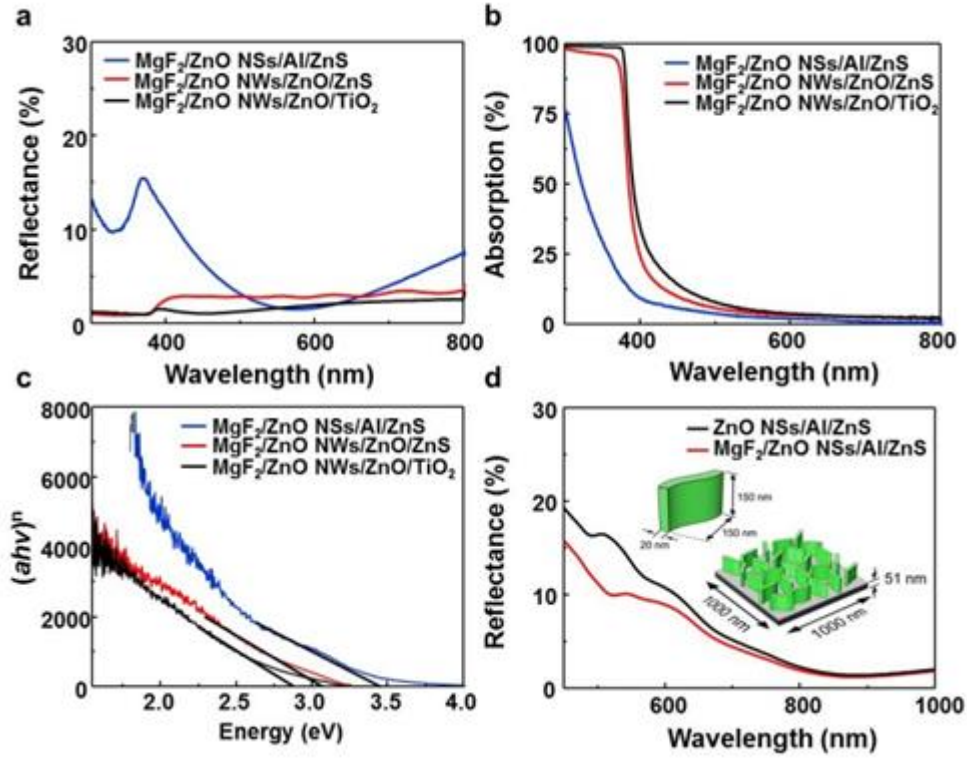


Figure 48. (a) UV-Vis-NIR reflectance spectra over a wavelength range from 300 to 800 nm: MgF₂/ZnO nanowires/ZnO/TiO₂, MgF₂/ZnO nanowires/ZnO/ZnS and MgF₂/ZnO nanosheet/Al/ZnS. (b) UV-Vis-NIR absorption spectra in the range from 300 to 800 nm. The absorption calculated by measuring the reflection (at a 7 ° angle of incidence) using $A \% = 100 \% - R \% - T \%$ while it is assumed that the scattering effect is negligible. (c) Corresponding plot of transformed Kubelka-Munk function versus the energy of the light. (d) Simulated spectra of the effect of the straight MgF₂ shell on the reflectance. Wavelength-dependent simulated reflectance distribution at 90 °.

The reflection in multi-layered AR coatings may be quite complicated due to the multiple reflections and interference effects occurring at the interface of the layers. Furthermore, for the nanowire-type AR coatings, it is difficult to explain the reflection because of the complicated nanowire morphologies. If the optical transmission of the ZnO/TiO₂ layered structure is taken into account multiple reflections and compared with the ZnO/ZnS layered structure, the reflection can be calculated by Eq. (1)²⁶⁻²⁸,

$$R = \frac{r_1^2 + r_2^2 + r_3^2 + r_1^2 r_2^2 r_3^2 + 2r_1 r_2 (1 + r_3^2) \cos 2\theta_1 + 2r_2 r_3 (1 + r_1^2) \cos 2\theta_2 + 2r_1 r_3 \cos 2(\theta_1 + \theta_2) + 2r_1 r_2^2 r_3 \cos 2(\theta_1 - \theta_2)}{1 + r_1^2 r_2^2 + r_1^2 r_3^2 + r_2^2 r_3^2 + 2r_1 r_2 (1 + r_3^2) \cos 2\theta_1 + 2r_2 r_3 (1 + r_1^2) \cos 2\theta_2 + 2r_1 r_3 \cos 2(\theta_1 + \theta_2) + 2r_1 r_2^2 r_3 \cos 2(\theta_1 - \theta_2)}$$

(1)

where, r_1 , r_2 , and r_3 are the amplitude reflection coefficients. θ is the incident angle of light and t is the thickness.

$$r_1 = \frac{n_0 - n_1}{n_0 + n_1} \quad (2)$$

$$r_2 = \frac{n_1 - n_2}{n_1 + n_2} \quad (3)$$

$$r_3 = \frac{n_2 - n_3}{n_2 + n_3} \quad (4)$$

$$\theta_1 = \frac{2\pi n_1 t_1}{\lambda} \quad (5)$$

$$\theta_2 = \frac{2\pi n_2 t_2}{\lambda} \quad (6)$$

n_0 , n_1 , n_2 and n_3 are the refractive indices of the air, ZnO, TiO₂ (or ZnS) and substrate. It is clearly observed that the nanostructures with a 50 nm thick TiO₂ layer show lower reflectance than those with ZnS layer in the entire region except near UV region, as shown in Figure 49. As the thickness of the layer increases, the reflectance decreases, indicating that the reflection can be lowered by optimizing the thickness of each layer.

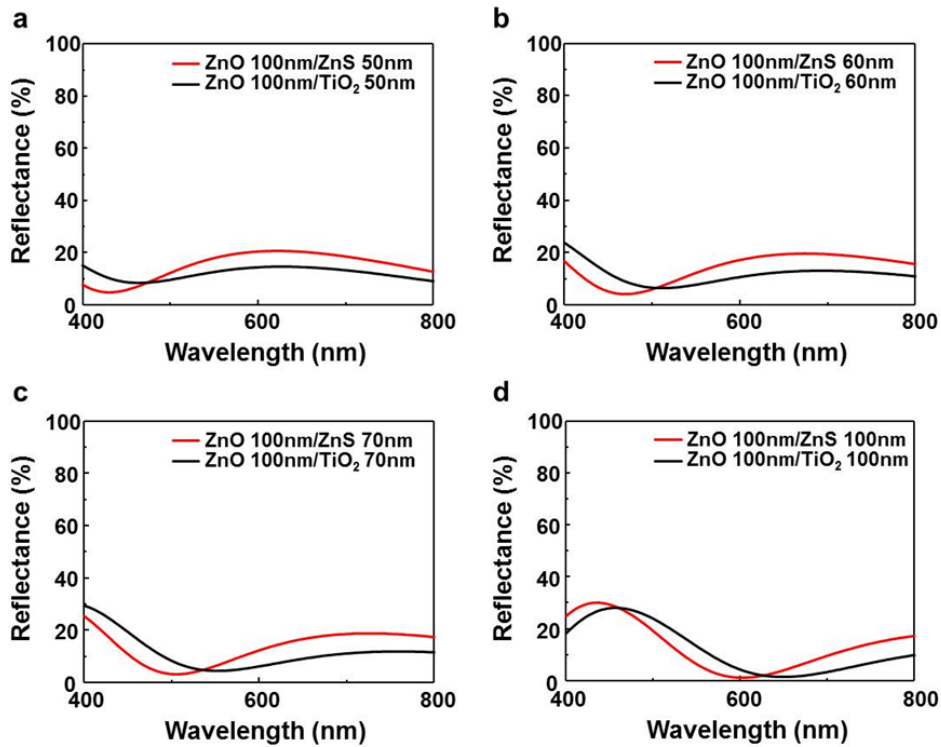


Figure 49. Simulated reflectance spectra for the ZnO/TiO₂ and ZnO/ZnS double layered films with different thickness. The thickness is ZnO 100nm, TiO₂ (or ZnS) (a) 50 nm, (b) 60 nm, (c) 70 nm and (d) 100 nm.

Note that the reflectance of both MgF₂/ZnO nanowires antireflection coatings is almost same in the near UV region (at the wavelength less than 400 nm), less than 1 ~ 2 %. This may ascribe to the low

bandgap (3.37 eV) of ZnO²⁹. This implies that the ZnO nanowires or film absorb the photons in UV light having wavelength less than 370 nm, preventing light to enter the active region of the solar cell. TiO₂ also has a small bandgap of 2.85 eV, indicating that the layer absorbs the light at the wavelengths shorter than 430 nm and lower the reflectance, compared with MgF₂/ZnO/ZnS sample³⁰. However, for the MgF₂ deposited ZnO nanosheets on Al/ZnS, it shows high reflectance (10 ~ 15 %) in near UV region, meaning that some of light can pass to the active region of the solar cell. It is also clearly seen that the reflectance is around 5 % or less over a wavelength range from 500 to 800 nm.

Figure 48b shows the total absorption of the nanostructured surfaces over a wavelength range from 300 to 800 nm using UV-vis-IR absorbance spectroscopy. For the MgF₂/ZnO nanowires on TiO₂ layer, it shows a high absorption close to 100 % in the UV region less than 400 nm. As the TiO₂ is replaced by the ZnS, the absorption is decreased to 92 % at 400 nm. For the ZnO nanosheets, it significantly decreases to 10 % at 400 nm. The absorbance was transformed by the following equation for the near-edge absorption as known as Kubelka-Munk method,

$$(\alpha hv)^n = K(hv - E_g) \quad (7)$$

where, K is a constant relative to the material, α is the absorption coefficient, hv is the photon energy, and n is 2 for a direct band gap semiconductor. The calculation shows that the MgF₂/ZnO nanowires on TiO₂ layer start to absorb below about 2.8 eV, which is equal to the optical bandgap of the TiO₂. The absorption edge increases to 3.2 eV as the TiO₂ is replaced by the ZnS, which is equal to the bandgap of the ZnO. For the ZnO nanosheets, it is found that the absorption band edge significantly increases to 3.4 eV. This means that the bandgap of the ZnO increases in the form of the nanosheets.

The blue-shift of the absorption edge in the nanosheets may be explained by the quantum confinement effect and the incorporation of Al atoms in ZnO. It was reported that various materials synthesized as a form of nanosheet showed an obvious blue shift in ultraviolet–visible (UV–vis) adsorption spectra due to the quantum confinement effect at an extremely small scale. Using a simple square quantum well potential of infinite height³¹, the band-to-band edge direct transition energy is proportional to $1/L^2$. Here, L is the thickness of the nanosheet. As L decreases, the transition energy increases. However, the critical size for significant quantum confinement effect should be less than 10 nm, which may be much smaller than that of the ZnO nanosheets. The incorporation of Al atoms in ZnO may be the reason for the blue-shift in the spectra. For the structures that are doped, the Al atoms are more favorable in the Zn sites than in the O sites, leading the ZnO nanosheet to an n type semiconductor³². According to the Burstein–Moss effect, the electrons occupy states within the conduction band, which pushes the Fermi level higher in energy, hence, the valence electrons require more energy to be excited to higher energy states in the conduction band. Therefore, the optical band gap of the nanosheets becomes larger than that of nanowires, thereby, increasing the optical transmittance, consistent with the results in Figure 48c.

To further verify the effect of the MgF₂ layer on the reflectance, we performed simulations for

reflectance of nanosheet structure with and without MgF_2 coating layer using the finite-difference time-domain (FDTD) method. To mimic the nanosheet structures shown in SEM images, we modelled 150 nm-height ZnO waveform nanostructure on the multilayer of Al (1nm)/ZnS (50nm)/Si (semi-infinite). The average thickness of the nanosheets and the MgF_2 layer is assumed to be 20 nm and 20 nm, respectively. It was also assumed that the MgF_2 layer was coated uniformly on the ZnO nanosheets. For a large area of ZnO nanosheets, we used periodic boundary condition for x and y directions, where the randomly oriented 5 x 5 array of ZnO nanosheet (see the inset of Figure 48d) was adopted as the unit cell. The refractive index in the range of 450 and 1000 nm for each material was obtained from experiment measurement data³³⁻³⁶. The reflectance spectrum in Figure 48d reveals that the reflectance in the entire region of wavelength decreases by the coating the MgF_2 layer. Moreover, the high reflectance ($> 10\%$) was found at short wavelengths, consistent with the experimental results in Figure 48a.

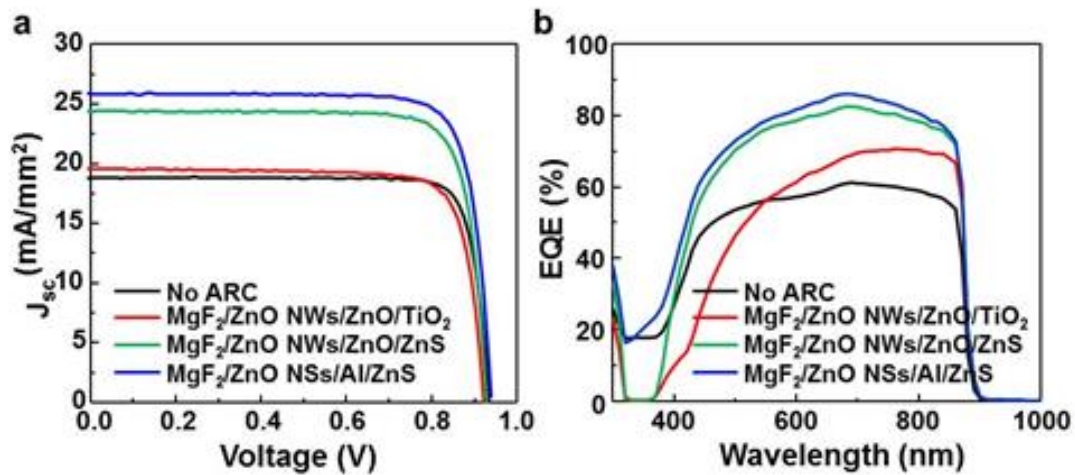


Figure 50. (a) The current density-voltage (J - V) curves of GaAs based solar cells with MgF_2/ZnO nanowires/ ZnO/TiO_2 , MgF_2/ZnO nanowires/ ZnO/ZnS , MgF_2/ZnO nanosheet/ Al/ZnS and without ARC layer under AM 1.5 G illumination ($100 \text{ mW}/\text{cm}^2$). (b) The external quantum efficiency (EQE) spectra of GaAs based solar cells with none, the MgF_2/ZnO nanowires/ ZnO/TiO_2 , MgF_2/ZnO nanowires/ ZnO/ZnS , MgF_2/ZnO nanosheet/ Al/ZnS ARC layers.

Efficiency of GaAs solar cell

The nanostructured AR surfaces based on nanowires and nanosheets were produced on the GaAs solar cells and the current-density versus voltage (J - V) curves are measured under AM1.5G illumination ($100\text{mW}/\text{cm}^2$, 1-sun) at room temperature. Figure 50a shows the J - V characteristics of solar cells integrated without and with the AR surfaces. For the solar cells without the AR surfaces, it shows an efficiency of approximately 14%. After the MgF_2/ZnO nanowires on TiO_2 layer are produced, there is

no significant change in the efficiency. As the TiO_2 is replaced by the ZnS , the efficiency is increased to 18.5 % without the change in the V_{oc} . These results show that many photons of the light is already absorbed in TiO_2 layer before entering the active region of the solar cell. After the ZnO nanosheets are grown, further increase to 19.8 % (43.9 % enhancement) in power conversion efficiency was observed despite the reflectance of this AR coating is 2 ~ 3 times larger than those of the nanowires-based AR coatings. This implies that the increase in the bandgap with the growth of the ZnO nanosheets with small thickness less than 20 nm significantly contributes to the enhancement of the solar cell performance. The spectral responses of external quantum efficiency (EQE) and surface reflectance were also measured to further analyse the antireflection capability of the AR surfaces in GaAs solar cells, plotted in Figure 50b. When the ZnO nanosheets were used, the GaAs solar cell exhibited a broad-range EQE enhancement from 400 to 900 nm and there was a 30 % enhancement in the EQE. Also note that the EQE is nearly zero in the solar cell with nanowire-based AR coatings at the wavelengths less than 400 nm, meaning that the light absorption is mainly due to the ZnO and TiO_2 , in which the AR coatings do not contribute to the solar cell performance. Integrating the EQE over a standard AM 1.5G illumination spectrum yields a short-circuit current density (J_{sc}) for the solar cell with ZnO nanosheets of 24.54 mA cm^{-2} , quite similar to the value in Figure 50a and Table 3.

Table 3. Short-circuit current density (J_{sc}), open-circuit voltage (V_{oc}), fill factor (FF) and power conversion efficiency of solar cells before and after integrated with the MgF_2/ZnO nanowires/ ZnO/TiO_2 , MgF_2/ZnO nanowires/ ZnO/ZnS and MgF_2/ZnO nanosheet/ Al/ZnS layer under AM1.5G normal illumination at room temperature

Samples	$J_{sc}/(\text{mA cm}^{-2})$	V_{oc}/V	FF%	$\eta\%$
No ARC (ZnO/TiO_2)	18.92	0.82	84.46	14.92
ZnO/ TiO_2 nanowires	19.63	0.80	80.78	14.60
No ARC (ZnO/ZnS)	19.66	0.80	80.09	14.54
ZnO/ ZnS nanowires	24.43	0.81	81.59	18.54
No ARC (Al/ZnS)	19.1	0.93	77.98	13.77
Al/ZnS nanosheets	25.9	0.94	81.39	19.81

4.4.4 Conclusion

In summary, a series of hierarchical ZnO nanostructures-based AR coatings was prepared by a hydrothermal method of ZnO nanostructures, followed by means of RF sputtering for coaxial

nanostructures. The two types of nanostructures (nanowires and nanosheets) was synthesized hydrothermally on high-refractive index layer by properly selecting the kind of seed layer; ZnO thin film for nanowires and Al thin film for nanosheets. The structural analysis showed that the ZnO has highly preferred orientation along $\langle 0001 \rangle$ direction with highly crystalline MgF_2 shell uniformly coated. It was observed that the thickness of the nanosheets increased with the thickness of the Al layer. A small amount of Al was present in nanosheets, originated from the Al diffusion from the Al seed layer, resulting in an increase of the optical bandgap. For nanosheets-based AR coatings, it showed quite high reflectance (10 ~ 15 % in near UV region and 5 % in visible region), while nanowires-based AR coatings showed low reflectance of 2~3 % in the entire region. Furthermore, nanowires-based AR coatings showed perfect absorption in near UV region. However, contrary to the AR characteristics, the GaAs solar cell showed the largest enhancement (43.9 %) from 13.77 % to 19.81 % in power conversion efficiency when the nanosheet-based AR coatings were used. These results shows that the low reflection of the nanowires-based AR coatings is mainly due to the high light absorption of the ZnO and TiO_2 , which prevent light to pass to the active region of the solar cell. The increase of the optical bandgap of the nanosheets due to the incorporation of Al atoms improves the optical transmittance, enhancing the solar cell performance.

4.4.5 Reference

- [1] Wu, T.-H.; Chuang, R.W.; Huang, C.-Y.; Cheng, C.-Y.; Huang, C.-Y.; Lin, Y.-C.; Su, Y.-K. ZnO nanoneedles/ZnO: Al film stack as an anti-reflection layer for high efficiency triple junction solar cell. *Solid-State Lett.*, **2012**, 15, H208-H210.
- [2] Tsan, M.-T.; Yang, Z.-P.; Jing, T.-S.; Hsieh, H.-H.; Yao, Y.-C.; Lin, T.-Y.; Chen, Y.-F.; Lee, Y.-J. Achieving graded refractive index by use of ZnO nanorods/TiO₂ layer to enhance omnidirectional photovoltaic performances of InGaP/GaAs/Ge triple-junction solar cells. *Sol. Energy Mater. Sol. Cells.*, **2015**, 136, 17–24.
- [3] Hou, J.-L.; Chang, S.-J.; Hsueh, T.-J.; Wu, C.-H.; Weng, W.-Y.; Shieh, J.-M. InGaP/GaAs/Ge triple-junction solar cells with ZnO nanowires. *Prog. Photovolt: Res. Appl.*, **2013**, 21, 1645–1652.
- [4] Wu, J.J.; Liu, S.C. Low-temperature growth of well-aligned ZnO nanorods by chemical vapor deposition. *Adv. Mater.*, **2002** 14, 215–218.
- [5] Ge, X.; Hong, K.; Zhang, J.; Liu, L.; Xu, M. A controllable microwave-assisted hydrothermal method to synthesize ZnO nanowire arrays as recyclable photocatalyst. *Mater. Lett.*, **2015**, 139, 119–121.
- [6] Hu, X.; Heng, B.; Chen, X.; Wang, B.; Sun, D.; Sun, Y.; Zhou, W.; Tang, Y. Ultralong porous ZnO nanobelt arrays grown directly on fluorine-doped SnO₂ substrate for dye-sensitized solar cells. *J. Power Sources.*, **2012**, 217, 120-127.
- [7] Wan, L.; Wang, X.; Yan, S.; Yu, H.; Li, Z.; Zou, Z. ZnO plates synthesized from the ammonium zinc nitrate hydroxide precursor. *CrystEngComm.*, **2012**, 14, 154-159.
- [8] Chen, S.-W.; Wu, J.-M. Nucleation mechanisms and their influences on characteristics of ZnO nanorod arrays prepared by a hydrothermal method. *Acta Mater.*, **2011**, 59, 841-847.
- [9] Yeh, L.-K.; Lai, K.-Y.; Lin, G.-J.; Fu, P.-H.; Chang, H.-C.; Lin, C.-A.; He, J.-H. Giant efficiency enhancement of GaAs solar cells with graded antireflection layers based on syringelike ZnO nanorod arrays. *Adv. Energy Mater.*, **2011**, 1, 506-510.
- [10] Gayen, R.N.; Dalui, S.; Rajaram, A.; Pal, A.K. Modulation of field emission properties of vertically aligned ZnO nanorods with aspect ratio and number density. *Appl. Surf. Sci.*, **2009**, **255**, 4902-4906.
- [11] Ahmad, R.; Tripathy, N.; Kim, J.H; Hahn, Y.-B. Highly selective wide linear-range detecting glucose biosensors based on aspect-ratio controlled ZnO nanorods directly grown on electrodes. *Sens. Actuators B.*, **2012**, 174, 195-201.
- [12] Chu, F.-H.; Huang, C.-W.; Hsin, C.-L.; Wang, C.-W.; Yu, S.-Y.; Yeh, P.-H.; Wu, W.-W. Well-aligned ZnO nanowires with excellent field emission and photocatalytic properties. *Nanoscale.*, **2012**, 4, 1471-1475.

- [13] Qi, L.; Yu, H.; Lei, Z.; Wang, Q.; Ouyang, Q.; Li, C.; Chen, Y. Dye-sensitized solar cells based on ZnO nanowire array/TiO₂ nanoparticle composite photoelectrodes with controllable nanowire aspect ratio. *Appl Phys A*, **2013**, 111, 279–284.
- [14] Lee, J.W.; Ye, B.U.; Kim, D.; Kim, J.K.; Heo, J.; Jeong, H.Y.; Kim, M.H.; Choi, W.J.; Baik, J.M. ZnO nanowire-based antireflective coatings with double-nanotextured surfaces. *ACS Appl. Mater. Interfaces*. **2014**, 6, 1375–1379.
- [15] Hiralal, P.; Chien, C.; Lal, N.N.; Abeygunasekara, W.; Kumar, A.; Butt, H.; Zhou, H.; Unalan, H.E.; Baumberg, J.J.; Amaratunga, G.J. Nanowire-based multifunctional antireflection coatings for solar cells. *Nanoscale*., **2014**, 6, 14555-14562.
- [16] Baeka, S.-H.; Kima, S.-B.; Shinb, J.-K.; Kim, J.H. Preparation of hybrid silicon wire and planar solar cells having ZnO antireflection coating by all-solution processes. *Sol. Energy Mater. Sol. Cells*., **2012**, 96, 251–256
- [17] Park, H.S.; Chang, S.H.; Jean, J.; Cheng, J.J.; Araujo, P.T.; Wang, M.S.; Bawendi, M.G.; Dresselhaus, M.S.; Bulovic, V.; Kong, J.; Gradecak, S. Graphene cathode-based ZnO nanowire hybrid solar cells. *Nano Lett.*, **2013**, 13, 233–239
- [18] Aurang, P.; Demircioglu, O.; Es, F.; Turan, R.; Unalan, H.E. ZnO Nanorods as Antireflective Coatings for Industrial-Scale Single-Crystalline Silicon Solar Cells. *J. Am. Ceram. Soc.*, **2013**, 96, 1253–1257.
- [19] Chang, S.-J.; Member, S.; Hou, J.-L.; Hsueh, T.-J.; Lam, K.-T.; Li, S.; Liu, C.-H.; Chang, S.-P. Triple-junction GaInP/GaAs/Ge solar cells with an AZO transparent electrode and ZnO nanowires. *Photovoltaics, IEEE Journal of*., **2013**, 3, 3.
- [20] Chen, J.Y.; Sun, K.W. Growth of vertically aligned ZnO nanorod arrays as antireflection layer on silicon solar cells. *Sol. Energy Mater. Sol. Cell.*, **2010**, 94, 930–934.
- [21] Huang, H.; Wang, H.; Li, B.; Mo, X.; Long, H.; Li, Y.; Zhang, H.; Carroll, D.L; Fang, G. Seedless synthesis of layered ZnO nanowall networks on Al substrate for white light electroluminescence. *Nanotechnology*, **2013**, 24, 315203.
- [22] Rahm, A.; Yang, G.W.; Lorenz, M.; Nobis, T.; Lenzner, J.; Wagner, G.; Grundmann, M. Two-dimensional ZnO: Al nanosheets and nanowalls obtained by Al₂O₃-assisted carbothermal evaporation. *Thin Solid Films*. **2005**, 486, 191–194.
- [23] Johansen, K.M.; Vines, L.; Bjørheim, T.S.; Schifano, R.; Svensson, B.G. Aluminum migration and intrinsic defect interaction in single-crystal zinc oxide. *Phys. Rev. Applied.*, **2015**, 3, 024003.
- [24] Gaddam, V.; Kumar, R.R.; Parmar, M.; Yaddanapudi, G.R.K.; Nayak, M.M.; Rajanna, K. Morphology controlled synthesis of Al doped ZnO nanosheets on Al alloy substrate by low-temperature solution growth method. *RSC Adv.*, **2015**, 5, 13519.

- [25] Lee, I.; Lee, W.J.; Y, J. Optimization of MgF₂/CeO₂/Si for antireflection coatings on crystalline silicon solar cell. *J. Korean Phys. Soc.*, **2001**, 39, 57-61.
- [26] Wang, E.Y.; Yu, F.T.S.; Sims, V.L.; Brandhorst, E.W.; Broder, J.D. *10th IEEE Photovoltaic Specialists Conference.*, **1973**, 168-171.
- [27] Kosyachenko, L.A.; Mathew, X.; Paulson, P.D.; Lytvynenko, V.Ya.; Maslyanchuk, O.L. Optical and recombination losses in thin-film Cu(In, Ga)Se₂ solar cells. *Sol. Energy Mater. Sol. Cell.*, **2014**, 130, 291–302.
- [28] Heavens, O.S. *Dover Publications Inc.*, **1991**.
- [29] Kong, Y.C.; Yu, D.P.; Zhang, B.; Fang, W.; Feng, S.Q. Ultraviolet-emitting ZnO nanowires synthesized by a physical vapor deposition approach. *Appl. Phys. Lett.*, **2001**, 78, 407.
- [30] Khan, M.M.; Ansari, S.A.; Pradhan, D.; Ansari, M.O.; Han, D.H.; Lee, J.; Cho, M.H. Band gap engineered TiO₂ nanoparticles for visible light induced photoelectrochemical and photocatalytic studies. *J. Mater. Chem. A.*, **2014**, 2, 637-644.
- [31] Mudd, G.W.; Svatek, S.A.; Ren, T.; Patanè, A.; Makarovskiy, O.; Eaves, L.; Beton, P.H.; Kovalyuk, Z.D.; Lashkarev, G.V.; Kudrynskiy, Z.R.; Dmitriev, A.I. Tuning the bandgap of exfoliated InSe nanosheets by quantum confinement. *Adv. Mater.*, **2013**, 25, 5714–5718.
- [32] Feng, X.-Y.; Wang, Z.; Zhang, C.-W.; Wang, P.-J. Electronic structure and energy band of IIIA doped group ZnO nanosheets. *J NANOMATER*, **2013**, 6, 181979.
- [33] Rakić, A.D.; Djurišić, A.B.; Elazar, J.M.; Majewski, M.L. Optical properties of metallic films for vertical-cavity optoelectronic devices. *Appl. Opt.*, **1998**, 37, 5271-5283.
- [34] Li, H.H. Refractive index of alkaline earth halides and its wavelength and temperature derivatives. *J. Phys. Chem. Ref. Data*, **1980**, 9, 161-289.
- [35] Debenham, M. Refractive indices of zinc sulfide in the 0.405–13- μ m wavelength range. *Appl. Opt.*, **1984**, 23, 2238-2239.
- [36] Bond, W.L. Measurement of the refractive indices of several crystals. *J. Appl. Phys.*, **1965**, 36, 1674-1677.

CURRICULUM VITAE

Hye Jin Lee

Street Address: UNIST-gil 50, Eonyang-eup, Ulju-gun, Ulsan, Republic of Korea, 44919.

E-mail: lhj0820@unist.ac.kr · Phone: +82-10-5133-2493

EDUCATION

2014-present **Ulsan National Institute of Science and Technology (UNIST)**

- Combined MS/Ph.D in Materials Science and Engineering.
- UNIST-KIST Research Scholarship.
- Supervisor: Professor, Jeong Min Baik

2014-present **Korea Institute of Science and Technology (KIST)**

- Center for Opto-Electronic Materials and Devices
- Supervisor: Dr. Won Jun Choi

2010-2013 **Kyungpook National University (KNU)**

- B.S. in Nano & Materials Science and Engineering.
- Supervisor: Professor, Sang Sik Park

RESEARCH EXPERIENCE

Functional Metal Oxides Nanostructures

- Hierarchical ZnO NWs/ZnS NSs Hybrids for Efficient Light Absorption in Solar Cell
- Stretchable Ti/MgF₂ Multilayer for Broad-band Solar Absorption
- Aligned VO₂ NWs Array based on Directional Ostwald Ripening

Solar-Thermal Conversion System & Wearable Physical Sensor

- Design of Anti-Reflection Layer for Enhancing Solar Cell Performance
- Solar Absorber for High-Power Thermoelectric Generator and Water

Heating System.

- Strain Sensor Based on Metal-Insulator Transition in Highly Aligned VO₂ NWs Array
- Thermally Stable Micro-Bolometer for Infrared Imaging Sensors

TEACHING EXPERIENCE

Teaching Assistant

- 2018, Fall **Teaching Assistant, Introduction to Semiconductor**, Department of Materials Science and Engineering, Ulsan National Institute of Science and Technology
- 2017, Fall **Teaching Assistant, Special Topics in Materials Science and Engineering (Nano energy)**, Department of Materials Science and Engineering, Ulsan National Institute of Science and Technology

AWARD

- 2018 • **Best Poster Award (Gold Award)**, International Conference on Electronic Materials and Nanotechnology for Green Environment (ENGE)
- 2015 • **Excellent Poster Award**, KIST-UNIST Ulsan Center (KUUC)

PUBLICATION

1. **Hye Jin Lee**, Jae Won Shin, Jun Gi Kim, Kyung Guen Song, Won Jun Choi*, Jeong Min Baik*, “Development of solar water heating system using photo-thermal conversion material” **Energy Environ. Sci.** In

preparation. (2019)

2. **Hye Jin Lee**, Tae-Hyeon Kil, Ho-Sung Kim, Seung Yeop Ahn, Seung-Hyub Baek, Won Jun Choi* and Jeong Min Baik*, “High temperature Operation (~100°C) of VO₂ Based Micro-bolometer with Infrared absorbing layer”. **Sens. Actuator A-Phys.** In preparation. (2019)
3. **Hye Jin Lee**, U-Jeong Yang, Kyeong Nam Kim, Soojin Park, Kye Hyoung Kil, Jun Soo Kim, Martin Moskovits, Galen D. Stucky, Alec M. Wodtke, Won Jun Choi*, Myung Hwa Kim*, Jeong Min Baik*, “Directional Ostwald ripening for producing aligned arrays of nanowires”, **Nano Lett.** *Online published.* (2019)
4. **Hye Jin Lee**, Dae-Han Jung, Tae-Hyeon Kil, Sang Hyeon Kim, Ki-Suk Lee, Seung-Hyub Baek, Won Jun Choi,* Jeong Min Baik*, “Mechanically Robust, Stretchable Solar Absorbers with Submicron-Thick Multilayer Sheets for Wearable and Energy Applications”, **ACS Appl. Mater. Interfaces.**, 9, 18061–18068 (2017)
5. **Hye Jin Lee**, Jae Won Lee, Hee Jun Kim, Dae-Han Jung, Ki-Suk Lee, Sang Hyeon Kim, Dae-myeong Geum, Chang Zoo Kim, Won Jun Choi*, Jeong Min Baik*, “Optical design of ZnO-based antireflective layers for enhanced GaAs solar cell performance”. **Phys. Chem. Chem. Phys.**, 18, 2906-2912 (2016)

PATENTS

1. Jeong Min Baik, Won Jun Choi, Seung Hyub Baek, **Hye Jin Lee**, “Micro-bolometer with Infrared Absorber Material having Multi-layer Structure and Method for Manufacturing The Same.” Korea, Patent No. 10-2018-0141634 (2018).

2. Jeong Min Baik, Won Jun Choi, **Hye Jin Lee**, “Nanowire Array Manufacturing Method and Flexible Strain Sensor Manufacturing Method Comprising The Same.” Korea, Patent No. 10-2018-0063762 (2018).
3. **[Patent Registration]** Won Jun Choi, **Hye Jin Lee**, Sang Hyeon Kim, Kyung Guen Song, “Solar Heat Boiler Using Absorber.” Korea, Patent No. 10- 2017-0070528 (2017), 101965619 (2019)
4. **[Patent Registration]** Jeong Min Baik, **Hye Jin Lee**, Won Jun Choi, Sang Hyeon Kim, “Infrared Absorber Element Including Thin Film Infrared Absorber Material.” Korea, Patent No. 10-2016-0056570 (2016), 101803290 (2017).
5. **[Patent Registration]** Jeong Min Baik, **Hye Jin Lee**, Won Jun Choi, Sang Hyeon Kim, “Method for Thin Film Infrared Absorber Material.” Korea, Patent No. 10-2015-0064370 (2015), 101684383 (2016).
6. **[Patent Registration]** Jeong Min Baik, Ki-Suk Lee, **Hye Jin Lee**, Won Jun Choi, Sang Hyeon Kim, “Method for Anti-reflection Coating of Solar cell.” Korea, Patent No. 10-2015-0064372 (2015), 101684947 (2016).

PRESENTATION

International Conference

1. International Conference on Electronic Materials and Nanotechnology for Green Environment (ENGE), Korea, November 11 – 14, 2018. Poster: Development of Solar Water Heating System Using Multi-layer

Photo-thermal Conversion Material.

2. European Materials Research Society (E-MRS), Poland, September 17-20, 2018. Poster: Development of Solar Water Heating System Using Multi-layer Photo-thermal Conversion Material.
3. International Symposium on the Physics of Semiconductors and Application (ISPSA 2018), Korea, July, 1-5, 2018. Poster: Self-guided Growth of sub-millimeter-long Vanadium Dioxide Nanowires Driven by Directional Ostwald Ripening.
4. International Symposium on the Physics of Semiconductors and Application (ISPSA 2018), Korea, July, 1-5, 2018. Poster: Development of Vanadium oxide-Based Micro-bolometer with Infrared absorbing layer.
5. Materials Research Society (MRS), USA, April 2-6, 2018. Poster: Development of Solar Water Heating System Using Multi-layer Photo-thermal Conversion Material.
6. Materials Research Society (MRS), USA, April 17 - 21, 2017. Oral: Self-guided Growth of Millimeter-long Vanadium Dioxide Nanowires.
7. International Conference on Electronic Materials and Nanotechnology for Green Environment (ENGE), Korea, November 6 – 9, 2016. Poster: Solar Absorption with Flexible Metal/Dielectric Multilayer Films for Thermoelectric and Wearable Application.
8. International Conference on Advanced Electromaterials (ICAE 2015), Korea, November 17-20, 2015. Poster: Nanosheet-based Coaxial Antireflective Layers for Enhanced GaAs Solar Cell Performance.

Domestic Conference

1. Photonics Conference (PC 2017), Korea, November 8~10, 2017, Poster: Infrared Absorber Based on Metal/Dielectric Multi-layers for Microbolometer.
2. Korea Society of LEDs and Optoelectronics (KSLOE 2015), Korea, January 26 – 27, 2015. Poster: Infrared Absorber Based on Metal/Dielectric Film Multilayers for Thermoelectric and Wearable Applications.
3. Korea Society of LEDs and Optoelectronics (KSLOE 2014), Korea, November 20 – 21, 2014. Poster: Self-powered Triboelectric Active Sensors for Sensitivity and Selectivity Volatile Organic Compound Vapours Detector.

SKILLS

- Technical:** Mask design and Photolithography, Hydrothermal growth (NWs, NSs), Solar-thermal conversion system, Physical sensing (Pressure, Strain) measurement, Gas sensing measurement, Bolometer measurement
- Laboratory** Material analysis (SEM, XRD, UV-Vis spectrometer, FTIR spectrometer), Processing equipment (E-beam evaporator, Sputter, PECVD, RIE, CVD, Furnace), Measurement equipment (Current source, blackbody source, cryostat, LCR meter, lock-in amplifier, preamplifier, spectral analysis, bending tester, pushing tester)
- Computer:** Origin Lab, Microsoft office, Auto CAD, Advanced Design System.